

# **Prediction of Textured Journal Bearing Performance Characteristics implementing Mass Conserving Boundary Conditions using Progressive Mesh Densification Method**

*A thesis*

*submitted in partial fulfillment of the  
requirements for the degree of*

**Doctor of Philosophy**

by

**Syed Nayab Rasool**



**Department of Mechanical Engineering  
Indian Institute of Technology Guwahati**

**January 2023**



# Certificate

It is certified that the work contained in the thesis entitled “**Prediction of Textured Journal Bearing Performance Characteristics implementing Mass Conserving Boundary Conditions using Progressive Mesh Densification Method**” is submitted by Syed Nayab Rasool to the Indian Institute of Technology Guwahati for the award of the degree of Doctor of Philosophy has been carried out under my supervision in the Department of Mechanical Engineering, Indian Institute of Technology Guwahati, India. This work has not been submitted elsewhere for the award of any other degree or diploma.

*S K Kakoty*  
(S K Kakoty)

Professor  
Department of Mechanical Engineering  
Indian Institute of Technology Guwahati

January 2023





***Dedicated  
To  
My Parents***



# Acknowledgment

---

I am extremely grateful to Almighty God, the most Gracious and Merciful, for granting me a blessed life. Indeed, without his help and will, nothing would be accomplished.


I wish to express my sincere gratitude to my supervisor, Prof. Sashindra Kumar Kakoty, for his constant advice, encouragement and support at every stage of my both personal and professional life. I have been associated with Prof. Sashindra Kumar Kakoty since my postgraduate studies and throughout this entire period of my doctoral studies. He provides excellent knowledge and experience in the field, which has been of great value to the results presented here. I learned a lot from him both on the professional and research front.

I also thank the members of my doctoral committee, Prof. S Senthilvelan, Prof. S Pal and Prof. S Talukdar, whose helpful suggestions increased the originality and quality of the thesis.

I am happy to acknowledge my debt to the present and past Heads of the Mechanical Engineering Department for providing me with the necessary arrangements to carry out my research.

Thanks to my colleagues, seniors and friends, Dr. Pranay Kumar Sarkar, Dr. Kamal Basumatary, Dr. Ashutosh Kumar, Dr. Sibananda Mohanty, Dr. Mirzaul Hussain, Mr. Durga Rao, Dr. Bibhuti Ranjan, Dr. Mahboob Alam, Dr. Shailendra, and Mr. Debajit Das for their help at various stages of my research work. I would also like to thank Mr. Kaustubh Khaire, Mr. Shaik Masruddin, Mr. Abdul Qadir and Mr. Dharendra Verma for giving me company on this journey.

Last but not least, I would like to show my gratitude to my parents, who made sacrifices to help me reach this stage. I also thank my family members for their support on the family front.



**Syed Nayab Rasool**

**IIT Guwahati**



# Contents

---

<b>1</b>	<b>Introduction</b>	<b>1</b>
1.0	State of the art	1
1.1	Literature review	2
1.1.1	Effect of surface texture on slider bearing	2
1.1.2	Effect of surface texture on thrust bearing	5
1.1.3	Effect of surface texture on journal bearing	7
1.1.4	Progressive mesh densification (PMD) method	14
1.1.5	Multigrid (MG) method	15
1.1.6	Fixed mesh density (FMD) method	16
1.2	Research gap	17
1.3	Scope of the present work	18
1.3.1	Objectives	18
1.4	Organization of the thesis	18
<b>2</b>	<b>Basic equations, boundary conditions and computational methods</b>	<b>21</b>
2.0	Introduction	21
2.1	Theory for textured journal bearing using Reynolds boundary conditions	21
2.1.1	Governing equation	21
2.1.2	Fluid film thickness	25
2.1.3	Reynolds Boundary conditions	25
2.1.4	Solution Scheme	26
2.1.5	Bearing performance parameters	27

2.2 Theory for textured journal bearing using mass conserving (JFO) boundary conditions	27
2.2.1 Governing equation	27
2.2.2 Fluid film thickness	30
2.2.3 Solution Scheme	31
2.2.4 Pressure in the full film region	31
2.2.5 Non-dimensional bearing parameters	32
2.2.6 Performance enhancement ratio	33
2.3 Multigrid (MG) method	33
2.4 Progressive mesh densification (PMD) method	35
2.4.1 Lagrange interpolation	37
2.5 Summary	38
<b>3 A Computational algorithm for textured journal bearing: progressive mesh densification (PMD) and multigrid (MG)</b>	<b>39</b>
3.0 Introduction	39
3.1 Comparison of computational efficiencies for different $L/D$ ratios	39
3.1.1 Comparison of computational efficiencies for $L/D = 0.2$	42
3.1.2 Comparison of computational efficiencies for $L/D = 1$	43
3.1.3 Comparison of computational efficiencies for $L/D = 2$	49
3.2 Summary	51
<b>4 Influence of texture parameters on computational efficiencies of PMD, MG and FMD methods</b>	<b>53</b>
4.0 Introduction	53
4.1 Influence of texture parameters	53

4.1.1 Influence of texture portion	55
4.1.2 Influence of dimple area density	58
4.1.3 Influence of dimple aspect ratio	60
4.1.4 Influence of non-dimensional clearance	67
4.1.5 Influence of non-dimensional length	68
4.2 Summary	72
<b>5 Dimple and protruded textured journal bearing</b>	<b>73</b>
5.0 Introduction	73
5.1 Comparison of performance characteristics	73
5.1.1 Comparison of present results for friction coefficient with the experimental results	73
5.1.2 Comparison based on eccentricity ratio	74
5.1.2.1 Full textured region configuration ( $0^{\circ}$ - $360^{\circ}$ )	75
5.1.2.2 First half-textured region configuration ( $0^{\circ}$ - $180^{\circ}$ )	79
5.1.2.3 Second half-textured region configuration ( $180^{\circ}$ - $360^{\circ}$ )	82
5.1.2.4 Calculation of optimum design parameters	85
5.1.3 Comparison based on load	86
5.1.3.1 Full textured region configuration ( $0^{\circ}$ - $360^{\circ}$ )	87
5.1.3.2 First half-textured region configuration ( $0^{\circ}$ - $180^{\circ}$ )	90
5.1.3.3 Second half-textured region configuration ( $180^{\circ}$ - $360^{\circ}$ )	92
5.1.3.4 Percentage change in performance characteristics	94
5.1.3.5 Pressure and film thickness profiles	96
5.2 Summary	97

<b>6</b>	<b>Concluding remarks</b>	<b>99</b>
6.0	Introduction	99
6.1	Inferences	100
6.2	Conclusions	101
6.3	Scope for future works	102
	<b>References</b>	<b>103</b>
	<b>List of publications</b>	<b>113</b>



# List of figures

<b>Fig. 1.1</b>	Textured journal bearing [1]	2
<b>Fig. 2.1</b>	Schematic diagram of the textured journal bearing (a) front view and (b) developed view of one half of bearing in the z-direction	22
<b>Fig. 2.2</b>	Geometry of spherical protruded textured journal bearing	31
<b>Fig. 2.3</b>	Flow chart of the MG method	36
<b>Fig. 2.4</b>	Flow chart of the PMD method	37
<b>Fig. 2.5</b>	Graphical representation of Lagrange interpolation	38
<b>Fig. 3.1</b>	Validation of the present results of the MG and PMD methods	41
<b>Fig. 3.2</b>	Comparison of the computational efficiency of PMD method, MG method and FMD method for $L/D = 0.2$ (a) Sommerfeld number vs. eccentricity ratio (b) Number of Iteration vs. eccentricity ratio (c) Time vs. eccentricity ratio	44
<b>Fig. 3.3</b>	Comparison of the computational efficiency of PMD method, MG method and FMD method for $L/D = 1$ (a) Sommerfeld number vs. eccentricity ratio (b) Number of Iteration vs. eccentricity ratio (c) Time vs. eccentricity ratio	46
<b>Fig. 3.4</b>	Comparison of Scheme 1 (PMD) results with the MG method and the FMD method results for $L/D = 1$ at an eccentricity ratio of 0.8	47
<b>Fig. 3.5</b>	Comparison of Scheme 2 (PMD) results with the MG method and the FMD method results for $L/D = 1$ at an eccentricity ratio of 0.8	47
<b>Fig. 3.6</b>	Comparison of Scheme 1 results for different eccentricity ratios of $L/D = 1$ at $orf = 1.8$	48
<b>Fig. 3.7</b>	Comparison of Scheme 1 and Scheme 2 computing speed for $L/D = 1$ at an eccentricity ratio of 0.8	48

<b>Fig. 3.8</b>	Comparison of the computational efficiency of PMD method, MG method and FMD method for $L/D = 2$ (a) Sommerfeld number vs. eccentricity ratio (b) Number of Iteration vs. eccentricity ratio (c) Time vs. eccentricity ratio	50
<b>Fig. 3.9</b>	Comparison of Scheme 1, MG and FMD method results for different $L/D$ ratios at an eccentricity ratio of 0.8	52
<b>Fig. 4.1</b>	Computational efficiency comparison for PMD, MG and FMD methods for texture portion of 0.4: (a) the Sommerfeld number, (b) the number of iteration, and (c) the time, versus the eccentricity ratio	56
<b>Fig. 4.2</b>	Computational efficiency comparison for PMD, MG and FMD methods for texture portion of 0.8: (a) the Sommerfeld number, (b) the number of iteration, and (c) the time, versus the eccentricity ratio	57
<b>Fig. 4.3</b>	Computational efficiency comparison for PMD, MG and FMD methods for dimple area density of 0.05: (a) the Sommerfeld number, (b) the number of iteration, and (c) the time, versus the eccentricity ratio	59
<b>Fig. 4.4</b>	Computational efficiency comparison for PMD, MG and FMD methods for dimple area density of 0.10: (a) the Sommerfeld number, (b) the number of iteration, and (c) the time, versus the eccentricity ratio	61
<b>Fig. 4.5</b>	Computational efficiency comparison for PMD, MG and FMD methods for dimple aspect ratio of 0.04: (a) the Sommerfeld number, (b) the number of iteration, and (c) the time, versus the eccentricity ratio	62

<b>Fig. 4.6</b>	Comparison of Sommerfeld number results of Scheme 1, MG method and FMD method at the dimple aspect ratio of 0.04 and an eccentricity ratio of 0.8	63
<b>Fig. 4.7</b>	Comparison of averaged pressure results of Scheme 1, MG method and FMD method at the dimple aspect ratio of 0.04 and an eccentricity ratio of 0.8	64
<b>Fig. 4.8</b>	Comparison of Sommerfeld number results of Scheme 2, MG method and FMD method at the dimple aspect ratio of 0.04 and an eccentricity ratio of 0.8	64
<b>Fig. 4.9</b>	Comparison of averaged pressure results of Scheme 2, MG method and FMD method at the dimple aspect ratio of 0.04 and an eccentricity ratio of 0.8	65
<b>Fig. 4.10</b>	Computational efficiency comparison for PMD, MG and FMD methods for dimple aspect ratio of 0.08: (a) the Sommerfeld number, (b) the number of iteration, and (c) the time, versus the eccentricity ratio	66
<b>Fig. 4.11</b>	Computational efficiency comparison for PMD, MG and FMD methods for non-dimensional clearance of 0.03: (a) the Sommerfeld number, (b) the number of iteration, and (c) the time, versus the eccentricity ratio	68
<b>Fig. 4.12</b>	Computational efficiency comparison for PMD, MG and FMD methods for non-dimensional clearance of 0.06: (a) the Sommerfeld number, (b) the number of iteration, and (c) the time, versus the eccentricity ratio	69
<b>Fig. 4.13</b>	Computational efficiency comparison for PMD, MG and FMD methods for non-dimensional Length of 30: (a) the Sommerfeld number, (b) the number of iteration, and (c) the time, versus the eccentricity ratio	70

<b>Fig. 4.14</b>	Computational efficiency comparison for PMD, MG and FMD methods for non-dimensional Length of 50: (a) the Sommerfeld number, (b) the number of iteration, and (c) the time, versus the eccentricity ratio	71
<b>Fig. 5.1</b>	Validation of the present results with the experimental results of Etsion et al. [16]	74
<b>Fig. 5.2</b>	Comparison of load carrying capacity for journal bearing with dimple and protruded textures with untextured bearing by varying texture depth for full textured region configuration	76
<b>Fig. 5.3</b>	Comparison of friction variable for journal bearing with dimple and protruded textures with untextured bearing by varying texture depth for full textured region configuration	77
<b>Fig. 5.4</b>	Comparison of flow coefficient for journal bearing with dimple and protruded textures with untextured bearing by varying texture depth for full textured region configuration	78
<b>Fig. 5.5</b>	Comparison of load carrying capacity for journal bearing with dimple and protruded textures with untextured bearing by varying texture depth for first-half textured region configuration	79
<b>Fig. 5.6</b>	Comparison of friction variable for journal bearing with dimple and protruded textures with untextured bearing by varying texture depth for first-half textured region configuration	80
<b>Fig. 5.7</b>	Comparison of flow coefficient for journal bearing with dimple and protruded textures with untextured bearing by varying texture depth for first-half textured region configuration	81
<b>Fig. 5.8</b>	Comparison of load carrying capacity for journal bearing with dimple and protruded textures with untextured bearing by varying texture depth for second-half textured region configuration	82

- Fig. 5.9** Comparison of friction variable for journal bearing with dimple and protruded textures with untextured bearing by varying texture depth for second-half textured region configuration 83
- Fig. 5.10** Comparison of flow coefficient for journal bearing with dimple and protruded textures with untextured bearing by varying texture depth for second-half textured region configuration 84
- Fig. 5.11** Film thickness and pressure profiles corresponding to the minimum and maximum loads 97





# List of tables

<b>Table 1.1</b>	Comparison of computational performance of PMD and FMD methods in terms of number of iterations	17
<b>Table 3.1</b>	The input parameters for the validation of results	40
<b>Table 3.2</b>	Range of over relaxation factor ( <i>orf</i> ) for convergence in PMD method	42
<b>Table 3.3</b>	Different Schemes for textured journal bearing ( $L/D = 0.2$ )	43
<b>Table 3.4</b>	Different Schemes for textured journal bearing ( $L/D = 1$ )	44
<b>Table 3.5</b>	Different Schemes for textured journal bearing ( $L/D = 2$ )	49
<b>Table 4.1</b>	Over-relaxation factor ( <i>orf</i> ) for the PMD and FMD methods	55
<b>Table 4.2</b>	Percentage of number of iterations and computing time taken by Scheme 1 with respect to the MG and FMD methods	72
<b>Table 5.1</b>	Parameters used for validation	75
<b>Table 5.2</b>	Parameters for the numerical study of spherical textured journal bearing	76
<b>Table 5.3</b>	Dimple and protruded textured journal bearing performance enhancement ratios	86
<b>Table 5.4</b>	Comparison of bearing operating and performance parameters for full textured region configuration	89
<b>Table 5.5</b>	Comparison of bearing operating and performance parameters for full textured region configuration in dimensional form	89
<b>Table 5.6</b>	Comparison of bearing operating and performance parameters for first-half textured region configuration	91
<b>Table 5.7</b>	Comparison of bearing operating and performance parameters for second-half textured region configuration	93

**Table 5.8** Percentage change in the performance parameters of textured journal bearings



# Notations

---

$C$	clearance, m
$D$	bearing diameter, m
$e$	eccentricity, m
$f$	friction variable
$h$	fluid film thickness, m
$\bar{h}$	non-dimensional fluid film thickness
$h_p$	dimple depth, m
$\bar{h}_p$	non-dimensional dimple depth
$h_{pl}$	local dimple depth, m
$\bar{h}_{pl}$	non-dimensional local dimple depth, m
$L$	bearing length, m
$\bar{L}$	non-dimensional length
$orf$	over relaxation factor
$p$	pressure, Pa
$\bar{p}$	non-dimensional pressure
$Q$	flow coefficient, m <sup>3</sup> /s
$\bar{Q}$	non-dimensional flow coefficient

$R$	bearing radius, m
$r_p$	dimple base circle radius, m
$r_1$	half of the imaginary square cell length, m
$\bar{r}_1$	non-dimensional half of the imaginary square cell length
$S$	Sommerfeld number
$S_p$	dimple area density
$U$	journal velocity, m/s
$W$	load carrying capacity, N
$\bar{W}$	non-dimensional load capacity
$x, z$	coordinates, m
$\bar{\theta}_1, \bar{z}$	non-dimensional coordinates
$x_1, z_1$	local coordinates, m
$\bar{x}_1, \bar{z}_1$	non-dimensional local coordinates
$\alpha$	texture portion
$\beta$	lubricant's bulk modulus, Pa
$\delta$	non-dimensional clearance
$\varepsilon$	eccentricity ratio
$\eta$	dynamic viscosity, Pa s
$\theta$	angular direction, deg

$\mu$	coefficient of friction
$\xi$	fractional film content parameter
$\rho$	lubricant density, kg/m <sup>3</sup>
$\rho_c$	lubricant density in cavitation zone, kg/m <sup>3</sup>
$\psi$	dimple aspect ratio
$\omega$	rotational speed, rad/s

### Abbreviations

DTB	Dimple Textured Bearing
EHL	Elasto-Hydrodynamic Lubrication
FMD	Fixed Mesh Densification
FT	Full textured
FHT	First-Half Textured
JFO	Jakobsson Floberg Olsson
LST	Laser Surface Texturing
MG	Multi-grid
PMD	Progressive Mesh Densification
PTB	Protruded Textured Bearing
PB	Plain Bearing
SHT	Second-Half Textured



# Abstract

---

Surface texturing is proven to be a feasible technique for enhancement of the performance characteristics of the hydrodynamic bearings. A considerable amount of numerical and experimental study is carried out on textured hydrodynamic bearings. The surface texturing onto the bearing surface can be done using different micro-fabrication techniques such as laser surface texturing (LST), chemical etching techniques, novel dressing techniques, Additive manufacturing, abrasive jet machining, photolithography, focused ion beam, micro-electric discharge machining, electrochemical texturing, ultrasonic machining, thermal implantation etc. The surface texture of regular geometries, either dimpled or protruded shapes, can be produced on the bearing surface with the above-mentioned manufacturing techniques.

The present dissertation deals with implementing a simple computational algorithm, i.e., the progressive mesh densification (PMD) method, to textured journal bearing problems. Its computational performance is compared with the multigrid (MG) and fixed mesh density (FMD) methods while implemented to spherical dimple textured journal bearing. It is found that the PMD method is superior in computational performance compared to MG and FMD methods for fixed texture parameters for length-to-diameter ( $L/D$ ) ratios of 0.2, 1 and 2 whereas, in the case of varying texture parameters for the  $L/D$  ratio of unity.

Further, the spherical protruded and dimple textured journal bearings' performance characteristics are compared with the untextured bearing ones for the  $L/D$  ratio of unity. The discretized governing Reynolds equation considering the mass conserving (JFO) boundary conditions has been solved using the computationally efficient PMD method. The numerical code developed is validated with the experimental results available in the literature. It has been noticed from the numerical analysis that the dimple textured journal bearing provides better performance compared to the protruded textured and untextured journal bearing for load carrying capacity and flow coefficient whereas, protruded textured journal bearing gives better performance compared to the dimple textured and untextured journal bearing for friction variable. For better performance, dimple and protruded textured bearings must be textured in the second-half textured region configuration.



## Introduction

---

### 1.0 State of the art

Tribology is a science that deals with the study of friction, wear, lubrication, and contact mechanics. It allows us to study the interaction of surfaces and to present solutions for crucial problems. The increasing range of tribological applications has increased the significance and interest in this field.

Textured surface application in the enhancement of contact performance is not a recent concept. For example, the movement of a shark in water is more efficient due to the presence of texture on its skin. The dimple textured surface of a golf ball also decreases drag to a greater extent and helps it to fly up to four times the distance when compared to a smooth surfaced golf ball.

Surface texturing has also significant impact on the enhancement of tribological performance of hydrodynamic bearings. There are many works in the literature related to the analysis of the random influence of roughness on the performance of the hydrodynamic bearing. It was concluded from those studies that the roughness influences the performance of bearing. The random roughness may be introduced onto the bearing's surface majorly due to surface finishing processes in production and minorly due to dust, additives in the lubricant and wear, while the roughness may be random or deterministic. The deterministic roughness known as the surface texture can be deliberately introduced on the bearing surface as depicted in Fig. 1.1 [1]. The regular surface texture in the form of micro-dimples or protuberances has pre-defined parameters for texture such as feature diameter, depth or height and area density. The different types of texture geometry can be produced on the surface of the bearings by different micro-fabrication techniques such as novel dressing techniques, laser surface texturing (LST), chemical etching techniques, photolithography, etc.

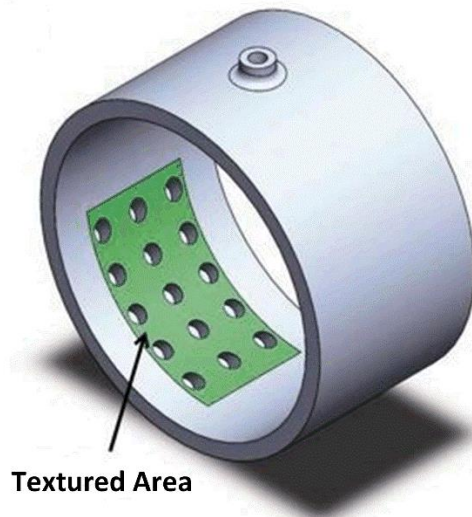


**Fig. 1.1** Textured journal bearing [1]

## **1.1 Literature review**

### **1.1.1 Effect of surface texture on slider bearing**

A slider bearing consists of two plane surfaces, one of which is stationary (fixed or pivoted) and the other of which moves with a uniform velocity, separated by a lubricating film. The direction of motion and the inclination are given in such a way that the convergent film is formed. There are many works related to the study of surface roughness or texture influence on the bearing performance characteristics. Some of the important research works related to the surface texture effect on the slider bearing's performance characteristics is discussed below.

Hargreaves [2] conducted an experimental investigation on the influence of waviness provided on the fixed surface of rectangular slider bearing on its load carrying capacity. Later compared the experimental results with the theoretical ones. From the study, it is shown that the mean discrepancy between the theoretical and experimental results is 7%. It is concluded that surface waviness improves the load carrying capacity of the bearing. However, the degree of improvement depends on the particular type of surface waviness and the tilt angle of the bearing pad.

It is important to determine the optimum texture parameters that produces the best performance of the slider bearing when it is textured. Dobrica et al. [3] carried out a numerical study to determine the optimal texture parameters such as dimple depth, texture extent and the dimple aspect for parallel and inclined slider bearings considering mass conserving (JFO) boundary conditions. The JFO boundary conditions have been implemented considering the principle of mass conservation at the interfaces between the full-film and the cavitated zones within the lubricant. Ma and Zhu [4] presented numerical and experimental analyses to obtain the optimum texture parameters for the elliptical-shaped textured parallel sliders. The authors have found the optimum texture parameters through numerical simulations, and the model built was then validated experimentally.

Yu et al. [5] conducted a numerical and experimental analysis on the influence of dimple texture geometries of various cross-sections such as circular, square and ellipse on the friction of parallel sliding surfaces. From numerical results, the authors have concluded that the dimple shape can be optimized for greater hydrodynamic pressure generation. From experimental analysis, it is concluded that the elliptical dimple gives better hydrodynamic pressure compared to the other texture geometries. The friction reduction effect also depends majorly on the texture shape. The elliptical dimple provides better friction reduction under different load and rotational speed conditions and these results showed good correlation with those obtained from the numerical model.

Fowell et al. [6] numerically studied the influence of rectangular-shaped dimple textures on infinitely long convergent bearings using mass conservation analysis. It is concluded that the surface texture influences the performance of the bearing significantly with increase in load carrying capacity and reduction in friction.

Ismail and Sarangi [7] studied the influence of surface texture orientation of negative and positive textures on the performance characteristics such as load, flow coefficient and friction variable of parallel slider bearing. From their study, the authors concluded that surface texture orientation of positive textures has a significant positive influence on bearing performance characteristics.

Gherca et al. [8] studied the effect of surface roughness and surface texture on the performance of parallel slider bearing, considering the mass conserving cavitation model. From the study, it is found that the surface roughness and surface texture have a positive impact on the performance of the bearing.

Malik and Kakoty [9] theoretically studied the influence of dimple texture on the load carrying capacity of parallel and inclined slider bearing. It is reported that when texturing is done from the front end in the width direction, a better load carrying capacity is obtained compared to texturing from the rear end regardless of the length-to-width ratio, texture portion and inclination.

Ji et al. [10] numerically studied the effect of partial surface texturing with texture geometries such as rectangular grooves, triangular grooves and parabolic grooves on the hydrodynamic pressure generated inside the parallel slider. The authors have reported that the geometric shape, groove depth and inclination of the grooves have a significant positive effect on the hydrodynamic pressure. However, the groove width has a very little positive effect on the hydrodynamic pressure.

Shen and Khonsari [11] determined optimized texture shape for maximum load carrying capacity for parallel slider bearing for both unidirectional and bidirectional sliding motion. The authors have compared the performances of optimized texture shapes with those of conventional texture shapes using mass conserving boundary conditions.

Singh et al. [12] numerically analyzed the texture parameters' effect on the slider bearing performance. The authors predicted that the better performance of the dimple textured slider bearing is attained when the bearing surface is textured with a single cylindrical dimple compared to multiple dimples.

Han and Fu [13] conducted a numerical analysis on the effect of surface texturing on the performance of the parallel slider bearing under transient conditions. They have concluded that, due to texturing, the parallel slider bearing tribological performance is greatly improved in terms of coefficient of friction and friction force.

Fu et al. [14] studied the effect of donut-shaped bump texture on the hydrodynamic performance of a parallel slider. The theoretical analysis predicted that the hydrodynamic pressure is developed as the convex of the donut-shaped bump behaves as a micro-step slider. The optimum values of bump height and horizontal spacing between adjacent textures have been determined for maximum hydrodynamic pressure.

### **1.1.2 Effect of surface texture on thrust bearing**

Thrust bearings have a number of sector-shaped pads, free to pivot, that are positioned in a circular fashion around the shaft. These provide wedge-shaped oil regions inside the bearing between the pads and a rotating disc, supporting the applied axial load and preventing metal-to-metal contact. The important works related to surface texture influence on the bearing performance characteristics of thrust bearing are presented below.

Brizmer et al. [15] theoretically studied the LST impact on the parallel thrust bearing. The optimum parameters for the dimples have been found to attain the maximum load carrying capacity. The authors have also found the best mode of LST for maximum load carrying capacity. An experimental study has also been carried out by Etsion et al. [16] on the impact of LST on the performance parameters, in terms of clearance and friction, of the parallel thrust bearing. The authors have found a good correlation between their experimental results and the theoretical results of Brizmer et al. [15]. The authors have reported that the unidirectional and bidirectional partial-LST bearing provides better performance compared to the untextured bearing with the increase in clearance and reduction in friction.

Wang et al. [17] carried out an experimental analysis to determine the optimum surface texture that enhances the load bearing capacity of the thrust bearing lubricated with water. It was found that there exist optimum texture parameters that give load bearing capacity for textured bearing as twice that of the load bearing capacity of the untextured bearing.

Etsion [18] conducted a theoretical and experimental study on the impact of surface texturing on thrust bearing performance. It is reported that friction can be substantially decreased in textured components compared to untextured ones. Buscaglia et al. [19] have studied the effect of periodic texture provided on the surface of thrust bearing on its static performance characteristics.

Rahmani et al. [20] presented an analytical study to determine the optimum geometrical parameters of square-shaped micro-dimples for the enhanced performance of partially textured parallel thrust bearings. The authors have concluded that despite the variation of different textured geometrical parameters, the optimal values of these parameters remain nearly constant.

Papadopoulos et al. [21] reported geometry optimization analysis of three-dimensional micro-thrust bearing textured with partial periodic rectangular texturing to attain maximum load carrying capacity.

Qiu and Khonsari [22] applied the mass-conservative algorithm to the thrust bearing to obtain a better understanding of the mechanisms involved and to develop a procedure for evaluating in realistic way the performance of the surfaces enhanced with dimples.

Marian et al. [23] presented theoretical and experimental analysis on the laser surface textured thrust bearing. The performance characteristics of the bearing are studied, in terms of fluid film thickness and friction torque, numerically and experimentally. From the study, it is reported that the theoretical results are in good agreement with the experimental results.

Shen and Khonsari [24] conducted a numerical and experimental investigation on the effect of internal structure shape of the cylindrical dimple on the thrust bearing specimen. From the analysis, the authors have found that the internal structure shape of the dimple has a profound influence on the load carrying capacity, but its influence on friction torque is insignificant.

Henry et al. [25] reported an experimental study to investigate the effect of surface texturing on the steady-state performance of thrust bearing. From the study, it is concluded that the textured thrust bearing reduces friction up to 30% at low loads.

Gherca et al. [26] numerically studied the influence of surface texturing on the performance of hydrodynamic thrust bearing. The mass conservative algorithm has been used to solve the governing Reynolds equation. The authors have reported that the behavior of thrust bearing is different when the stator is textured compared to when the rotor is textured. Finally,

it was found that when the rotor is textured, the performance of the thrust bearing is significantly improved under certain conditions.

Fu and Untaroiu [27] conducted a 3D-Computational Fluid Dynamic (CFD) analysis to optimize the texture parameters for elliptical textured thrust bearing performance in terms of load carrying capacity and friction coefficient, considering mass conserving boundary conditions. The authors have validated their numerical model results with the experimental results available in the literature.

Panigrahi and Sarangi [28] conducted an experimental study on the effect of texture size and height on the performance characteristics of the parallel sliding thrust bearing. The positive textures having cross-sections such as circular, elliptical, square and triangular are fabricated on bearing surfaces for experimental analysis. Their results show that the textured bearings, for all texture shapes, produce lesser frictional torque and higher clearance compared to the untextured bearing under varying loads and speeds. The test results show that when the texture height is the same, the small size textures produce better bearing performance, followed by medium and larger size textures for the given range of parameters. Also, when the texture size is the same, the greater texture height provides better performance characteristics for all texture shapes for the given range of parameters.

Zhirong et al. [29] presented a numerical analysis to determine the optimal texture shape that gives maximum load carrying capacity for the parallel thrust bearing. They have implemented mass conserving boundary conditions to solve the governing Reynolds equation. They have concluded that the chevron-shaped texture provides the maximum load carrying capacity.

### **1.1.3 Effect of surface texture on journal bearing**

A journal bearing is the most familiar of all the bearings. The sleeve of the bearing is wrapped partially or completely around the rotating journal. This bearing can support an externally applied radial load. It is due to pressure development inside the lubricant present between the rotating journal and the bearing sleeve due to the wedge action principle. Many researchers have implemented various techniques pertaining to surface texturing to improve the

performance characteristics of journal bearings. Some of the works relevant to present study are described below.

Sinanoglu et al. [30] studied theoretically and experimentally the influence of texturing the shaft on the distribution of pressure and, thus, on the load carrying capacity of journal bearing. The authors have reported that the shaft textured with trapezoidal profile produces better load carrying capacity compared to the shaft textured with saw profile.

Tala-Ighil et al. [31] conducted a numerical analysis to investigate the effect of surface texture on the journal bearing characteristics. The spherical dimple textured journal bearing characteristics are compared with those of the untextured journal bearing. From the analysis, the authors have reported that the most important bearing characteristics are affected by texturing. Also, appropriate selection of the texture parameters can have a significant impact on the bearing characteristics.

Ausas et al. [32] highlighted the importance of consideration of mass conserving boundary conditions while solving problems of textured journal bearings. The square dimpled textures are considered in the analysis. The authors have concluded that though the Reynolds model and mass conserving cavitation model yield the same results for performance characteristics of untextured bearings, in the case of micro-textured bearings, consideration of mass conserving cavitation model is crucial for the evaluation of performance characteristics.

Lu and Khonsari [33] investigated the friction characteristic of a journal bearing with dimpled bushings manufactured using machining and chemical etching techniques. A series of experimental results are presented to examine the effect of dimples on the Stribeck curve. It is shown that with proper dimples dimensions, journal bearings' friction performance can be improved, particularly for light oils. Experimental results also indicate that a bushing with etched dimples over the entire circumference offers better frictional performance than one with dimples etched on half of its circumference.

Tala-Ighil et al. [34] studied different texture geometries' effects on the performance of hydrodynamic journal bearings. The different texture geometries considered are spherical, cylindrical and parallelepiped. The authors have concluded that the parallelepiped texture

geometry provides better performance compared to other texture geometries and smooth surface.

Cupillard et al. [35] performed computational fluid dynamic analysis to predict the coefficient of friction of the textured journal bearings. The results suggest that introducing the surface texture of suitable geometry can reduce the friction coefficient.

Tala-Ighil et al. [36] conducted a theoretical analysis of the effect of textured area on the hydrodynamic journal bearing performance. The authors have considered the cylindrical texture on the surface of the bearing. The results depict that the most important properties can be improved through the proper arrangement of the textured area on the bearing surface.

The effect of different types of texture (micro-cavities) on the hydrodynamic journal bearing performance has been numerically studied by Kango et al. [37]. It has been suggested that the half wave texture (negative) on the bearing surface produces better bearing performance than that of the full wave texture (negative).

Brizmer and Kligerman [38] presented a theoretical study on the implementation of LST on journal bearings. The authors have analyzed the effect of full-LST and partial-LST on the load carrying capacity and attitude angle of the journal bearing. They have found the favorable mode of LST and optimum parameters of dimple texture for maximum load carrying capacity.

Rao et al. [39] studied the influence of texture/slip configuration on the journal bearing performance in terms of load carrying capacity and coefficient of friction. They presented a one-dimensional analysis of partially textured slip journal bearing. Partially textured slip followed by a single groove is considered on the stationary surface of the journal bearing. They concluded that considering partially textured slip configuration produces higher load carrying capacity and lower coefficient of friction. Among all the cases considered in the analysis of concentric journal bearing, the groove region followed by the partially textured slip region provides an improvement in non-dimensional load carrying capacity and a decrease in coefficient of friction.

Li and Wang [40] conducted a numerical analysis on the impact of surface texture in the form of a bulge around a dimple on the tribological properties of journal bearing. The authors have concluded that the tribological properties (friction coefficient and eccentricity ratio) of the journal bearing can be bettered with surface texturing. However, the load carrying capacity can be negatively affected.

Gupta et al. [41] carried out an experimental study on textured journal bearing performance. The authors have concluded that the performance of the journal bearing has been affected due to the textured surface i.e., pressure increases more in textured journal bearing as compared to smooth journal bearing and in the converging zone of bearing, the surface textures are more effective.

Kango et al. [42] compared the hydrodynamic performance, in terms of friction coefficient, of textured journal bearing and grooved journal bearing. The authors have reported that the micro-grooves on the bearing surface reduce the friction coefficient compared to the spherical textures.

Lu et al. [43] presented an experimental investigation on the influence of the phyllotactic pattern arrangement of textures on the friction characteristic of dimple textured journal bearing. The authors have reported that the phyllotactic pattern arrangement of textures provides better frictional performance compared to the conventional linear pattern.

Ganji and Kakoty [44] reported a numerical study on the performance characteristics of micro-elliptical dimple textured journal bearing. The authors have reported that the textured bearing provides better performance compared to the untextured bearing with proper selection of texture depth, texture area and dimple area density.

Tala-Ighil and Fillon [45] numerically investigated the influence of surface texturing on the performance parameters of journal bearing. Firstly, the authors have validated their numerical results with the experimental results available in the literature and found good agreement. The authors have concluded from their study that full-texturing does not necessarily improve performance parameters. However, at very low speeds and adequate texture sizes, full-texturing can improve the performance parameters. Partial texturing at the outlet zone can always improve the performance parameters.

Zhang et al. [46] studied the hydrodynamic effect of dimple textures on the journal bearing performance. It has been reported that the load bearing capacity can be significantly improved with partially texturing on the inlet of the bearing sleeve.

Meng et al. [47] showed the influence of compound dimples (rectangular dimple at the top and the spherical dimple at the bottom) on the performance of journal bearing in terms of load carrying capacity and friction coefficient. The performance parameters for representative rectangular-spherical compound dimples on journal bearing have been compared with those of simple rectangular dimples. It is found that the compound dimple provides better performance due to its twice hydrodynamic action compared to the simple dimple.

Liang et al. [48] carried out three dimensional CFD analysis to determine the influence of partial texture location and dimple depth on the performance parameters of partially textured journal bearing. The authors have concluded that the texture located at the lubricant inlet area can enhance the performance of the bearing and the shallow dimples give better performance than the deep ones.

Dadouche and Conlon [49] conducted an experimental investigation on the effect of surface texture on the steady-state performance characteristics of hydrodynamic journal bearing under high loads and lubricated with contaminated lubricant. From the experimental results, the authors have drawn conclusions on the advantage of dimples in capturing contaminant particles and thus decreasing the possibility of failure of bearing.

Khatri and Sharma [50] studied the effect of surface texture on the performance characteristics of non-recessed hybrid journal bearing operating with non-Newtonian lubricant. From their study, it is predicted that surface textured hole-entry hybrid journal bearing provides a reduction in minimum film thickness for lubricants such as pseudoplastic, Newtonian and dilatant compared to untextured hole-entry hybrid journal bearing.

Sharma et al. [51] studied the effect of surface texture on a couple stress fluid-based journal bearings. The authors have considered mass-conserving boundary conditions instead of Reynolds boundary conditions. It is found that texturing produces an increment in load carrying capacity only at lower eccentricity ratios for a couple stress fluid-based journal

bearing, whereas load carrying capacity is increased with a couple stress fluid in smooth journal bearing at different eccentricity ratios.

Yamada et al. [52] conducted a theoretical and experimental study on the influence of square dimple texture on the static characteristics of journal bearing. The authors have suggested that the textured journal bearings produce a lower attitude angle and higher eccentricity ratio compared to the smooth journal bearing under the same operating conditions.

Shinde and Pawar [53] implemented a multi-objective optimization technique to optimize surface texturing parameters to enhance the journal bearing performance with increasing load carrying capacity and reduction in friction coefficient.

Guo [54] theoretically studied the influence of micro-spherical and cylindrical dimple textures on the load carrying capacity and lubrication performance of the journal bearing with axial grooves using the JFO boundary conditions.

Usman and Park [55] conducted a numerical analysis to study the effect of surface textures that are transverse to the sliding direction on the performance of journal bearing at varying operating conditions. The mass conserving boundary conditions have been implemented in solving the governing Reynolds equation. The authors have reported that the frictional characteristic can be significantly improved at a slight expense of load carrying capacity.

Shinde et al. [56] presented an experimental and numerical investigation on conical shaped journal bearing with partial texturing. They have considered texture distribution from  $0^{\circ}$ - $90^{\circ}$  and  $90^{\circ}$ - $180^{\circ}$  on the bearing surface in the circumferential direction. It is predicted that the texture distribution along  $90^{\circ}$ - $180^{\circ}$  produces enhancement in the bearing performance compared to the plain journal bearing.

Mao et al. [57] performed experimental and theoretical analysis on the effect of arrangement patterns of round pits on journal bearing's tribological characteristics. The authors have reported that texturing of the bearing surface could reduce friction and wear.

The impact of chevron-shaped texture on the journal bearing performance was theoretically analyzed by Sharma et al. [58]. The authors reported that there would be an

improvement in the performance parameters if the textured region is situated in the region of pressure build-up. It was also reported that surface texturing would be more effective in improving bearing performance for the bearings operating at lower eccentricity ratios.

Galda et al. [59] conducted an experimental investigation on the effect of surface texture on the performance of journal bearings. They have found that the textured journal bearings remained in hydrodynamic lubrication for greater time and moved to mixed lubrication at lower speeds, during the shut-down, compared to smooth journal bearings.

Manser et al. [1] studied numerically the influence of cylindrical texture and non-Newtonian lubricant on the journal bearing performance using the mass-conserving boundary conditions. The results suggest that texturing in the bearing convergent zone significantly improves the bearing performance with enhancement in load carrying capacity and reduction in friction coefficient, whereas, for full-texturing, there is adverse performance.

Korenaga et al. [60] presented an experimental investigation on the frictional performance of oil-impregnated sintered bearings with surface texturing. The authors concluded that friction is low for the dimpled bearings compared to the flat bearings.

Singh and Awasthi [61] studied the influence of dimple location and depth on the hydrodynamic journal bearing performance. The authors reported that the texturing has a more significant impact on the bearing performance when it is textured in the upstream zone of  $126^{\circ}$  -  $286^{\circ}$  and for dimple aspect ratio nearer to unity.

Manser et al. [62] numerically studied the effect of surface texture on the hydrodynamic journal bearing performance using JFO boundary conditions. They demonstrated that their results were in good agreement with the bench mark results available in the literature.

Singh and Awasthi [63] theoretically investigated the influence of different dimple textures with geometrical shapes such as spherical, triangular, cylindrical and kite on the journal bearing performance. The authors mentioned that there is better improvement in the journal bearing performance when the bearing surface is textured with spherical shaped dimple textures compared to other texture shapes.

Awasthi and Mann [64] studied the effect of surface texture on the hydrodynamic journal bearing performance operating under a turbulent regime. From the results, the authors concluded that the performance of the journal bearing improves if the bearing surface is textured at a proper location.

Filho et al. [65] conducted an experimental study to determine the static performance parameters of journal bearing when its journal surface is textured with different texture geometries. From the study, the authors reported that the performance parameters are affected due to the texturing of the journal surface.

#### **1.1.4 Progressive mesh densification (PMD) method**

PMD method is the computational procedure where the computations are performed at different levels of mesh sizes. In this method, computational mesh is progressively densified, with movement of levels from lower level to higher level, to accelerate the solution process and ensure numerical accuracy. It is a simple computational method that is easy to implement. Within the PMD method itself, different Schemes may be adopted based upon the combinations of different levels to improve its computational efficiency.

Zhu [66] conducted a numerical investigation on thin-film and mixed lubrication. In this investigation, the author has presented a PMD method and compared it with the multigrid method. He concluded that the PMD method has an advantage over the multigrid method as it reduces computational time significantly for moderate and thick-film cases.

Pu et al. [67] numerically studied the mixed Elasto-hydrodynamic lubrication (EHL) implementing the PMD method. They compared their results with those from the direct iteration method with a fixed mesh and concluded that the PMD procedure has better computational performance no matter with or without surface roughness is involved. The stability of the PMD procedure is also investigated and concluded that it is stable for mixed EHL problems and capable of accelerating the numerical process, maintaining numerical accuracy.

Kumar et al. [68] implemented the PMD method to study the thermo-EHL lubrication in the Rayleigh step bearing numerically. The authors compared their results with the fixed

mesh results and concluded that implementation of PMD leads to better computational performance, with lesser number of iterations, over the fixed mesh density (FMD) method for both EHL and thermo-EHL conditions. They found out better scheme within the PMD method, which depends on the movement of levels from coarser mesh to fine mesh. Kumar et al. [69] later implemented the PMD method to investigate the combined effect of stochastic roughness, thermal effect, and elastic deformation of surfaces on Rayleigh step bearing performance. Kumar et al. [70] implemented the PMD method in their study on the influence of surface roughness and deformation on Rayleigh step bearing under thin film lubrication. Further, Kumar et al. [71] implemented the PMD method in rough thrust pad bearing under thermo-elastohydrodynamic lubrication. Kumar and Azam [72] also used the PMD method in their work on the influence of directionally oriented random roughness on the performance of a Rayleigh step bearing operating under mixed-EHL.

#### **1.1.5 Multigrid (MG) method**

Multigrid techniques are computationally efficient methods compared to the most standard iterative techniques with enormous reduction in central processing unit (CPU) time. In MG method computations are performed at different levels of mesh sizes, the mesh density going up and down repeatedly in a *V*- or *W*-cycle. Multigrid methods are difficult to implement in comparison to the PMD method.

Qiu and Khonsari [22] studied cavitation behavior in flat dimple-enhanced surfaces using the mass-conservative algorithm. The authors compared cavitation theories in predicting pressure distribution, film rupture and reformation boundaries. The authors have used multigrid method to accelerate the convergence speed.

Quinonez and Morales-Espejel [73] carried out a study to ascertain the effects of general surface roughness in wide exponential land slider bearings. The authors developed an analytical solution method and obtained full numerical results using finite difference discretization techniques and MG methods for convergence acceleration to verify the method.

Awati and Kengangutti [74] presented the thermo-hydrodynamic performance of textured journal bearing with lubricant as a couple stress fluid with the help of the MG method

to solve the modified Reynolds equation and energy equation together with the heat transfer equation. The performance parameters are estimated for different couple stress parameters.

Wang et al. [75] developed a simplified MG method based on the one presented by Venner et al. [76]. It is suggested that the algorithm can be implemented for both steady state and transient isothermal line contact EHL problems. Su et al. [77] conducted a two-dimensional Elasto-hydrodynamic numerical study on surface textured sliding bearings with relatively soft material. The authors used the MG method with a finite difference scheme to estimate the bearing performance.

Liu et al. [78] explored the MG method in depth to simulate two-dimensional EHL problems for smooth, wavy and rough surfaces. The authors considered the mass-conserving algorithm in the MG method to deal with micro-cavitations. Liu et al. [79] conducted numerical analysis on elastohydrodynamic lubrication of line contacts involving micro-cavitations using the MG method.

MG method has been used in some more works such as Ji et al. [10], Shen and Khonsari [11], Fu et al. [14], Shen and Khonsari [24], Li and Wang [40], Chang et al. [80], Venner and Lubrecht [81], Noutary et al. [82], Awati et al. [83], Liu et al. [84], Reichelt [85] etc.

### **1.1.6 Fixed mesh density (FMD) method**

In the FMD method, the governing Reynolds equation is solved in a single fixed mesh throughout the computing process till convergence. It is easy to implement and so commonly used in most of the numerical works that are available in the literature. Some of the noted works are listed here, such as Manser et al. [1], Malik and Kakoty [9], Tala-Ighil et al. [31], Ausas et al. [32], Tala-Ighil et al. [34], Tala-Ighil et al. [36], Kango et al. [37], Kango et al. [42], Ganji and Kakoty [44], tala-Ighil and Fillon [45], Zhang et al. [46], Guo [54], Manser et al. [62], Elrod [86], Fesanghary and Khonsari [87] etc.

The comparison of computational performances of PMD method with the FMD method for EHL, thermo-EHL and mixed-EHL conditions corresponding to the works of Zhu [66], Pu et al. [67] and Kumar et al. [68], are shown in Table 1.1. It is observed from Table 1.1 that the PMD method reduces the number of iterations tremendously in Mixed-EHL [66, 67] problems,

compared to the FMD method, whereas, in EHL [68] and Thermo-EHL [68] problems it reduces the number of iterations significantly.

**Table 1.1** Comparison of computational performance of PMD and FMD methods in terms of number of iterations

Lubrication Regime	Number of iterations	
	PMD	FMD
Mixed-EHL [66]	1010	2485
Mixed-EHL [67]	222	761
EHL [68]	11547	16132
Thermo-EHL [68]	12089	16984

## 1.2 Research gap

From the literature, it has been observed that the PMD method has better computational efficiency than the FMD method for solving the Reynolds equation of mixed Elasto-hydrodynamic lubrication problems, while it has better computational efficiency compared to the MG method in solving thin and mixed lubrication problems. It has also been observed from the literature that the PMD method has been implemented in thin EHL, mixed-EHL and thermo-EHL problems but not in textured hydrodynamic bearing problems. Further, it is observed from the literature that incorporating the textures on the bearing surface enhances its performance when the texture geometry, location of texture zone, texture depth/height, texture area density etc., are properly chosen. It is found that there is better improvement in the journal bearing performance when the bearing surface is textured with spherical shaped dimple textures compared to cylindrical-, triangular- and kite-shaped textures [63]. It is also observed that no attempt has been made to compare performance characteristics such as load carrying capacity, friction variable and flow coefficient of dimple textured and protruded textured journal bearing with untextured journal bearing, for spherical texture geometry, implementing mass conserving boundary conditions using the PMD method.

### **1.3 Scope of the present work**

In view of the above, an attempt has been made to carry out a numerical analysis of textured journal bearing to improve its computational efficiency and generate design data which includes the following objectives.

#### **1.3.1 Objectives**

1. To improve the computational efficiency of dimple textured hydrodynamic journal bearing using the progressive mesh densification method.
2. To study the influence of texture and bearing parameters on the computational efficiencies of PMD, MG and FMD methods while implementing to dimple textured journal bearing problems.
3. To compare the performance characteristics such as load carrying capacity, friction variable and flow coefficient of dimple textured journal bearing, protruded textured journal bearing and plain journal bearing implementing mass conserving boundary conditions using the PMD method.

### **1.4 Organization of the thesis**

The present work deals with the improvement of the computational efficiency of dimple textured journal bearing problems using the PMD method in comparison with the MG and the FMD methods. Further, the bearing performance characteristics of the dimple textured journal bearing and the protruded textured journal bearing have been compared with the untextured journal bearing. The present thesis is broadly divided into six chapters.

Chapter 1 deals with the state of the art and literature review of the previous works. The scope of the present work has been drawn based on the literature review in this chapter.

Chapter 2 presents a theory for textured journal bearing using Reynolds boundary conditions and mass conserving (JFO) boundary conditions. In the theory for textured journal bearing using Reynolds boundary conditions, the governing Reynolds equation, fluid film thickness equation for the spherical dimple textured bearing, boundary conditions, solution scheme and the equations for estimation of bearing performance parameters are presented. In

the theory for textured journal bearing using mass conserving (JFO) boundary conditions, the governing Reynolds equation, fluid film thickness equations for the spherical dimple and protruded textured bearing, solution scheme and the equations for estimation of pressure in the full film region and the bearing performance parameters are presented. Further, computational methods such as PMD and MG have been briefly discussed in chapter 2.

Chapter 3 deals with the comparison of computational efficiencies of PMD, MG and FMD methods while solving textured journal bearing problems related to different  $L/D$  ratios for a fixed set of texture parameters.

Chapter 4 presents the comparison of computational efficiencies of PMD, MG and FMD methods while solving textured journal bearing problems related to the  $L/D$  ratio of unity for varying texture parameters such as texture portion, dimple area density, dimple aspect ratio, non-dimensional clearance and non-dimensional length.

Chapter 5 deals with the comparison of performance characteristics of protruded textured journal bearing and dimple textured journal bearing, in terms of load carrying capacity, friction variable and flow coefficient, with untextured journal bearing for different texture configurations such as full textured region, first-half textured region and second-half textured region. Two ways of comparison of performance characteristics have been presented. One is based on eccentricity ratio and the other is based on load.

Finally, the major inferences and conclusions drawn from the work carried out in this thesis are presented in Chapter 6.



# Chapter 2

## Basic equations, boundary conditions and computational methods

---

---

### 2.0 Introduction

This chapter presents a theory for textured journal bearing using Reynolds boundary conditions and mass conserving (JFO) boundary conditions. In the theory for textured journal bearing using Reynolds boundary conditions, governing equation, fluid film thickness equation for the spherical dimple textured bearing, boundary conditions, solution scheme and the equations for estimation of bearing performance parameters are presented. In the theory for textured journal bearing using mass conserving (JFO) boundary conditions, governing equation, fluid film thickness equations for the spherical dimple and protruded textured journal bearing, solution scheme and the equations for estimation of pressure in the full film region and the bearing performance parameters are presented. Furthermore, the different computational methods used in the present work, such as progressive mesh densification (PMD) and multigrid (MG), have been briefly discussed in this chapter.

### 2.1 Theory for textured journal bearing using Reynolds boundary conditions

#### 2.1.1 Governing equation

The Schematic diagram of the hydrodynamic journal bearing having dimple texture on the inner surface is shown in Fig. 2.1. The front view of the dimple textured journal bearing is depicted in Fig. 2.1(a). Here, the radii of journal and bearing are  $r$  and  $R$  respectively. There is fluid lubricant filled in between journal and bearing surfaces with thickness,  $h(\theta, z)$ . The pressure is developed in the lubricant inside the bearing as the journal starts rotating with a rotational speed of  $\omega$  ( $= U/R$ ,  $U$  being the sliding velocity of the journal), under the influence of an external load  $W$ . The journal assumes a stable position after some time. The distance

between the journal and bearing centers after stability is attained is  $e$ . The magnified view depicts the micro-dimple with base circle diameter as  $2r_p$ , dimple depth as  $h_p$  and local dimple depth as  $h_{pl}$ . Figure 2.1(b) depicts the developed view of one-half of the hydrodynamic journal bearing in  $z$ -direction. The amount of texturing (texture portion) along circumferential direction is  $\alpha$ . The magnified view depicts a small imaginary square cell of the side length consisting of a micro-dimple at the center.

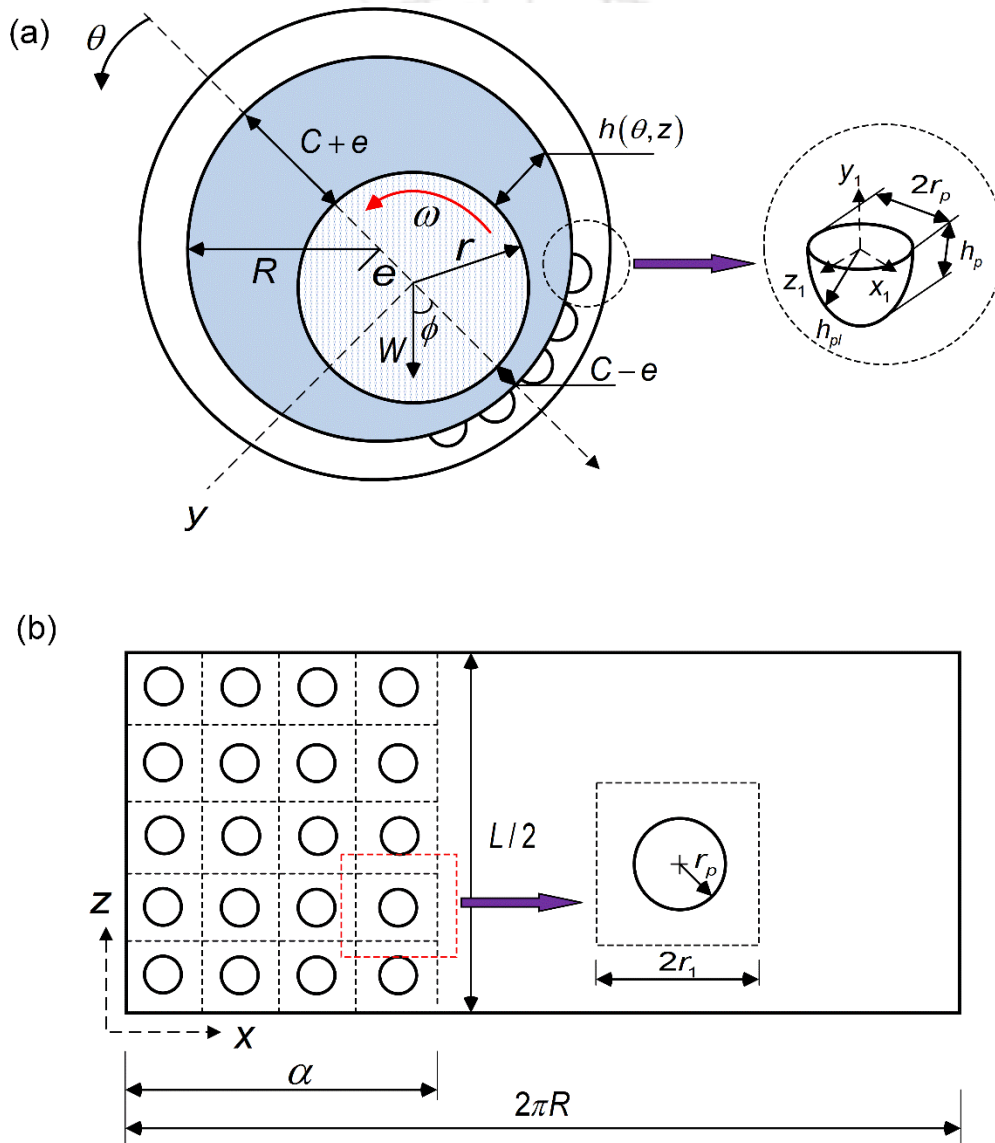


**Fig. 2.1** Schematic diagram of the textured journal bearing (a) front view and (b) developed view of one-half of bearing in the  $z$ -direction

The generalized Reynolds equation related to the hydrodynamic lubrication, where the lubricant is compressible and obeys the Newtonian law of viscosity and the flow is laminar, for an unsteady state can be written as:

$$\frac{\partial}{\partial x} \left( \rho h^3 \frac{\partial p}{\partial x} \right) + \frac{\partial}{\partial z} \left( \rho h^3 \frac{\partial p}{\partial z} \right) = 6\eta U \frac{\partial(\rho h)}{\partial x} + 12 \frac{\partial(\rho h)}{\partial t} \quad (2.1)$$

The governing Reynolds equation for the hydrodynamic journal bearing, where the lubricant is incompressible and obeys the Newtonian law of viscosity and the flow is laminar, for the steady-state case is [44]:

$$\frac{\partial}{\partial x} \left( h^3 \frac{\partial p}{\partial x} \right) + \frac{\partial}{\partial z} \left( h^3 \frac{\partial p}{\partial z} \right) = 6\eta U \frac{\partial h}{\partial x} \quad (2.2)$$

The parameters used for defining spherical dimple texture in the non-dimensional form are non-dimensional clearance  $\delta$ , non-dimensional bearing radius  $\bar{R}$ , non-dimensional local dimple depth  $\bar{h}_{pl}$ , non-dimensional film thickness  $\bar{h}$ , non-dimensional x-coordinate  $\bar{x}$ , non-dimensional z-coordinate  $\bar{z}$ , non-dimensional length  $\bar{L}$  and non-dimensional dimple aspect ratio  $\psi$ .

The non-dimensional form of the parameters mentioned above is as follows [38]:

$$\delta = \frac{C}{2r_p}; \bar{R} = \frac{R}{r_p}; \bar{h}_{pl} = \frac{h_{pl}}{C}; \bar{h} = \frac{h}{C}; \theta_1 = \frac{x}{r_p} = \bar{R}\theta; \bar{z} = \frac{z}{r_p}; \bar{L} = \frac{L}{r_p}; \psi = \frac{h_p}{2r_p} \quad (2.3)$$

After substituting non-dimensional parameters from Eqn. 2.3 in Eqn. 2.2, following non-dimensional governing Reynolds equation is obtained

$$\bar{h}^3 \frac{\partial^2 \bar{p}}{\partial \theta_1^2} + 3\bar{h} \frac{\partial \bar{p}}{\partial \theta_1} \frac{\partial \bar{h}}{\partial \theta_1} + \bar{h}^3 \frac{\partial^2 \bar{p}}{\partial \bar{z}^2} + 3\bar{h}^2 \frac{\partial \bar{p}}{\partial \bar{z}} \frac{\partial \bar{h}}{\partial \bar{z}} = \frac{1}{\delta^2} \frac{\partial \bar{h}}{\partial \theta_1} \quad (2.4)$$

where non-dimensional pressure,  $\bar{p} = \frac{2r_p p}{3\eta U}$

The dimple area density ( $S_p$ ), defined as the ratio of the area of the dimple to the area of the imaginary square cell, used in the analysis is

$$S_p = \frac{\pi r_p^2}{4r_1^2} \quad (2.5)$$

$$\frac{\bar{r}_1}{r_p} = \frac{r_1}{r_p} = \frac{1}{2} \sqrt{\frac{\pi}{S_p}} \quad (2.6)$$

Eqn. 2.4 is discretized using a central difference quotient. The pressure at each node is obtained as follows:

$$\bar{p}_{i,j} = \frac{A_{i,j} \bar{p}_{i+1,j} + B_{i,j} \bar{p}_{i-1,j} + C_{i,j} \bar{p}_{i,j+1} + D_{i,j} \bar{p}_{i,j-1} - E_{i,j}}{F_{i,j}} \quad (2.7)$$

where

$$A_{i,j} = \left( \frac{\bar{h}_{i,j}^3}{(\Delta\theta_1)^2} + \frac{3\bar{h}_{i,j}^2}{2\Delta\theta_1} \left( \frac{\bar{h}_{i+1,j} - \bar{h}_{i-1,j}}{2\Delta\theta_1} \right) \right)$$

$$B_{i,j} = \left( \frac{\bar{h}_{i,j}^3}{(\Delta\theta_1)^2} - \frac{3\bar{h}_{i,j}^2}{2\Delta\theta_1} \left( \frac{\bar{h}_{i+1,j} - \bar{h}_{i-1,j}}{2\Delta\theta_1} \right) \right)$$

$$C_{i,j} = \left( \frac{\bar{h}_{i,j}^3}{(\Delta z)^2} + \frac{3\bar{h}_{i,j}^2}{2\Delta z} \left( \frac{\bar{h}_{i,j+1} - \bar{h}_{i,j-1}}{2\Delta z} \right) \right)$$

$$D_{i,j} = \left( \frac{\bar{h}_{i,j}^3}{(\Delta z)^2} - \frac{3\bar{h}_{i,j}^2}{2\Delta z} \left( \frac{\bar{h}_{i,j+1} - \bar{h}_{i,j-1}}{2\Delta z} \right) \right)$$

$$E_{i,j} = \frac{1}{\delta^2} \left( \frac{\bar{h}_{i+1,j} - \bar{h}_{i-1,j}}{2\Delta\theta_1} \right)$$

$$F_{i,j} = \frac{2\bar{h}_{i,j}^3}{(\Delta\theta_1)^2} + \frac{2\bar{h}_{i,j}^3}{(\Delta z)^2}$$

### 2.1.2 Fluid film thickness

The general form of non-dimensional fluid film thickness considered for the textured journal bearing is

$$\bar{h}(\theta) = 1 + \varepsilon \cos(\theta) + \bar{h}_{pl} \quad (2.8)$$

The non-dimensional fluid film thickness for the dimple textured journal bearing is given as follows [38]:

$$\left. \begin{aligned} \bar{h} &= 1 + \varepsilon \cos(\theta) - \left( \frac{1}{8\psi\delta} - \frac{\psi}{2\delta} \right) + \sqrt{\left( \frac{1}{8\psi\delta} + \frac{\psi}{2\delta} \right)^2 - \frac{1}{4\delta^2} \left( (\bar{x}_1)^2 + (\bar{z}_1)^2 \right)} && \text{when } (\bar{x}_1)^2 + (\bar{z}_1)^2 < 1 \\ \bar{h} &= 1 + \varepsilon \cos(\theta) && \text{when } (\bar{x}_1)^2 + (\bar{z}_1)^2 \geq 1 \end{aligned} \right\} \quad (2.9)$$

where  $\bar{x}_1 = \frac{x_1}{r_p}$  and  $\bar{z}_1 = \frac{z_1}{r_p}$  are non-dimensional local coordinates with origin at the center of a dimple square cell.

### 2.1.3 Reynolds boundary conditions

The Reynolds boundary conditions used for the solution of the Eqn. 2.4 are as follows:

$$\left. \begin{aligned} \bar{p}(\theta, \pm \frac{\bar{L}}{2}) &= 0 \\ \bar{p}(0, \bar{z}) &= \bar{p}(2\pi, \bar{z}) \\ \frac{\partial \bar{p}}{\partial \bar{z}} &= 0 \text{ at } \bar{z} = 0 \\ \bar{p} = 0; \frac{\partial \bar{p}}{\partial \theta} &= 0 \text{ at } \theta = \theta_c \end{aligned} \right\} \quad (2.10)$$

where  $\theta_c$  is the angle at which film cavitates

In Eqn. 2.10, the first boundary condition presents that pressure at the ends in axial direction of the bearing is ambient pressure, the second boundary condition means that the pressure in circumferential direction of the bearing is same at the start and the end of the angular coordinate in the analysis, the third boundary condition depicts that the change in pressure gradient at the midplane in axial direction of the bearing is zero and the last boundary condition presents that the pressure, where the fluid film cavitates, is ambient pressure and its gradient in circumferential direction is zero.

#### 2.1.4 Solution scheme

The pressure at any node point is expressed in terms of the pressure of four adjacent points. The non-dimensional pressure at all mesh points is assumed to be zero to start with the iteration process. Gauss-Seidel method coupled with successive over relaxation (SOR) scheme has been used for solving the equations of pressure at each node satisfying the boundary conditions in Eqn. 2.10 [38]. The significance of using successive over relaxation (SOR) scheme with Gauss-Seidel method is that the convergence of the solution becomes faster; for which a parameter called over relaxation factor is used.

The Gauss-Seidel method coupled with a successive over relaxation scheme (SOR) is used to determine new pressure as follows [38]:

$$\left(\bar{p}_{i,j}\right)_{new} = \left(\bar{p}_{i,j}\right)_{old} + err_{i,j} \times orf \quad (2.11)$$

where,

error is  $err_{i,j}$  = Right-hand side (R.H.S) of Eqn. 2.7 -  $\left(\bar{p}_{i,j}\right)_{old}$  and  $orf$  is the over relaxation factor. The ' $orf$ ' value needs to be considered in between 1 and 2 for the above-mentioned method whereas, for Gauss-Seidel method its value becomes unity.

The Convergence criterion used is as follows:

$$\frac{\left| \left(\sum \bar{p}_{i,j}\right)_{M-1} - \left(\sum \bar{p}_{i,j}\right)_M \right|}{\left| \left(\sum \bar{p}_{i,j}\right)_M \right|} \leq 10^{-5} \quad (2.12)$$

### 2.1.5 Bearing performance parameters

The load carrying capacity components and load carrying capacity are given below [38]:

$$\left. \begin{aligned} \bar{W}_x &= -2\bar{R} \int_0^{\bar{L}/2} \int_0^{2\pi} \bar{p} \cos \theta d\theta d\bar{z} \\ \bar{W}_z &= 2\bar{R} \int_0^{\bar{L}/2} \int_0^{2\pi} \bar{p} \sin \theta d\theta d\bar{z} \\ \bar{W} &= \sqrt{\bar{W}_x^2 + \bar{W}_z^2} \end{aligned} \right\} \quad (2.13)$$

The Sommerfeld number is a bearing performance parameter that is used in the design of hydrodynamic journal bearings. It is very important in lubrication analysis as it contains all the design variables specified by the designer. The Sommerfeld number equation is given as follows [38]:

$$S = \frac{\bar{L}}{6\pi\bar{W}} \left( \frac{\bar{R}}{\delta} \right)^2 \quad (2.14)$$

Load carrying capacity is obtained numerically through double integration using Simpsons 1/3 rule. Using Simpson's 1/3 rule, the approximate solution to the definite integral can be obtained through quadratic approximation of the function or integrand.

## 2.2 Theory for textured journal bearing using mass conserving (JFO) boundary conditions

### 2.2.1 Governing equation

In the theory of lubrication, the Reynolds equation is employed for determining the pressure distribution of viscous fluid films. Assuming that the lubricant obeys the Newtonian law of viscosity and the flow is laminar, the governing Reynolds equation for the journal bearing operating at steady state condition can be written as:

$$\frac{\partial}{\partial x} \left( \rho h^3 \frac{\partial p}{\partial x} \right) + \frac{\partial}{\partial z} \left( \rho h^3 \frac{\partial p}{\partial z} \right) = 6\eta U \frac{\partial \rho h}{\partial x} \quad (2.15)$$

where  $p$  is the local pressure,  $h$  is the fluid film thickness,  $\eta$  is the viscosity,  $\rho$  is the density and  $U$  is the sliding speed.

In the full-film region, assuming the density of the lubricant to be constant, the Eqn. 2.15 becomes [87]:

$$\frac{\partial}{\partial x} \left( h^3 \frac{\partial p}{\partial x} \right) + \frac{\partial}{\partial z} \left( h^3 \frac{\partial p}{\partial z} \right) = 6\eta U \frac{\partial h}{\partial x} \quad (2.16)$$

In the cavitation region, since the pressure remains constant at the cavitation pressure, thus for this region Eqn. 2.15 reduces to [87]:

$$\frac{\partial \rho h}{\partial x} = 0 \quad (2.17)$$

The film rupture and reformation neglected in Reynolds boundary conditions are considered with the implementation of mass conserving boundary conditions. The mass conserving boundary conditions proposed by Jakobsson, Floberg and Olsson provides a more realistic solution than the Reynolds boundary conditions [87].

To implement the mass conserving boundary conditions, Elrod [86] has introduced a new parameter called fractional film content  $\xi (= \rho/\rho_c)$  that would combine two Eqns. 2.16 and 2.17 into a single 'universal' partial differential equation (PDE) that covers both the full-film and the cavitated regions. However, a switch function 'g' is necessary to make the resulting PDE consistent with the uniform pressure assumption within the cavitated zone. Therefore, a switch function 'g' has been proposed by Elrod [86] and later it was modified by Fesanghary and Khosari [87] to improve numerical instability and avoid convergence issues. In the present analysis, the modified switch function of Fesanghary and Khosari [87] has been used.

The resulting mass conservative form of the Reynolds equation can be written as follows [87]:

$$\frac{\partial}{\partial x} \left[ \beta h^3 g(\xi) \left( \frac{\partial \xi}{\partial x} \right) \right] + \frac{\partial}{\partial z} \left[ \beta h^3 g(\xi) \left( \frac{\partial \xi}{\partial z} \right) \right] = 6\eta U \frac{\partial \xi h}{\partial x} \quad (2.18)$$

where  $\beta = \rho \frac{\partial p}{\partial \rho}$  is the lubricant's bulk modulus.

The discretized form of Eqn. 2.18 has been obtained from the work of Fesanghary and Khonsari [87], where they have employed a Finite difference scheme for discretization.

The discretized equation is presented below:

$$\xi_{i,j} = \frac{A_1 \xi_{i-1,j} + A_2 \xi_{i+1,j} + A_3 \xi_{i,j-1} + A_4 \xi_{i,j+1} + B_1 + B_2 + B_3}{A_5} \quad (2.19)$$

where

$$A_1 = \frac{U}{2\Delta x} \left[ (1 - g_{i-1,j}) h_{i-1,j} \right] + \frac{\beta}{12\eta(\Delta x)^2} \left[ g_{i-1,j} h_{i-1/2,j}^3 \right]$$

$$A_2 = \frac{\beta}{12\eta(\Delta x)^2} \left[ g_{i+1,j} h_{i+1/2,j}^3 \right] \quad A_3 = \frac{\beta}{12\eta(\Delta z)^2} \left[ g_{i,j-1} h_{i,j-1/2} \right] \quad A_4 = \frac{\beta}{12\eta(\Delta z)^2} \left[ g_{i,j+1} h_{i,j+1/2} \right]$$

$$A_5 = \frac{U}{2\Delta x} \left[ (1 - g_{i,j}) h_{i,j} \right] + \frac{\beta}{12\eta(\Delta x)^2} \left[ g_{i,j} (h_{i+1/2,j}^3 + h_{i-1/2,j}^3) \right] + \frac{\beta}{12\eta(\Delta z)^2} \left[ g_{i,j} (h_{i,j+1/2}^3 + h_{i,j-1/2}^3) \right]$$

$$B_1 = \frac{U}{2\Delta x} \left[ \frac{g_{i-1,j} (2 - g_{i,j})}{2} h_{i-1,j} + \frac{g_{i,j} (g_{i-1,j} - 2 + g_{i+1,j})}{2} h_{i,j} - \frac{g_{i+1,j} g_{i,j}}{2} h_{i+1,j} \right]$$

$$B_2 = \frac{\beta}{12\eta(\Delta x)^2} \left[ -g_{i-1,j} h_{i-1/2,j}^3 + g_{i,j} (h_{i+1/2,j}^3 + h_{i-1/2,j}^3) - g_{i+1,j} h_{i+1/2,j}^3 \right]$$

$$B_3 = \frac{\beta}{12\eta(\Delta z)^2} \left[ -g_{i,j-1} h_{i,j-1/2}^3 + g_{i,j} (h_{i,j+1/2}^3 + h_{i,j-1/2}^3) - g_{i,j+1} h_{i,j+1/2}^3 \right]$$

### 2.2.2 Fluid film thickness

The general form of fluid film thickness is given as follows:

$$h = h_s \pm h_t \quad (2.20)$$

where  $h_s (= C + e \cos \theta)$  is fluid film thickness for plain journal bearing,  $h_t$  is the local depth/height for texture, the '+' sign is for dimple texture and the '-' sign is for protruded texture.

The fluid film thickness for spherical texture is given below:

$$h = h_s \pm \left\{ \begin{array}{l} h_p - \left( \frac{r_p^2 + h_p^2}{2h_p} \right) + \sqrt{\left( \frac{r_p^2 + h_p^2}{2h_p} \right)^2 - ((x_1)^2 + (z_1)^2)} \quad \text{when } (x_1)^2 + (z_1)^2 < r_p^2 \\ h_p \quad \text{when } (x_1)^2 + (z_1)^2 \geq r_p^2 \end{array} \right\} \quad (2.21)$$

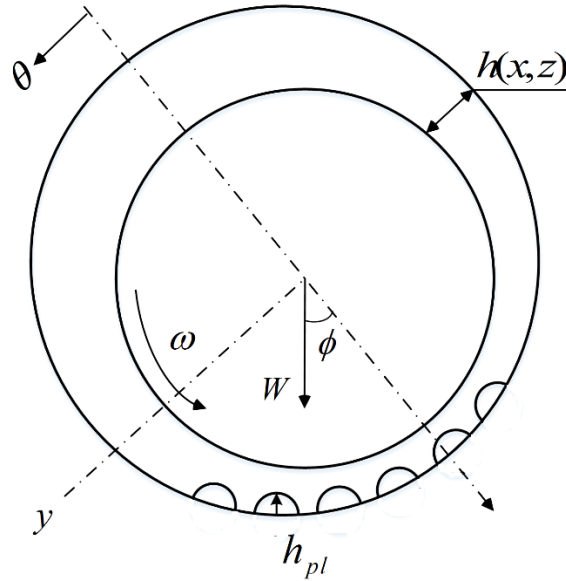
where  $x_1 = x - r_1$  and  $z_1 = z - r_1$  are local coordinates with origin at the center of the square cell having the length as ' $2r_1$ ', the '+' sign is for spherical dimple texture and the '-' sign is for spherical protruded texture.

Figure 2.2 represents the geometry of a spherical protruded textured journal bearing highlighting the significant bearing and texture parameters. For geometry of spherical dimple textured journal bearing, Fig. 2.1 in Sec. 2.1 may be referred.

In this case, half of the length of the unit square cell is given as follows:

$$r_1 = \sqrt{\frac{\pi r_p^2}{S_p}} \quad (2.22)$$

where  $S_p$  is dimple area density and  $r_p$  is the base circle radius of the spherical dimple



**Fig. 2.2** Geometry of spherical protruded textured journal bearing

### 2.2.3 Solution scheme

Here, the Gauss-Seidel iterative method coupled with a successive over-relaxation (SOR) scheme has been implemented to solve Eqn. 2.19 for fractional film content parameter ' $\xi$ '. The finite difference grid is selected in such a way that it is fine enough to capture the film rupture and reformation boundaries accurately. The mass conserving boundary conditions implementation has two convergence criteria to be satisfied; one for the film content parameter ' $\xi$ ' at the inner loop and the other for the switch function 'g' at the outer loop [87]. The ultimate error tolerance for the film content parameter is taken as  $10^{-5}$  whereas the switch function is said to be converged when the present iteration values for 'g' repeats with the previous iteration ones. In the present study, the modified switch function proposed by Fesanghary and Khonsari [87] is used to improve convergence stability.

### 2.2.4 Pressure in the full film region

As the cavitated region in the bearing contains gaseous and vapor content the pressure in that region is cavitation pressure. However, as the full film region in the bearing is filled with lubricant the pressure in that region is greater than cavitation pressure.

The pressure in the full film region can be determined, after solving Eqn. 2.19 for film content parameter ‘ $\xi$ ’, from the equation given below [87]:

$$p_{i,j} = p_c + \beta \ln \xi_{i,j} \quad (2.23)$$

where  $p_c$  is the cavitation pressure

### 2.2.5 Non-dimensional bearing parameters

After the non-dimensionalization, the pressure and the fluid film thickness in non-dimensional form can be obtained in the following way:

$$\bar{p} = \frac{pC^2}{\eta UR} \quad (2.24)$$

$$\bar{h} = \frac{h}{C} \quad (2.25)$$

Here, non-dimensional coordinates are  $\bar{x} = \frac{x}{R}$  and  $\bar{z} = \frac{z}{L}$ .

The non-dimensional load carrying capacity components and load carrying capacity is given below:

$$\left. \begin{aligned} \bar{W}_x &= - \int_0^1 \int_0^{2\pi} \bar{p} \cos \theta d\theta d\bar{z} \\ \bar{W}_z &= \int_0^1 \int_0^{2\pi} \bar{p} \sin \theta d\theta d\bar{z} \\ \bar{W} &= \sqrt{\bar{W}_x^2 + \bar{W}_z^2} \end{aligned} \right\} \quad (2.26)$$

The friction variable can be found from the equation below:

$$f = \mu \left( \frac{R}{C} \right) = \frac{1}{\bar{W}} \int_0^1 \int_0^{2\pi} \left( \frac{\bar{h}}{2} \frac{\partial \bar{p}}{\partial \theta} + \frac{1}{\bar{h}} \right) d\theta d\bar{z} \quad (2.27)$$

The non-dimensional flow can be obtained from the equation below:

$$\bar{Q} = -\frac{1}{12} \left( \frac{D}{L} \right)^2 \int_0^{2\pi} h^{-3} \frac{\partial \bar{p}}{\partial z} d\theta \quad (2.28)$$

### 2.2.6 Performance enhancement ratio (PER)

PER is the parameter that provides the effectiveness of texturing the bearing surface compared to untextured bearing in terms of load carrying capacity and friction variable in combination. Higher the value of PER better is the performance.

In the present study, based upon the PER presented in Sharma et al. [58], the PER is given as follows:

$$PER = \frac{\left( \frac{\text{Load carrying capacity of textured bearing}}{\text{Load carrying capacity of untextured bearing}} \right)}{\left( \frac{\text{Friction variable of textured bearing}}{\text{Friction variable of untextured bearing}} \right)} \quad (2.29)$$

### 2.3 Multigrid (MG) method

The MG algorithm of V-cycle, for three level situation, where the coarser grid has half of the grid points and the coarsest grid has one-fourth of the grid points of the finest grid, concerning Sec. 2.1, is described in detail in the following steps [22].

1. The Gauss-Seidel iteration scheme is applied to the system of equations (Eqn. 2.7), at finest level, a few times. It gives an approximate solution of  $\bar{p}_{i,j}$  at every node (i, j).

The Residual at each node can be calculated from the equation:

$$R_{i,j} = F_{i,j} \bar{p}_{i,j} - (A_{i,j} \bar{p}_{i+1,j} + B_{i,j} \bar{p}_{i-1,j} + C_{i,j} \bar{p}_{i,j+1} + D_{i,j} \bar{p}_{i,j-1} - E_{i,j}) \quad (2.30)$$

2. The Residual  $R$  is transferred to the coarser grid using the restrictor operator, which is given as

$$Res = \begin{bmatrix} 1/16 & 1/8 & 1/16 \\ 1/8 & 1/4 & 1/8 \\ 1/16 & 1/8 & 1/16 \end{bmatrix} \quad (2.31)$$

The resulting residual can be expressed in the following form

$$R_{i,j}^1 = \frac{1}{16}(R_{i+1,j+1} + R_{i+1,j-1} + R_{i-1,j+1} + R_{i-1,j-1}) + \frac{1}{8}(R_{i+1,j} + R_{i-1,j} + R_{i,j+1} + R_{i,j-1}) + \frac{1}{4}R_{i,j} \quad (2.32)$$

3. The equations on the coarser grid are obtained by replacing  $E_{i,j}$  in Eqn. 2.7 with  $R_{i,j}^1$  and solving for the corresponding pressures having their respective coefficient terms on the coarser grid. Here, Gauss-Seidel relaxation scheme is implemented a few times.
4. Steps 2 and 3 are repeated on the coarsest level.
5. The solution obtained on the coarsest level is transferred back to the coarser level. The coarsest level nodes sitting in the place of coarser level nodes are directly transferred to the coarser level, whereas the intermediate nodes of the coarser level are interpolated using the following interpolation operator.

$$Pr = \begin{bmatrix} 1/4 & 1/2 & 1/4 \\ 1/2 & 1 & 1/2 \\ 1/4 & 1/2 & 1/4 \end{bmatrix} \quad (2.33)$$

6. The values in the matrix represent the weight of the coarsest grid node in the intermediate nodes of the coarser grid. After prolongation, the correction to the pressures at the coarser grid is obtained. The latest pressure values are obtained by adding the correction to the previous pressures at the coarser grid.
7. The Gauss-Seidel relaxation scheme is applied a few times to refine the results.
8. Steps 5 and 6 are repeated on the finest grid.

The procedure described above is for one V-cycle and the same procedure has to be repeated until the convergence criterion for pressures is satisfied. The flow chart of the MG method is illustrated in Fig. 2.3.

## 2.4 Progressive mesh densification (PMD) method

The PMD method and the MG method are theoretically similar. Using an iterative relaxation procedure, the errors whose wavelengths are of the order of mesh size can be rapidly reduced. But, the errors whose wavelengths are far away from mesh spacing may take more time to diminish. If the error wavelength is not comparable to mesh size, then the error may often barely decline, and consequently, after a few iterations, the convergence slows down and the asymptotic convergence rate may become very small. That is why different mesh levels are needed to speed up the solution process. However, there is a prime difference between the PMD and the MG, that is, in the MG, mesh density goes up and down in the form of a V- or W-cycle, whereas in the PMD method mesh density varies from lower to higher mesh density with gradually improving mesh density step by step till the desired mesh density is reached [67].

In the PMD method, the computational procedure is started with a lower level ( $N=1$ ) with lower mesh density and it eventually moves towards higher levels ( $N=2, 3$ ) until the highest mesh density is attained. The Lagrange interpolation technique is used to transfer the locally converged solution from the lower level to the higher level. This process of convergence and interpolation at each level repeats till the ultimate solution is attained in the highest mesh density. Figure 2.4 shows the procedure followed in the PMD method in the form of a flow chart.

To start with the PMD method, the mesh size for the initial level has to be selected. Since the texture bearing governing equation is a 2-dimensional one, the mesh size ( $m \times n$ ) is to be selected. The divisions in the axial direction ( $n$ ) are selected and the divisions in the circumferential direction follow from the relationship between  $m$  and  $n$ , i.e.,  $m = (2\pi n)/(L/D)$  which ensures that the grid selected is square. The mesh size ( $m \times n$ ) for level 1 is found so that the minimum number of iterations is required to achieve the loose convergence criterion ( $error \leq 10^{-3}$ ) and the solution obtained is nearer to the exact solution. With the optimized mesh size ( $m \times n$ ) for level 1, the first approximate solution is obtained quickly, which eventually ensures that the converged target solution at the highest mesh density is also attained quickly.

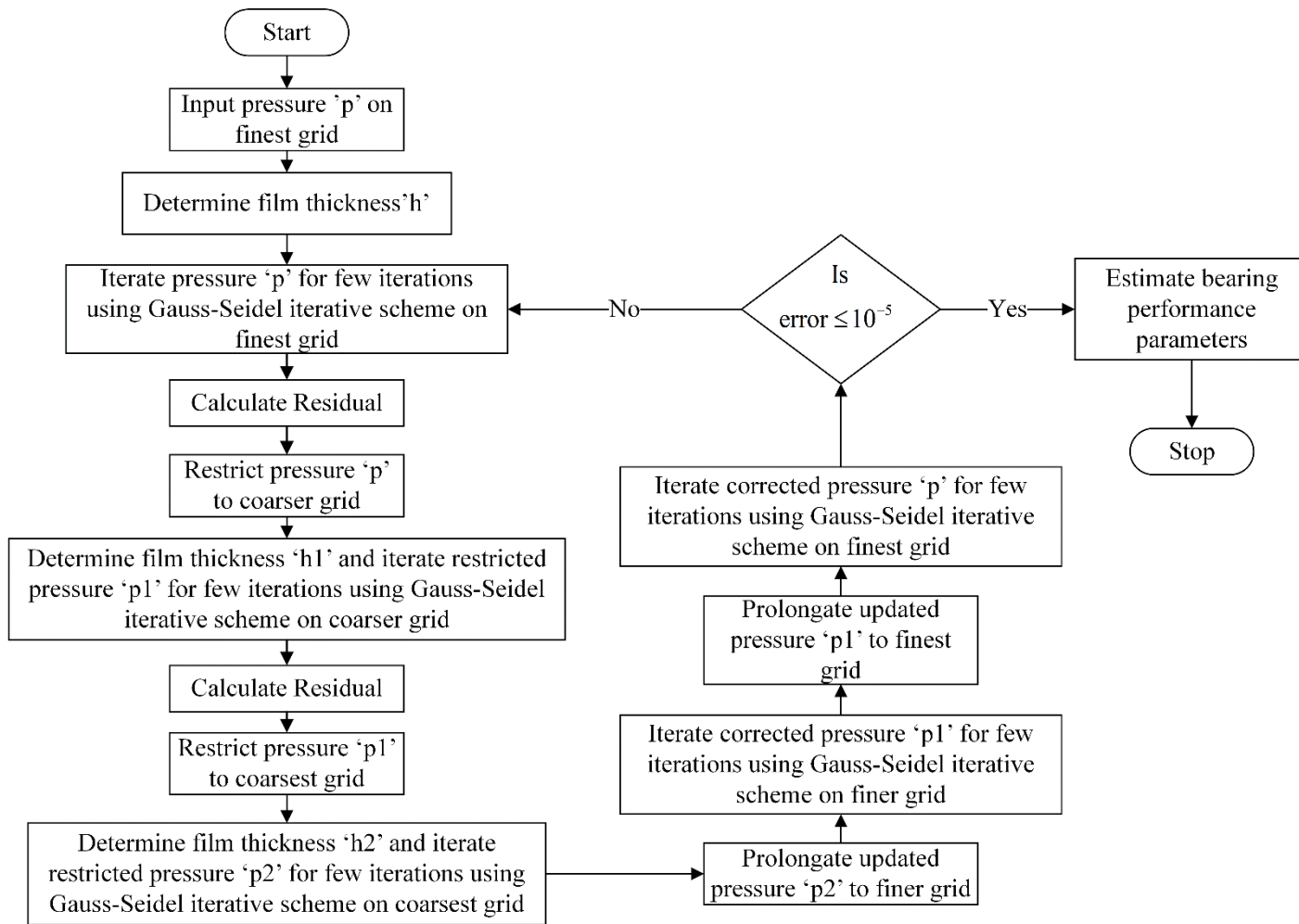


Fig. 2.3 Flow chart of the MG method

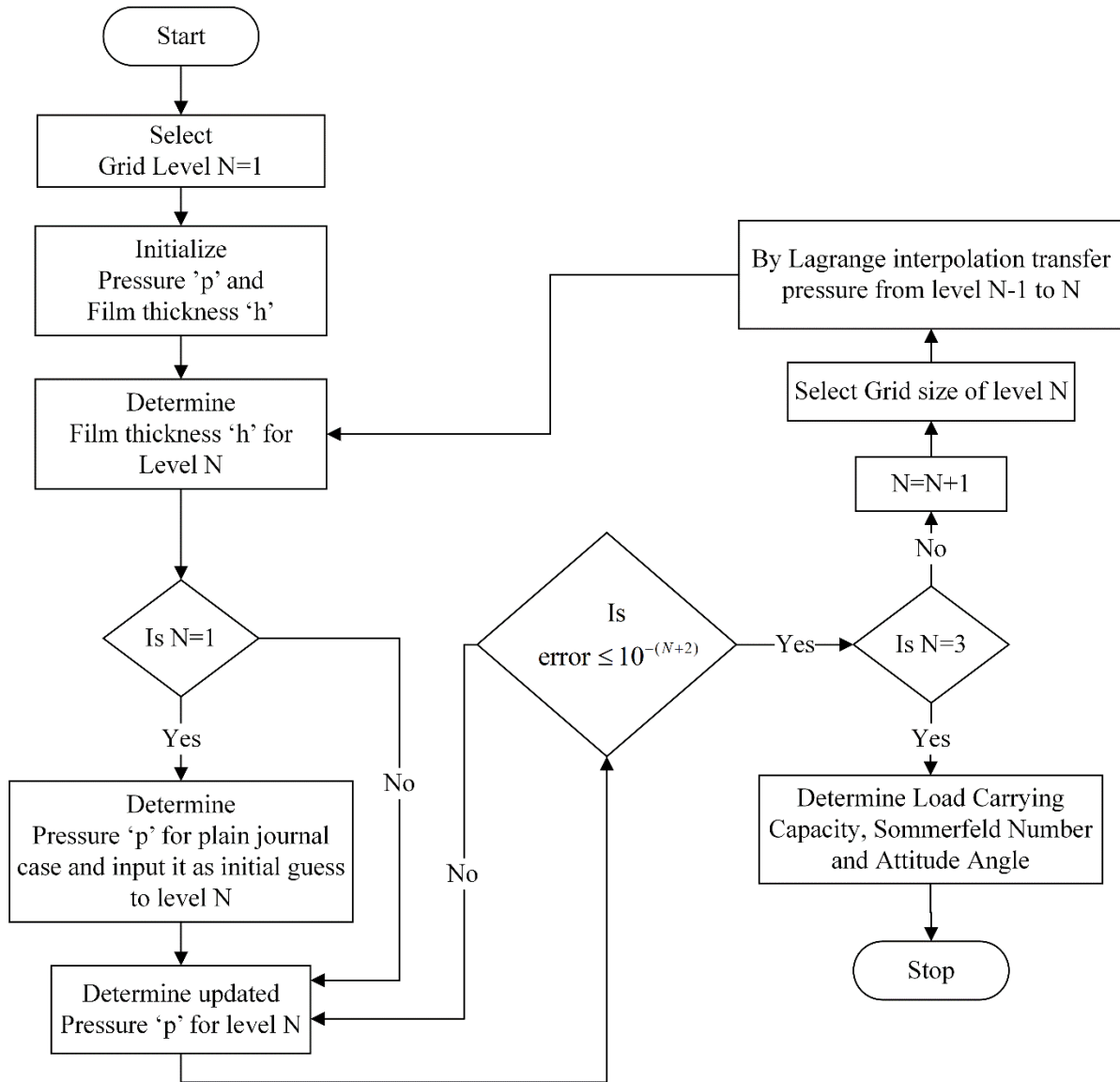


Fig 2.4 Flow chart of the PMD method

### 2.4.1 Lagrange interpolation

The Lagrange interpolation in graphical representation is depicted in Fig. 2.5. In the graph  $f(x)$  and  $x_i$  represents the pressure function and distance of the nodes from the inlet, respectively.

In Lagrange interpolation, if the pressures at two node points are known, then the pressure at the intermediate node points can be found with the help of the following formula.

$$p_x = \frac{(x-x_2)}{(x_1-x_2)} p_1 + \frac{(x-x_1)}{(x_2-x_1)} p_2 \quad (2.34)$$

where

$p_x$  is the pressure at an intermediate node at a distance of  $x$  from the inlet

$p_1$  is the pressure at node 1 at a distance of  $x_1$  from the inlet

$p_2$  is the pressure at node 2 at a distance of  $x_2$  from the inlet

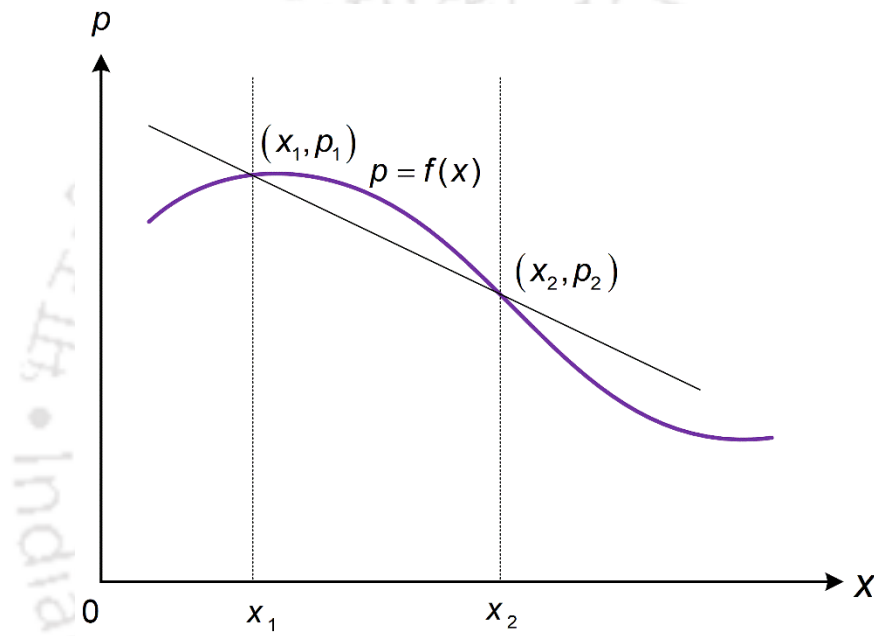


**Fig. 2.5** Graphical representation of Lagrange interpolation

## 2.5 Summary

Theories for textured journal bearing, using Reynolds boundary conditions and JFO boundary conditions, are discussed in this chapter. The governing Reynolds equation, fluid film thickness equation, solution scheme and formulations for estimating bearing performance parameters related to both theories are presented. Further, computational methods such as PMD and MG are discussed briefly in this chapter. The equations mentioned above, formulations and computational methodologies are used in the following three chapters.

# Chapter 3

## A Computational algorithm for textured journal bearing: progressive mesh densification (PMD) and multigrid (MG)

---

### 3.0 Introduction

There are several methods used to estimate the performance characteristics of textured bearings. However, Progressive Mesh Densification (PMD) method is not yet used for textured journal bearings, while it has been used for mixed elastohydrodynamic lubrication (EHL) and thermo-EHL problems. Therefore, the PMD method is implemented to estimate the performance parameters of the textured journal bearing for different  $L/D$  ratios for the fixed set of texture parameters. Its computational performance is compared with the computational performance of multigrid (MG) and the fixed mesh density (FMD) methods and is found to be very effective in improving computational efficiency in some cases of  $L/D$  ratios. The theory pertaining to Sec. 2.1 is applicable to this study.

### 3.1 Comparison of computational efficiencies for different $L/D$ ratios

The PMD, MG and FMD methods are used to estimate the bearing performance parameters for the textured journal bearing with fixed texture parameters such as non-dimensional clearance  $\delta = 0.05$ , dimple aspect ratio  $\psi = 0.06$ , dimple area density  $S_p = 0.13$ , over relaxation factor  $orf = 1.8$ , texture portion  $\alpha = 1$ , non-dimensional length  $\bar{L} = 20$  for  $L/D$  ratios of 0.2, 1 and 2. The schematic diagram for the dimple textured journal bearing may be referred to as Fig. 2.1 in Chapter 2.

The Sommerfeld number obtained for PMD (Scheme 1) and MG methods are compared with those of Brizmer and Kligerman [38], for validation, for both textured and untextured bearings, as depicted in Fig. 3.1. The input parameters and their values considered for the validation study are shown in Table 3.1. It is observed from Fig. 3.1 that the present results predicted by PMD and MG methods are very close to that of Brizmer and Kligerman [38]. Therefore, the codes developed for the PMD and MG methods have been implemented to obtain the solution of problems pertaining to dimple textured journal bearing.

In validation, to avoid convergence issues for the texture case of the PMD method, the plain journal bearing results of pressure converged to a loose convergence criterion ( $error \leq 10^{-3}$ ) at the coarsest grid are provided as input pressure values. However, in the case of the MG method, the texture bearing results of pressure itself converged to a loose convergence criterion ( $error \leq 10^{-3}$ ) at the coarsest grid are interpolated to the finest grid and provided as input pressure values.

**Table 3.1** The input parameters for the validation of results

Parameters	Value
Length-to-Diameter ratio, $L/D$	0.2
Non-dimensional clearance, $\delta$	0.05
Dimple aspect ratio, $\psi$	0.06
Dimple area density, $S_p$	0.13
Texture portion, $\alpha$	1
Non-dimensional length, $\bar{L}$	20
Over-relaxation factor ( <i>orf</i> ) for PMD	1.7
PMD, Mesh Sizes	754x24, 1508x48, 3016x96
MG, Mesh Sizes	3016x96, 1508x48, 754x24

The over relaxation factor (*orf*) influences the speed of convergence of the solution (see Sec. 2.1.4). So, it is necessary to find the *orf* range in which the solution converges faster for the PMD method. For the numerical process to accelerate, the *orf* should be considered

between 1 to 2. Table 3.2 depicts the range of  $orf$ , for Schemes 1 and 2 of the PMD method, for different  $L/D$  ratios. Scheme 1 is the movement of levels from the lowest mesh density (level 1) to higher mesh density (level 2) and ultimately to the highest mesh density (level 3). Scheme 2 is the direct movement of levels from the lowest mesh density (level 1) to the highest mesh density (level 3). Since the numerical analysis is carried out for textured journal bearings, the range of  $orf$  is found for textured bearings ( $L/D = 0.2, 1$  and  $2$ ) only. However, the  $orf$  range for the non-textured bearing of  $L/D = 0.2$  has been found as it has been considered for validation. For textured bearing ( $L/D = 0.2$ ), Scheme 1 has no convergence for  $orf$  varying from 1.1 to 1.5 and Scheme 2 has no convergence for  $orf$  varying from 1.1 to 1.5 and 1.9. However, for other cases, there is no convergence issue for  $orf$  beyond the mentioned range in Table 3.2, except that the convergence takes more time.

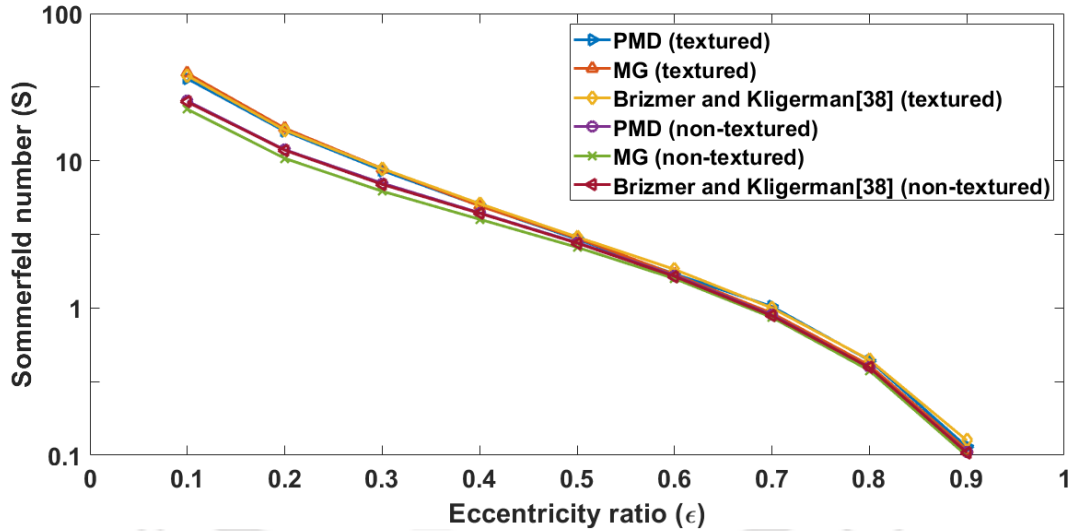


**Fig. 3.1** Validation of the present results of the MG and PMD methods

The mesh convergence study for different  $L/D$  ratios of a textured journal bearing is carried out. In case of  $L/D$  ratio of 0.2, the mesh convergence takes place at the finest mesh size of  $3140 \times 100$ . However, in the PMD method, to satisfy the condition that the first approximate solution should be nearer to the final solution and also to avoid convergence issues, the mesh size of  $3016 \times 96$  has been selected. In the case of  $L/D$  ratios of 1 and 2, the mesh convergence takes place at the finest mesh sizes of  $1132 \times 180$  and  $502 \times 160$ , respectively. In both cases of  $L/D$  ratios of 1 and 2, the condition in the PMD method that the first approximate solution should be nearer to the final solution is taken care of.

**Table 3.2** Range of over relaxation factor (*orf*) for convergence in PMD method

L/D	Texture		Non-texture	
	Scheme 1	Scheme 2	Scheme 1	Scheme 2
0.2	1.6 - 1.9	1.6 - 1.8	1.1 - 1.9	1.1 - 1.9
1	1.4 - 1.8	1.4 - 1.8	-	-
2	1.3 - 1.8	1.3 - 1.8	-	-

### 3.1.1 Comparison of computational efficiencies for $L/D = 0.2$

Table 3.3 shows the movement of levels from lower to higher, for two different schemes in the PMD method, with the movement of the number of divisions in the z-direction for  $L/D = 0.2$ . As levels move from one level to another, the number of divisions get doubled in the PMD method, starting from the number of divisions in the z-direction with 24 and subsequent levels having 48 and 96 divisions. The number of divisions in  $\theta$  direction can be obtained from the relationship between  $m$  and  $n$ , i.e.,  $m = (2\pi n)/(L/D)$ . In the PMD method, the level 1 grid size is  $754 \times 24$ , the level 2 grid size is  $1508 \times 48$  and the level 3 grid size is  $3016 \times 96$  for  $L/D = 0.2$ . The computational performance of the PMD method is compared with the MG and FMD methods for the textured bearing of  $L/D = 0.2$ , as shown in Fig. 3.2. In the MG method, the V-cycle style with three levels has been used to determine the computational performance. The top level is meshed with the finest mesh of  $3016 \times 96$ , whereas the bottom level has been meshed with the coarsest mesh of size  $754 \times 24$  and the intermediate level has been meshed with a coarser mesh of  $1508 \times 48$  mesh size. In the PMD method and the MG method, the initial pressure values are obtained similarly, as mentioned in validation. In the FMD method, the computational performance has been estimated at  $3016 \times 96$  mesh size at  $orf = 1.7$ . However, to start with the procedure of the FMD method, the results of pressure for plain journal bearing at the mesh size of  $3016 \times 96$  are given as initial pressure values to avoid convergence problems for higher eccentricity ratios. Hence the majority of the number of iterations required for convergence constitutes the iterations to obtain input pressure values.

The Sommerfeld number has been estimated to find how close PMD method results are to MG and FMD ones for  $L/D = 0.2$ , as shown in Fig. 3.2(a). The Scheme 1 and 2 results for the Sommerfeld number have a negligible difference at all eccentricity ratios varying from

0.1 to 0.9. There is a negligible difference between the Sommerfeld number results of the PMD and the MG method for eccentricity ratios of 0.4 and 0.6, whereas, for other eccentricity ratios, there is a little difference. There is a negligible difference in Sommerfeld number results for Scheme 1 and Scheme 2 compared to the FMD method results for eccentricity ratios varying from 0.3 to 0.6 and 0.9, whereas for other eccentricity ratios, there is a slight difference. From Fig. 3.2(b) and Fig. 3.2(c), it is evident that the MG method has moderately better computational performance at all eccentricity ratios over scheme 1 and scheme 2, in terms of both the number of iterations and computational time, and it has much better computational performance when compared to FMD method. It is observed from Fig. 3.2(b) that the MG method has moderately less number of iterations compared to both schemes of the PMD method and much less number of iterations compared to the FMD method. In Scheme 1, the number of iterations is less compared to Scheme 2 at all eccentricity ratios. It is observed from Fig. 3.2(c) that computational time in the MG method is moderately less compared to Scheme 1 and Scheme 2 of the PMD method and much less compared to the FMD method at all the eccentricity ratios. The computational time in Scheme 1 is less compared to Scheme 2 for all eccentricity ratios. Since the MG method has better computational performance compared to Scheme 1, Scheme 2 and the FMD methods, it can be implemented to estimate the bearing performance parameters of textured journal bearing for  $L/D = 0.2$ .

**Table 3.3** Different Schemes for texture journal bearing ( $L/D = 0.2$ )

Schemes	Movement of Levels	Movement of Divisions (n)
Scheme 1	1 → 2 → 3	24 → 48 → 96
Scheme 2	1 → 3	24 → 96

### 3.1.2 Comparison of computational efficiencies for $L/D = 1$

Table 3.4 depicts the movement of levels from lower to higher, for two different schemes of the PMD method, with the movement of the number of divisions in z-direction for the textured bearing of  $L/D = 1$ . The number of divisions considered in z-direction for levels from lower to higher is 45, 90 and 180, respectively. Consequently, the lower level grid size is 283x45, the intermediate level grid size is 566x90 and the higher-level grid size is 1132x180.

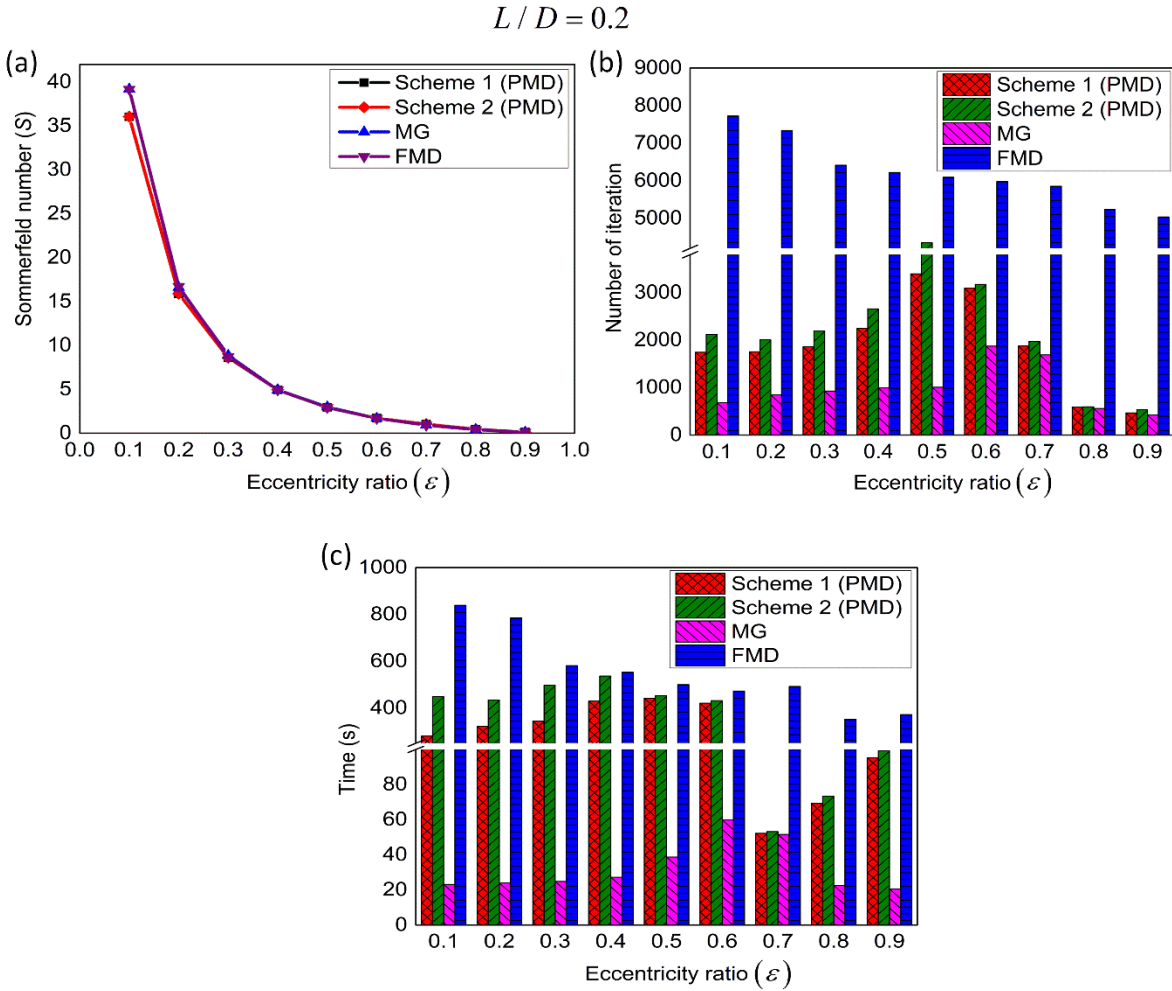


**Fig. 3.2** Comparison of the computational efficiency of PMD method, MG method and FMD method for  $L/D = 0.2$  (a) Sommerfeld number vs. eccentricity ratio (b) Number of Iteration vs. eccentricity ratio (c) Time vs. eccentricity ratio

**Table 3.4** Different Schemes for texture journal bearing ( $L/D = 1$ )

Schemes	Movement of Levels	Movement of Divisions ( $n$ )
Scheme 1	1 → 2 → 3	45 → 90 → 180
Scheme 2	1 → 3	45 → 180

The computational performance of the PMD method has been compared with the MG and the FMD method for the textured bearing of  $L/D = 1$ , as shown in Fig. 3.3. The mesh sizes considered for different levels of the V-cycle MG method are 1132x180 for the top level,

566x90 for the intermediate level and 283x45 for the bottom level. In the PMD method, the initial guess values of pressure are obtained similarly as mentioned in validation. However, in the case of the MG method, the plain bearing results of pressure converged to a loose convergence criterion ( $error \leq 10^{-3}$ ) at the coarsest grid are interpolated to the finest grid and provided as input pressures. In the FMD method, the mesh size considered is 1132x180. The plain journal bearing results of pressure at the mesh size of 1132x180 are provided as input pressure values for texture case, in the FMD method, in a similar way as it is done for texture bearing of  $L/D = 0.2$ . It has been observed from Fig. 3.3(a) that the Scheme 1 results of Sommerfeld number have a little difference compared to Scheme 2 ones, for eccentricity ratios varying from 0.1 to 0.5 and no difference at all for eccentricity ratios varying from 0.6 to 0.9. The PMD method results have a slight difference with the MG method results for all eccentricity ratios. There is a slight deviation in Sommerfeld number results compared to FMD method results for both Scheme 1 and Scheme 2 for eccentricity ratios varying from 0.1 to 0.8 with the exception of an eccentricity ratio of 0.9. It is evident from Fig. 3.3(b) and Fig. 3.3(c) that the number of iterations and computational time for Scheme 1 are lesser compared to Scheme 2 and moderately lesser compared to the MG method, whereas compared to the FMD method they are much lesser. It is observed from Fig. 3.3(b) that the number of iterations required for Scheme 1 of the PMD method to reach the converged solution is less than 88% and 6% that of the MG and the FMD method, respectively. For Scheme 2 of the PMD method, the number of iterations required for computation to reach the converged solution is less than 91% and 7% that of the MG and the FMD method, respectively. It can be seen from Fig. 3.3(c) that the time of computing for Scheme 1 and Scheme 2 is less compared to MG method and much less compared to the FMD method at all eccentricity ratios. Scheme 1 has lesser computational time compared to Scheme 2 for all eccentricity ratios varying from 0.1 to 0.9. Scheme 1 can be used to estimate the performance parameters of textured journal bearing of  $L/D = 1$  as it has better computational efficiency compared to Scheme 2, the MG method and the FMD method.

To illustrate the computational efficiency of the PMD method in a better way, for textured journal bearing of  $L/D = 1$ , the computational efficiencies of Scheme 1 and Scheme 2 of the PMD are compared with the MG and FMD methods for an eccentricity ratio of 0.8 as

shown in Fig. 3.4 and Fig. 3.5, respectively. The average non-dimensional pressure (mean of pressure values at all nodes) at each iteration versus the number of iterations is depicted in these figures. Since the fluid film thickness is constant for every iteration in the present analysis, it hasn't been considered for obtaining these figures, whereas Pu et al. [64] have considered average film thickness in their case, as it is time dependent and varies at every iteration.

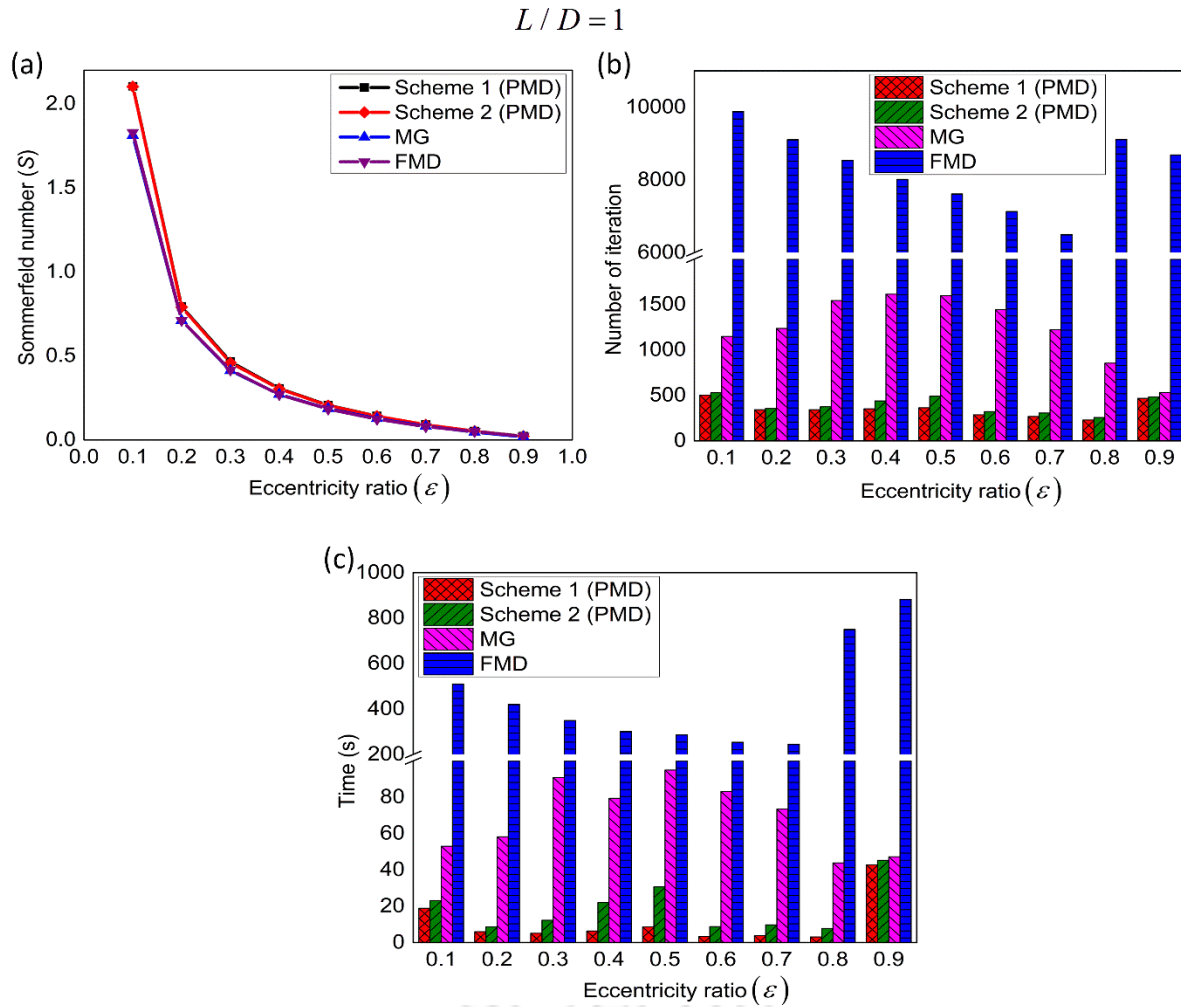


**Fig. 3.3** Comparison of the computational efficiency of PMD method, MG method and FMD method for  $L/D = 1$  (a) Sommerfeld number vs. eccentricity ratio (b) Number of Iteration vs. eccentricity ratio (c) Time vs. eccentricity ratio

Figure 3.6 depicts the comparison of Scheme 1 results for different eccentricity ratios of texture journal bearing ( $L/D = 1$ ) at  $\text{orf} = 1.8$ . It is observed from Fig. 3.6 that the number

of iterations for computing is minimum for the case of eccentricity ratio of 0.8 when compared to other eccentricity ratios of 0.2, 0.4 and 0.6.

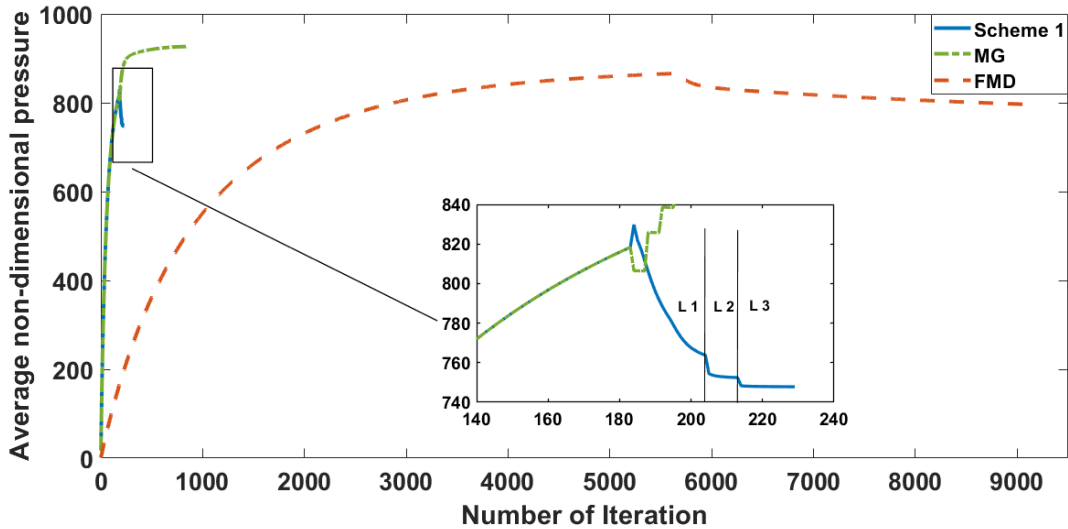


Fig. 3.4 Comparison of Scheme 1 (PMD) results with the MG method and the FMD method results for  $L/D = 1$  at an eccentricity ratio of 0.8

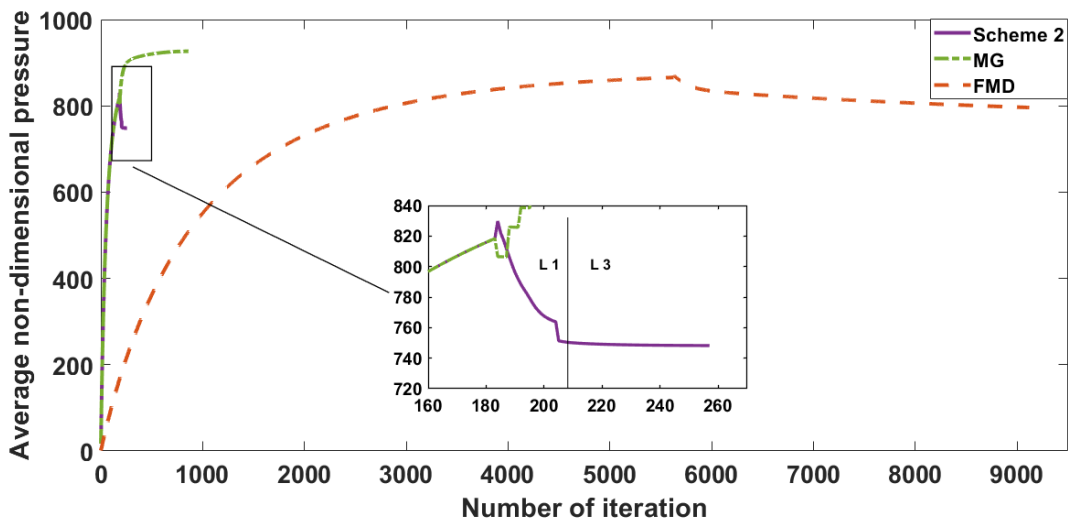
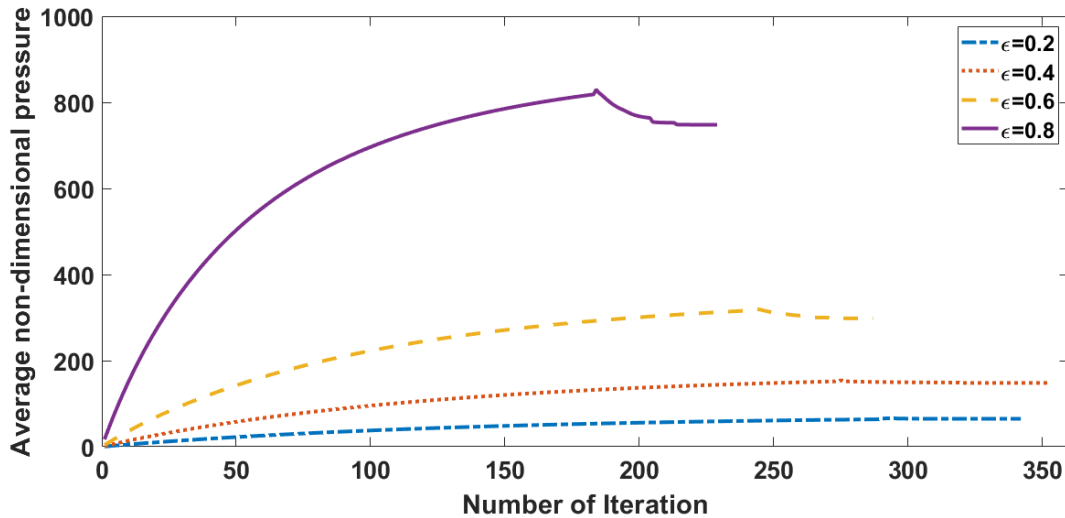


Fig. 3.5 Comparison of Scheme 2 (PMD) results with the MG method and the FMD method results for  $L/D = 1$  at an eccentricity ratio of 0.8

The computing speeds of Scheme 1 (PMD), with respect to MG and FMD methods, have been compared with that of Scheme 2 computing speeds for textured journal bearing of  $L/D = 1$  at an eccentricity ratio of 0.8 as shown in Fig. 3.7. The ratio of time of computing for

the MG method ( $T_m$ ) to time of computing for the PMD method ( $T_p$ ) gives the computing speed of the PMD method with respect to the MG method. Similarly, the computing speed of the PMD method with respect to the FMD method can be found. The computing speeds of Scheme 1, with respect to the MG and FMD methods, are 14.2 and 242, respectively, whereas the computing speeds of Scheme 2 are 5.7 and 97.4, respectively.



**Fig. 3.6** Comparison of Scheme 1 results for different eccentricity ratios of  $L/D = 1$  at  $orf = 1.8$

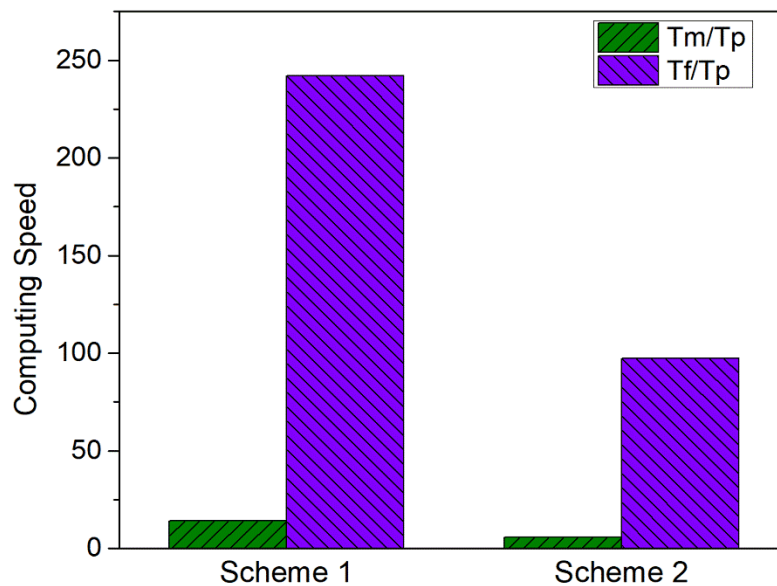


**Fig. 3.7** Comparison of Scheme 1 and Scheme 2 computing speed for  $L/D = 1$  at an eccentricity ratio of 0.8

### 3.1.3 Comparison of computational efficiencies for $L/D = 2$

The movement of levels and movement of the number of divisions in the z-direction, for two different Schemes of PMD method, has been shown in Table 3.5 for textured journal bearing of  $L/D = 2$ . The process of selection of mesh size for different levels in the PMD method is the same as explained above for the case of  $L/D = 0.2$ .

**Table 3.5** Different Schemes for texture journal bearing ( $L/D = 2$ )

Schemes	Movement of Levels	Movement of Divisions ( $n$ )
Scheme 1	1 → 2 → 3	40 → 80 → 160
Scheme 2	1 → 3	40 → 160

For textured journal bearing of  $L/D = 2$ , Fig. 3.8 depicts the computational efficiency of Schemes 1 and 2 compared with the MG method and the FMD method. In the PMD method, computation is performed at a level 1 grid size of  $126 \times 40$ , then for successive levels at  $252 \times 80$  and  $504 \times 160$ , respectively. In the MG method, the computation is performed at the grid sizes of  $504 \times 160$  for the top level,  $252 \times 80$  for the intermediate level and  $126 \times 40$  for the bottom level. In the PMD method, the initial guess values of pressure are obtained similarly as mentioned in validation. However, in the case of the MG method, the plain bearing results of pressure converged to a loose convergence criterion ( $error \leq 10^{-3}$ ) at the coarsest grid are interpolated to the finest grid and provided as input pressures. The mesh size considered in the FMD method is  $504 \times 160$ . For the initial guess values of pressures in the FMD method, the same procedure as mentioned above, for texture bearings of  $L/D$  ratios 0.2 and 1, has been followed. It is evident from Fig. 3.8(a) that the Sommerfeld number results of Scheme 1, compared to Scheme 2 have been the same for most of the eccentricity ratios from 0.1 to 0.9, with a negligible difference at eccentricity ratios of 0.1 and 0.3, when compared to the MG method ones, there is a negligible difference at eccentricity ratios of 0.1, 0.3 and 0.8 and slight variation at other eccentricity ratios. The estimated Sommerfeld number for Schemes 1 and 2 has a little variation with the results of the FMD method for eccentricity ratios of 0.1 to 0.3, negligible variation at eccentricity ratios of 0.4 and 0.9 and no variation for the rest of the eccentricity ratios. It has been observed from Fig. 3.8(b) that for Scheme 1, the number of

iterations is less compared to Scheme 2, MG method and FMD method. Scheme 1 and Scheme 2 have a lesser number of iterations compared to MG and FMD methods. It is seen from Fig. 3.8(c) that the computing time for Scheme 1 is lesser compared to Scheme 2 for all eccentricity ratios. Both Scheme 1 and Scheme 2 have lesser computing time compared to MG and FMD methods for all eccentricity ratios. Since Scheme 1 has better computational performance compared to Scheme 2, MG and FMD methods, the bearing performance parameters can be estimated using Scheme 1 for textured journal bearing of  $L/D = 2$ .

MG method has better computational performance compared to both Schemes of the PMD method and the FMD method for  $L/D = 0.2$ , whereas Scheme 1 has better computational

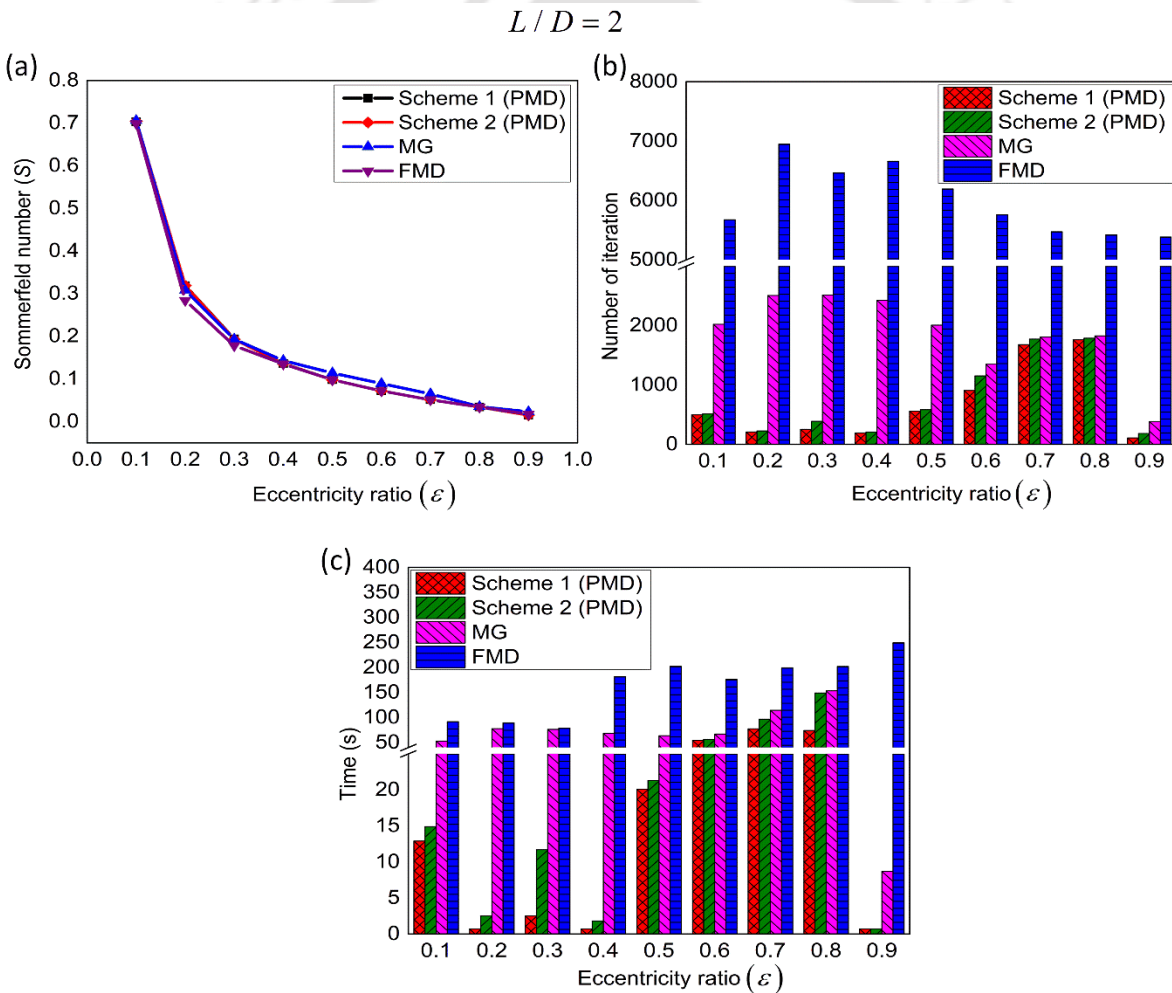


**Fig. 3.8** Comparison of the computational efficiency of PMD method, MG method and FMD method for  $L/D = 2$  (a) Sommerfeld number vs. eccentricity ratio (b) Number of Iteration vs. eccentricity ratio (c) Time vs. eccentricity ratio

performance compared to Scheme 2, the MG method and the FMD method for  $L/D$  ratios 1 and 2. The MG method is computationally efficient, in the case of  $L/D$  ratio of 0.2, compared to both schemes of the PMD method and the FMD method, it is may be due to different way of estimating input pressure values for MG method in case of  $L/D$  ratio of 0.2 than in cases for  $L/D$  ratios of 1 and 2. In case of  $L/D$  ratio of 0.2, the textured bearing results of pressure itself converged to a loose convergence criterion ( $error \leq 10^{-3}$ ) at the coarsest grid are interpolated to the finest grid and provided as input pressures. However, in case of  $L/D$  ratios of 1 and 2, the plain bearing results of pressure converged to a loose convergence criterion ( $error \leq 10^{-3}$ ) at the coarsest grid are interpolated to the finest grid and provided as input pressures. The two different ways of estimating input pressure values for MG method, in case of  $L/D$  ratio of 0.2 and  $L/D$  ratios of 1 and 2, have been followed so that the number of iterations and computing time to obtain the ultimate pressure results are minimum and also convergence issues to obtain the ultimate pressure results are avoided.

Figure 3.9 shows the comparison of Scheme 1, MG and FMD method results for different  $L/D$  ratios at corresponding optimum  $orf$  values at an eccentricity ratio of 0.8. It has been observed from Fig. 3.9 that the convergence of results occurs at the minimum number of iterations of 229 for Scheme 1 of  $L/D = 1$ , and the maximum number of iterations of 9118 are taken for convergence for the FMD method of  $L/D = 1$ .

The computational process is carried out using MATLAB, with a processor having configurations of Intel® Core™ i7-3770 CPU @ 3.40 GHz 3.90, RAM of 4 GB.

### 3.2 Summary

In the present work, the comparison of computational efficiencies, in terms of the number of iterations and computational time, of PMD, MG and FMD methods has been done for the textured journal bearing problems for different  $L/D$  ratios of 0.2, 1 and 2 for the fixed texture parameters. It is found that the PMD method is the computationally efficient one compared to MG and FMD methods for textured journal bearings of  $L/D = 1$  and 2, whereas the MG method

is a better one in computational performance compared to PMD and FMD methods for textured journal bearing of  $L/D = 0.2$ .

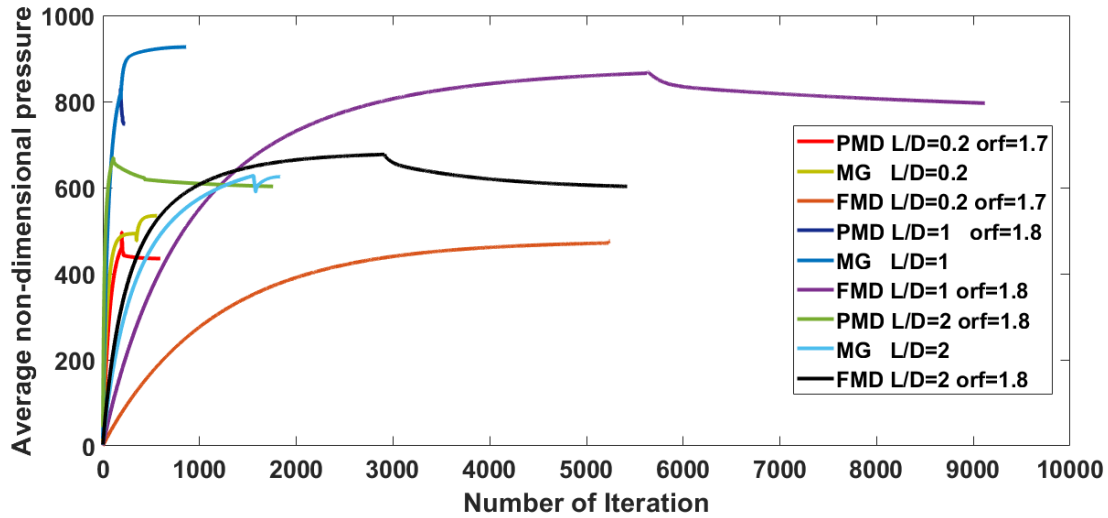
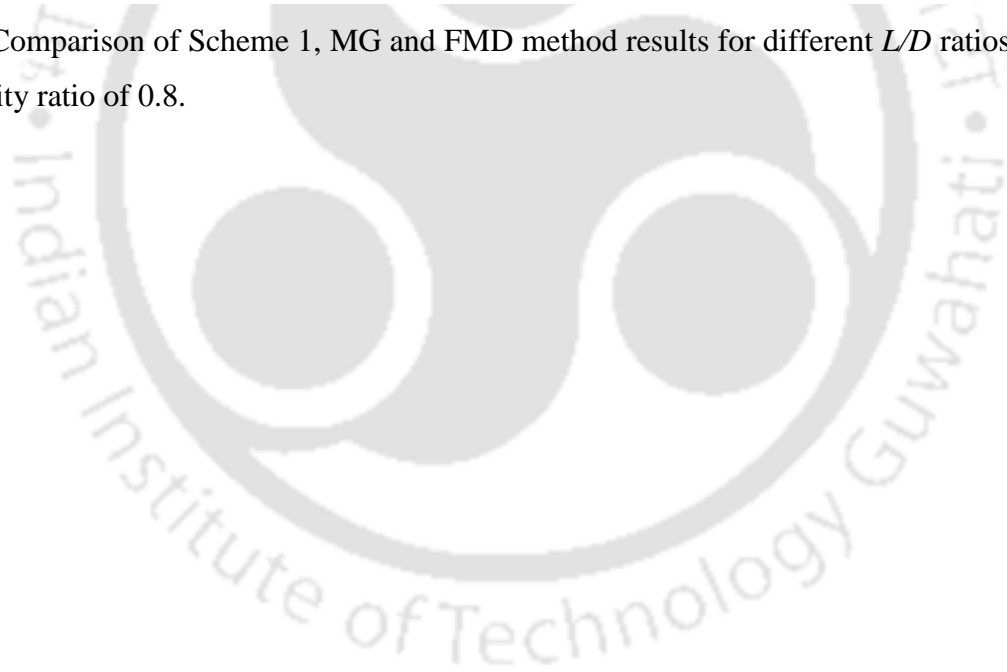


**Fig. 3.9** Comparison of Scheme 1, MG and FMD method results for different  $L/D$  ratios at an eccentricity ratio of 0.8.



# Chapter 4

## Influence of texture parameters on computational efficiencies of PMD, MG and FMD methods

---

### 4.0 Introduction

The comparison of computational efficiencies of the progressive mesh densification (PMD), multigrid (MG) and fixed mesh density (FMD) methods has been carried out for the fixed set of texture parameters for different  $L/D$  ratios in Chapter 3. Here, in this chapter, the influence of texture parameters such as texture portion, dimple area density, dimple aspect ratio, non-dimensional clearance and non-dimensional length on the computational efficiencies of PMD, MG and FMD methods has been investigated for dimple textured journal bearing of  $L/D$  ratio of unity. The theory pertaining to Sec. 2.1 is applicable to this study.

### 4.1 Influence of texture parameters

The influence of texture parameters on the computational efficiencies, in terms of the number of iterations and computational time, of PMD, MG and FMD methods for dimple textured journal bearing of  $L/D$  ratio of unity has been studied. The different cases corresponding to texture parameters such as texture portion, dimple area density, dimple aspect ratio, non-dimensional clearance and non-dimensional length are investigated as presented in the following sub-sections.

Here, the computational procedure has been performed using MATLAB, with a processor having configurations of Intel® Core™ i7-3770 CPU @ 3.40 GHz 3.90 and 4 GB RAM.

The mesh sizes considered in PMD, MG and FMD methods are the same as for the  $L/D$  ratio of unity in the fixed texture parameters study in chapter 3. However, a brief description of mesh size selection is presented below.

In the PMD method, with a maximum of three levels of mesh refinement considered, two schemes such as Scheme 1 and Scheme 2 have been used for the solution of the textured journal bearing problem. In Scheme 1, the movement of levels is such as level 1, level 2 and level 3. However, in Scheme 2, the levels move directly from level 1 to level 3, skipping level 2. Since, in the PMD method, as we move up from one level to the next level, the mesh size gets doubled, the mesh sizes considered in Scheme 1 for level 1, level 2 and level 3 are 283x45, 566x90 and 1132x180, respectively. The mesh sizes considered for level 1 and level 3, in Scheme 2, are 283x45 and 1132x180, respectively.

In the MG method, the three-level situation of the V-cycle has been considered having top-level meshed with the finest mesh of 1132x180, intermediate level meshed with the coarser mesh of 566x90 and bottom level meshed with the coarsest mesh of 283x45. The FMD method has been implemented with a mesh size of 1132x180.

Here, to avoid convergence issues, the pressures obtained for plain bearing at the coarsest mesh of PMD that are converged to loose convergence criterion ( $error \leq 10^{-3}$ ) are provided as input pressure values. However, in the case of the MG method, the pressures obtained for plain bearing at the same coarsest mesh of PMD are interpolated to the finest mesh size and provided as input pressure values.

It is necessary to find out the over-relaxation factor ( $orf$ ) for which the solution converges efficiently with a lesser number of iterations and less computational time. Therefore, the over-relaxation factor ( $orf$ ) has been found out for the PMD method such that the convergence issues are avoided and the solution is obtained with a lesser number of iterations and less computational time. In the FMD method also, the over-relaxation factor has been found for which the results are obtained with a lesser number of iterations and less computational time. In the MG method, the over relaxation factor ( $orf$ ) should be considered as unity as a standard procedure. The over-relaxation factor ( $orf$ ) considered, in the present

study, for Scheme 1 and Scheme 2 of PMD and FMD methods while implementing to different cases of texture parameters has been presented in Table 4.1.

**Table 4.1** Over-relaxation factor (*orf*) for the PMD and FMD methods

Texture parameters Method	Texture portion ( $\alpha$ )		Dimple area density ( $S_p$ )		Dimple aspect ratio ( $\psi$ )		Non-dimensional clearance ( $\delta$ )		Non-dimensional length ( $\bar{L}$ )	
	0.4	0.8	0.05	0.1	0.04	0.08	0.03	0.06	30	50
Scheme 1	1.8	1.8	1.8	1.8	1.8	1.8	1.7	1.8	1.7	1.7
Scheme 2	1.8	1.8	1.8	1.8	1.8	1.8	1.7	1.8	1.7	1.7
FMD	1.9	1.8	1.9	1.9	1.9	1.8	1.9	1.8	1.9	1.9

#### 4.1.1 Influence of texture portion

The effect of texture portion on the computational efficiencies of PMD, MG and FMD methods is studied for two cases of texture portion ( $\alpha$ ) of 0.4 and 0.8, as depicted in Fig. 4.1 and Fig. 4.2, respectively. The other non-dimensional parameters considered constant are dimple area density ( $S_p$ ) = 0.13, dimple aspect ratio ( $\psi$ ) = 0.06, non-dimensional clearance ( $\delta$ ) = 0.05 and non-dimensional length ( $\bar{L}$ ) = 20.

Figure 4.1(a) depicts the comparison of Sommerfeld number results obtained from Scheme 1 and Scheme 2 of the PMD method, MG method and FMD method for texture portion of 0.4. It shows that Scheme 1 and Scheme 2 predicted the same Sommerfeld number results for all eccentricity ratios except for 0.2 and 0.3, with a negligible difference. The MG method predicted the Sommerfeld number having a slight difference from that of Scheme 1, Scheme 2 and FMD method at all eccentricity ratios. The FMD method results also have a slight difference from that of Scheme 1 and Scheme 2 of the PMD method at most of the eccentricity ratios. Figures 4.1(b) and 4.1(c) shows the computational efficiency, in terms of the number of iterations and computing time, of Scheme 1, Scheme 2, MG method and FMD method for the texture portion of 0.4. It is evident from Fig. 4.1(b) that Scheme 1 has better computational performance in terms of the number of iterations compared to Scheme 2, MG method and FMD method at all eccentricity ratios except at 0.6 compared to Scheme 2 where both the schemes

predicted the same result. It is also evident that Scheme 1 takes the least number of iterations to get a converged solution followed by Scheme 2, MG method and FMD method. From Fig. 4.1(c), it is shown that Scheme 1 also takes lesser computational time compared to Scheme 2 at all eccentricity ratios, whereas it takes moderately lesser computational time compared to the MG method and greatly lesser computational time compared to the FMD method at all eccentricity ratios. The number of iterations for the MG and FMD methods is greater than 1.23 and 13.94 times that of Scheme 1, respectively. The Scheme 1 computing speed (ratio of computational time of Scheme 1 to computational time of compared method) is at least 2.31 and 22.86 compared to the MG and FMD methods, respectively.

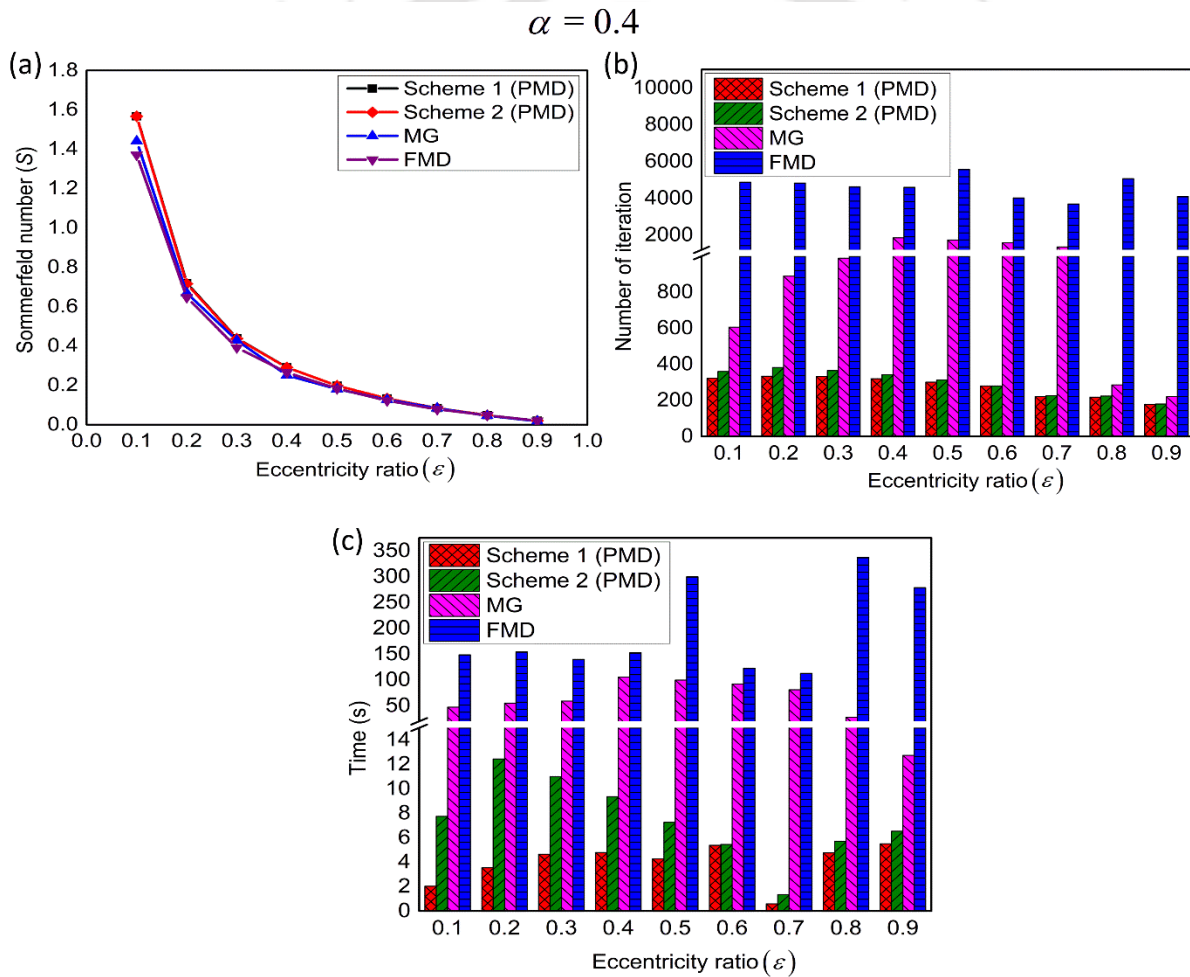


**Fig. 4.1** Computational efficiency comparison for PMD, MG and FMD methods for texture portion of 0.4: (a) the Sommerfeld number, (b) the number of iteration, and (c) the time, versus the eccentricity ratio

Figure 4.2(a) shows the Sommerfeld number results comparison obtained from Scheme 1 and Scheme 2 of PMD method, MG method and FMD method for texture portion of 0.8. It shows that the Sommerfeld number results predicted by Scheme 1 and Scheme 2 are very close to each other for the eccentricity ratios up to 0.5, whereas, for the other eccentricity ratios, both the schemes predicted the same results. The Sommerfeld number results predicted by the MG method have a slight difference from that of Scheme 1, Scheme 2 and the FMD method at all eccentricity ratios. The FMD method predicted results for Sommerfeld number also have a slight difference with that of Scheme 1 and Scheme 2 of PMD method at most of the eccentricity ratios. Figures 4.2(b) and 4.2(c) depicts the computational efficiency, in terms of the number of iterations and computing time, of Scheme 1, Scheme 2, MG method and FMD

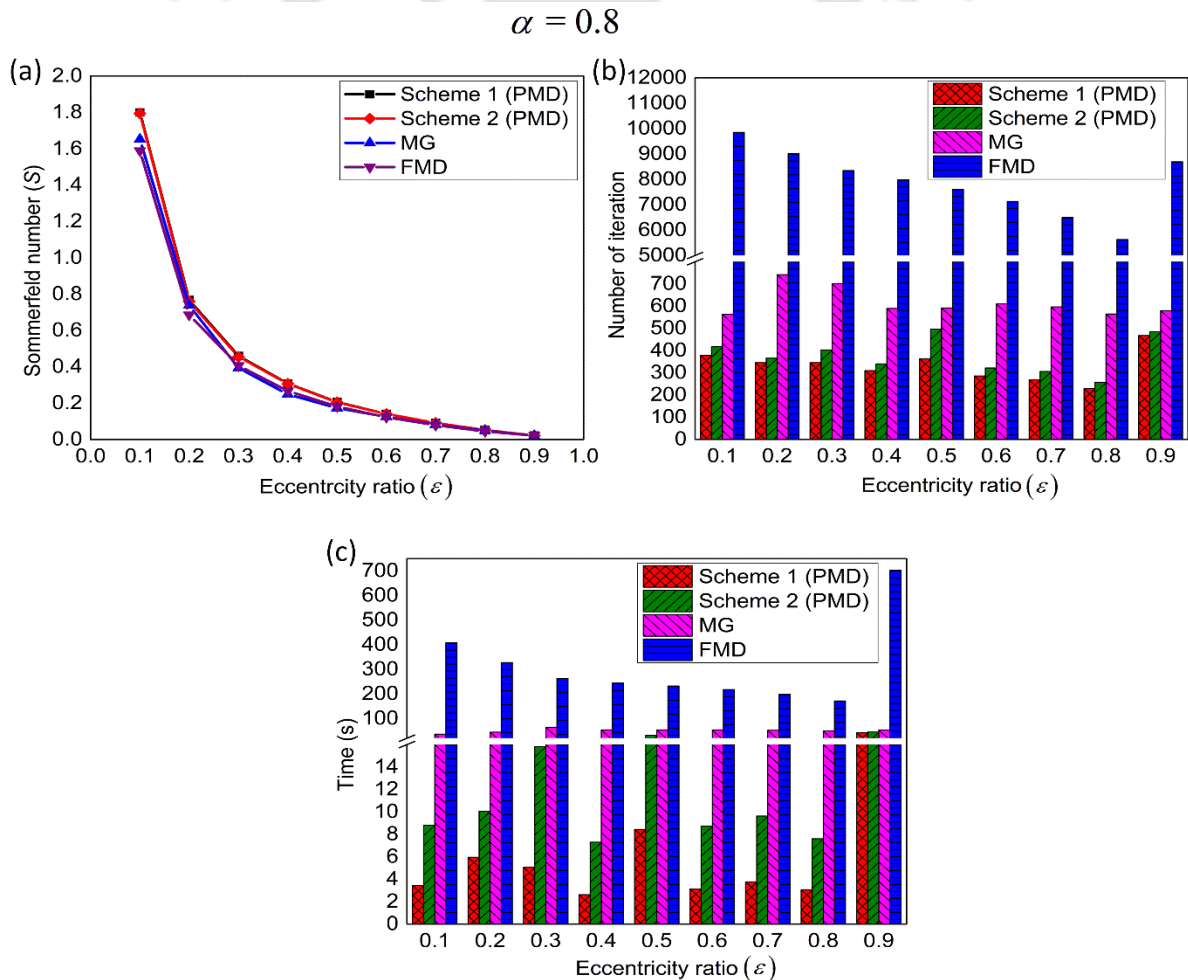


**Figure 4.2** Computational efficiency comparison for PMD, MG and FMD methods for texture portion of 0.8: (a) the Sommerfeld number, (b) the number of iteration, and (c) the time, versus the eccentricity ratio

method for texture portion of 0.8. From Fig. 4.2(b), it can be observed that the number of iterations taken by Scheme 1 to obtain the converged solution is lesser compared to Scheme 2. However, it is greatly lesser and moderately lesser compared to the FMD and MG methods, respectively. Here, the number of iterations taken by the MG and FMD methods is greater than 1.23 and 18.57 times that of Scheme 1, respectively. Figure 4.2(c) depicts that the computational time of Scheme 1 is lesser compared to Scheme 2, moderately lesser compared to the MG method and tremendously lesser compared to the FMD method. The Scheme 1 computing speed is at least 1.25 and 16.41 compared to the MG and FMD methods, respectively.

#### 4.1.2 Influence of dimple area density

The dimple area density is varied keeping other parameters constant such as texture portion ( $\alpha$ ) = 1.0, dimple aspect ratio ( $\psi$ ) = 0.06, non-dimensional clearance ( $\delta$ ) = 0.05 and non-dimensional length ( $\bar{L}$ ) = 20. The influence of dimple area density on the computational efficiencies of PMD, MG and FMD methods has been investigated for two cases of dimple area density ( $S_p$ ) of 0.05 and 0.10, as shown in Fig. 4.3 and Fig. 4.4, respectively.

The comparison of Sommerfeld number results, obtained from Scheme 1 and Scheme 2 of PMD method, MG method and FMD method, for dimple area density of 0.05, is shown in Fig. 4.3(a). It depicts that the Sommerfeld number results predicted by Scheme 1 and Scheme 2 of PMD are the same for all eccentricity ratios except for 0.1 and 0.9, with a negligible difference. The Sommerfeld number results of the MG method have a slight difference with the results of Scheme 1 and Scheme 2 at all eccentricity ratios, whereas, with respect to the FMD method, the difference is negligible at most of the eccentricity ratios. The Sommerfeld number results predicted by the FMD method also have a slight difference from that of Scheme 1 and Scheme 2 of the PMD method at most of the eccentricity ratios. Figure 4.3(b) depicts the comparison of computational efficiency, in terms of the number of iterations, of Scheme 1, Scheme 2, MG method and FMD method for dimple area density of 0.05. From Fig. 4.3(b), it is evident that the number of iterations of Scheme 1 is lesser compared to Scheme 2, whereas compared to the MG method and FMD method moderately lesser and tremendously lesser, respectively. The number of iterations taken for convergence by the MG method and

FMD method is more than 1.15 and 10.41 times that of Scheme 1, respectively. Figure 4.3(c) presents the comparison of the computational efficiency of Scheme 1, Scheme 2, MG method and FMD method, for dimple area density of 0.05, in terms of computational time. It is observed from Fig. 4.3(c) that Scheme 1 has better computational efficiency in terms of computational time compared to Scheme 2. Also, Scheme 1 has lesser computational time compared to Scheme 2, moderately lesser computational time compared to the MG method and greatly lesser computational time compared to the FMD method. The computing speed of Scheme 1 is greater than 1.86 and 20.48 compared to the MG and FMD methods, respectively.

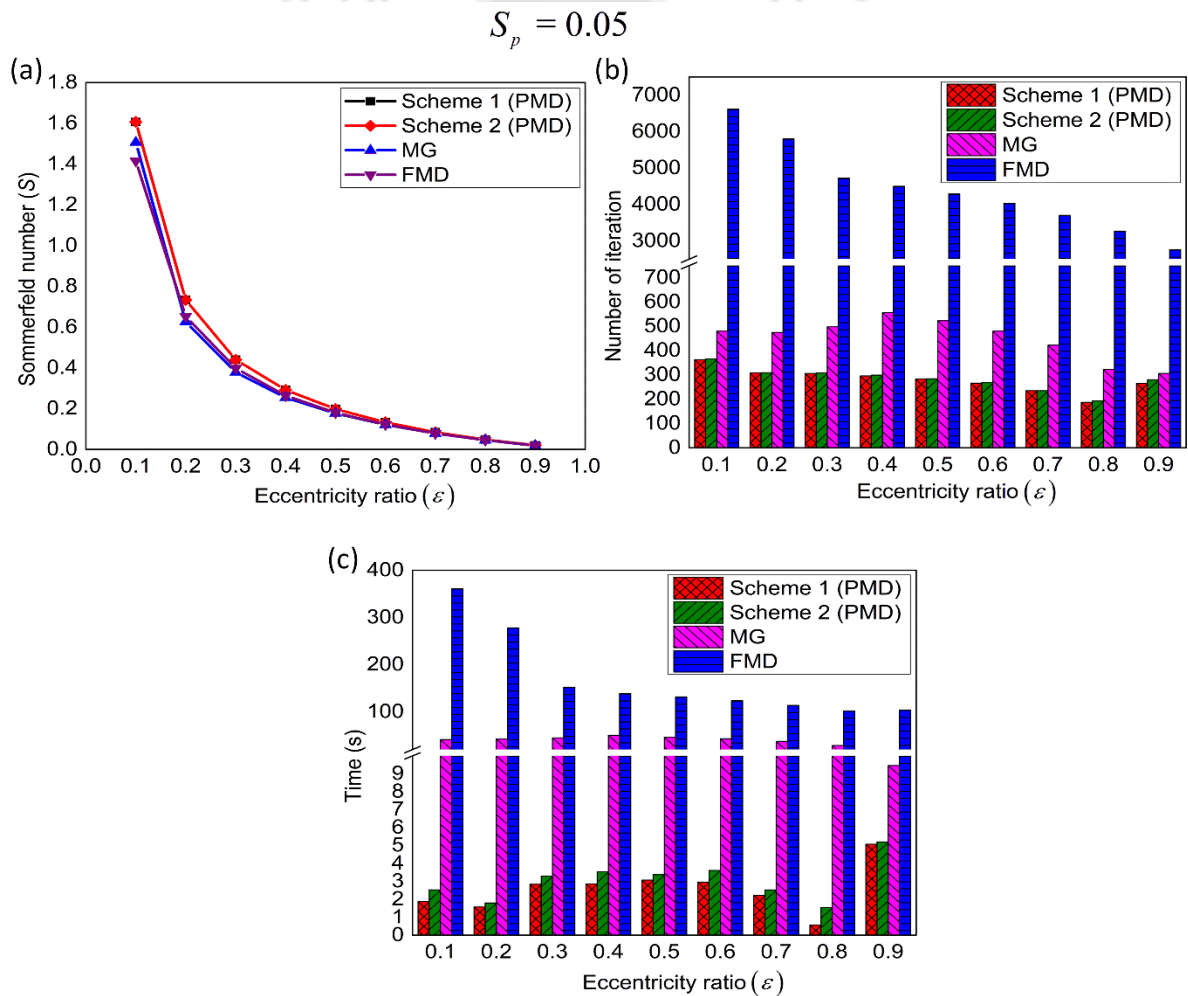


**Fig. 4.3** Computational efficiency comparison for PMD, MG and FMD methods for dimple area density of 0.05: (a) the Sommerfeld number, (b) the number of iteration, and (c) the time, versus the eccentricity ratio

Figure 4.4(a) illustrates the comparison of Sommerfeld number results estimated from Scheme 1, Scheme 2, MG method and FMD method for dimple area density of 0.10. From Fig. 4.4(a), it is evident that the Sommerfeld number results for Scheme 1 and Scheme 2 have a negligible difference at eccentricity ratios from 0.1 to 0.5 and no difference at the other eccentricity ratios. The Sommerfeld number results of Scheme 1 and Scheme 2 have a slight difference from that of the MG method and FMD method. The Sommerfeld number results estimated by the MG method also have a slight difference from that of the FMD method at most of the eccentricity ratios. Figures 4.4(b) and 4.4(c) presents the comparison of the computational efficiency of Scheme 1 and Scheme 2 of the PMD method, MG method and FMD method for dimple area density of 0.10 in terms of the number of iterations and computational time, respectively. It is evident from Fig. 4.4(b) that the number of iterations for Scheme 1 is lesser compared to Scheme 2 and the MG method and greatly lesser compared to the FMD method. It is also observed from Fig. 4.4(c) that Scheme 1 has lesser computational time compared to Scheme 2, moderately lesser computational time compared to the MG method and tremendously lesser computational time compared to FMD method. The number of iterations taken by the MG method and FMD method is greater than 1.13 and 10.74 times that of Scheme 1, respectively. The percentage reduction in computational time for Scheme 1 compared to MG and FMD methods is above 58 and 91, respectively.

### 4.1.3 Influence of dimple aspect ratio

Here, the computational efficiencies result for two cases of dimple aspect ratio ( $\psi$ ) of 0.04 and 0.08 are shown in Fig. 4.5 and Fig. 4.10, respectively. The other parameters that considered constant are texture portion ( $\alpha$ ) = 1.0, dimple area density ( $S_p$ ) = 0.13, non-dimensional clearance ( $\delta$ ) = 0.05 and non-dimensional length ( $\bar{L}$ ) = 20. The more detailed results are illustrated in figures 4.6 through 4.9, showing the variation of averaged Sommerfeld number and averaged non-dimensional pressure with the number of iterations at the dimple aspect ratio of 0.04 and eccentricity ratio of 0.8.

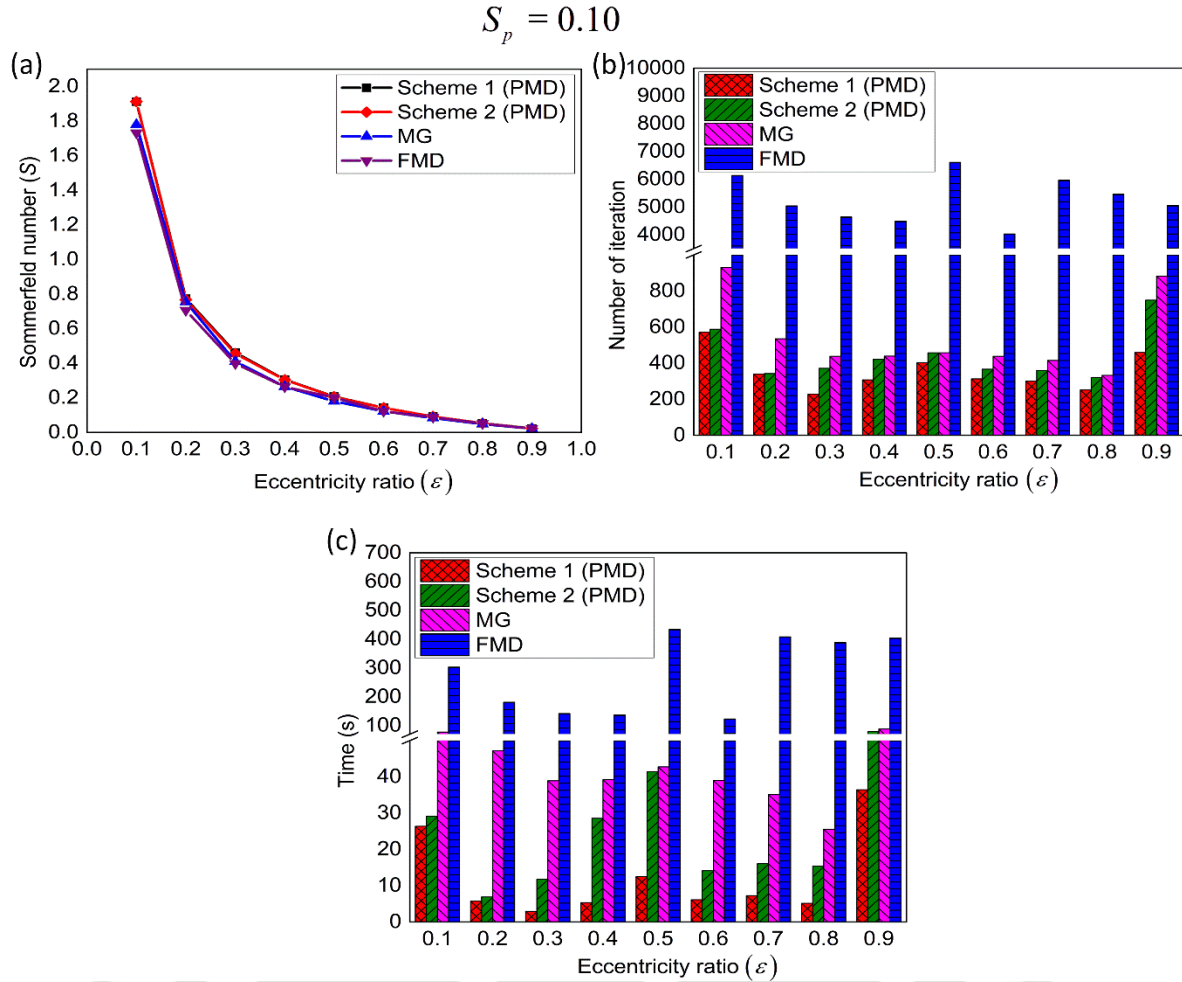


**Fig. 4.4** Computational efficiency comparison for PMD, MG and FMD methods for dimple area density of 0.10: (a) the Sommerfeld number, (b) the number of iteration, and (c) the time, versus the eccentricity ratio

Figure 4.5(a) depicts the comparison of the Sommerfeld number obtained from Scheme 1 and Scheme 2 of the PMD method, MG method and FMD method for a dimple aspect ratio of 0.04. It is observed that the Scheme 1 results of Sommerfeld number have negligible differences from that of Scheme 2 for eccentricity ratios from 0.1 to 0.5, and at other eccentricity ratios, both the schemes predicted the same results. The Sommerfeld number results of Scheme 1 and Scheme 2 have negligible difference from that of the MG method at most of the eccentricity ratios. Also, the Sommerfeld number results predicted by Scheme 1 and Scheme 2 have a slight difference from that of the FMD method. Figures 4.5(b) and 4.5(c) show the comparison of computational efficiency, for dimple aspect ratio of 0.04, of Scheme 1, Scheme 2, MG method and FMD method in terms of the number of iterations and

computational time, respectively. From Fig. 4.5(b), it is evident that Scheme 1 takes a lesser number of iterations to reach convergence compared to Scheme 2 and the MG method and tremendously lesser iterations compared to the FMD method. The percentage reduction in the number of iterations for Scheme 1 compared to MG and FMD methods is above 12 and 88, respectively. It is observed from Fig. 4.5(c) that the computational time of Scheme 1 is less compared to Scheme 2, MG method and FMD method. It is also noticed that Scheme 1 and Scheme 2 takes moderately less computational time compared to the MG method and very less computational time compared to the FMD method. The percentage reduction in computational time for Scheme 1 compared to MG and FMD methods is above 17 and 77, respectively.

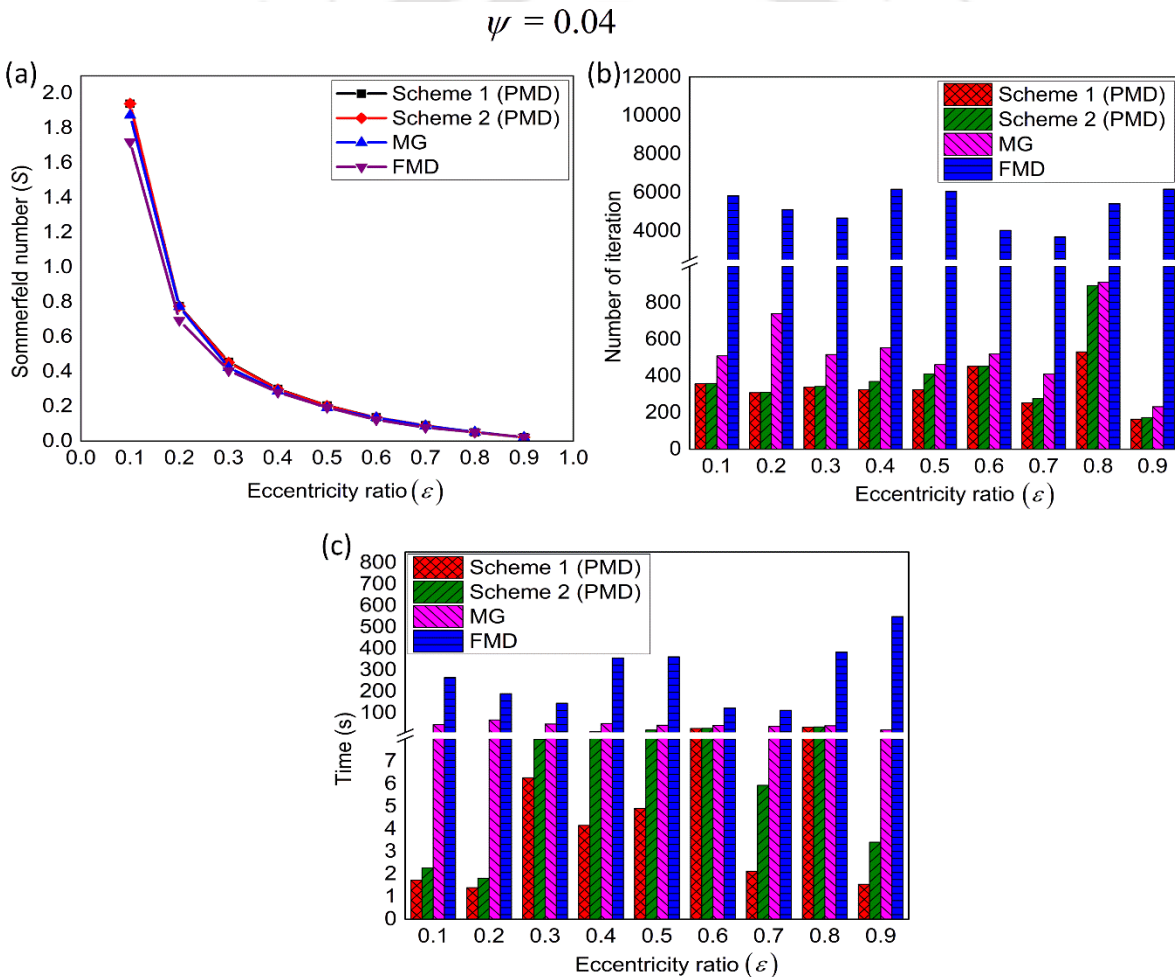


**Fig. 4.5** Computational efficiency comparison for PMD, MG and FMD methods for simple aspect ratio of 0.04: (a) the Sommerfeld number, (b) the number of iteration, and (c) the time, versus the eccentricity ratio

Figure 4.6 shows the averaged Sommerfeld number variation with the number of iterations for Scheme 1, MG method and FMD method at the dimple aspect ratio of 0.04 and an eccentricity ratio of 0.8. The averaged Sommerfeld number and the number of iterations, for Scheme 1, at the convergence are 0.05 and 532, respectively. Also, the Sommerfeld number value and the number of iterations for the MG method and the FMD method are 0.053, 912 and 0.051, 5426, respectively.

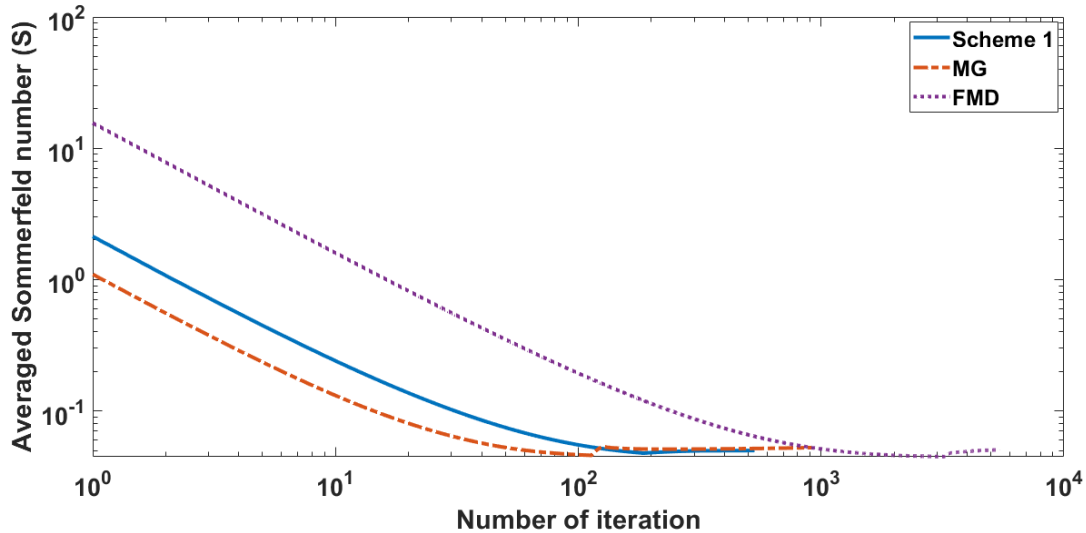


**Fig. 4.6** Comparison of Sommerfeld number results of Scheme 1, MG method and FMD method at the dimple aspect ratio of 0.04 and an eccentricity ratio of 0.8

The averaged non-dimensional pressure is also plotted against each iteration till convergence, for Scheme 1, MG method and FMD method, at the dimple aspect ratio of 0.04 and an eccentricity ratio of 0.8 as depicted in Fig. 4.7. Figure 4.7 shows that when the FMD method is selected the number of iterations taken for convergence is tremendously high that are 5426. The number of iterations taken by the MG method till convergence is 912. However, Scheme 1 of PMD takes only 532 iterations to reach a converged solution with the number of iterations on coarser mesh levels, i.e., level 1 and level 2 as 185 and 129, respectively and finer mesh level 3 as 218. The averaged non-dimensional pressure values obtained at the convergence for Scheme 1, MG method and FMD method are 779.40, 813.99 and 782.43, respectively.

The averaged Sommerfeld number variation with the number of iterations for Scheme 2, MG method and FMD method at the dimple aspect ratio of 0.04 and an eccentricity ratio of 0.8 is depicted in Fig. 4.8. It is observed from Fig. 4.8 that the averaged Sommerfeld number and the number of iterations, for Scheme 2, at the convergence are 0.05 and 894, respectively.

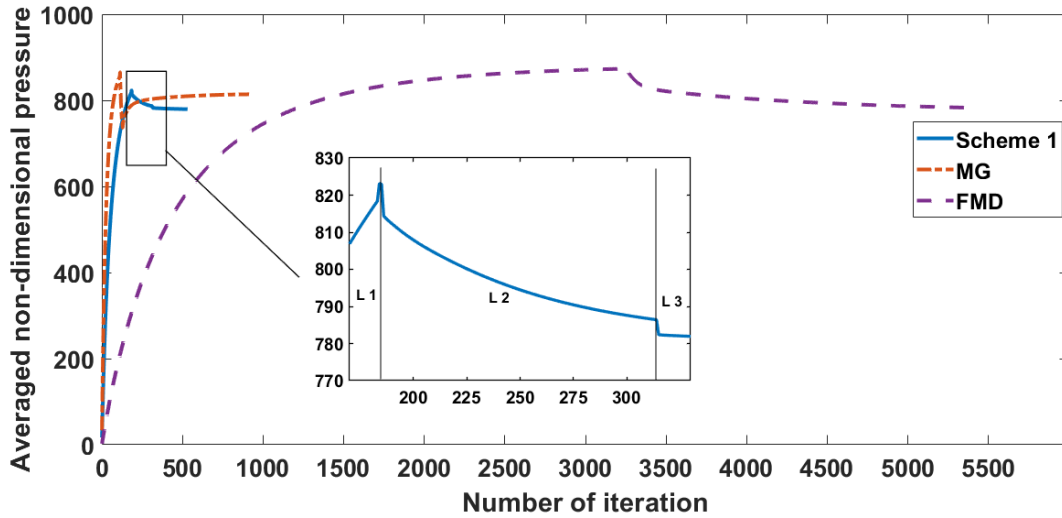


Fig. 4.7 Comparison of averaged pressure results of Scheme 1, MG method and FMD method at the dimple aspect ratio of 0.04 and an eccentricity ratio of 0.8

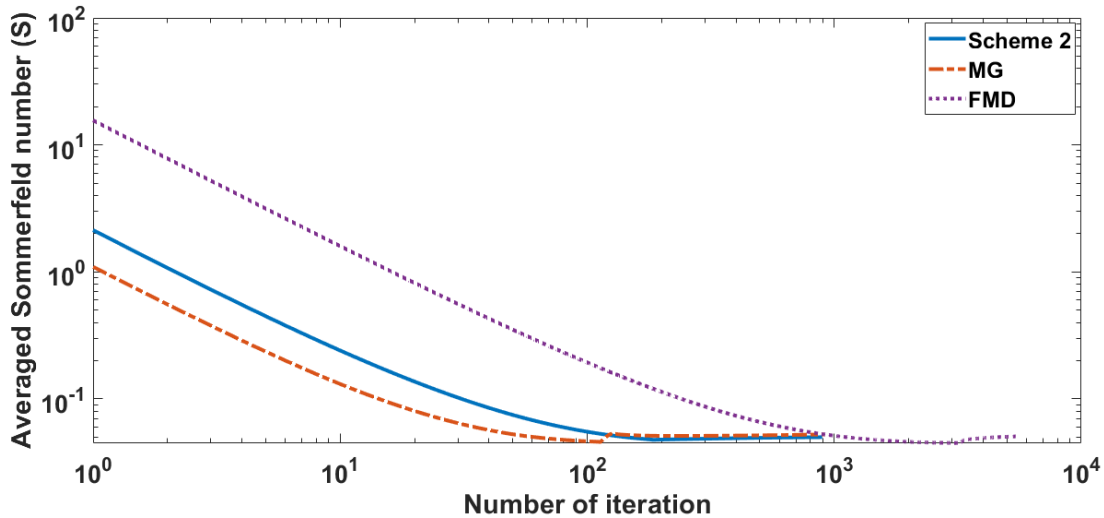
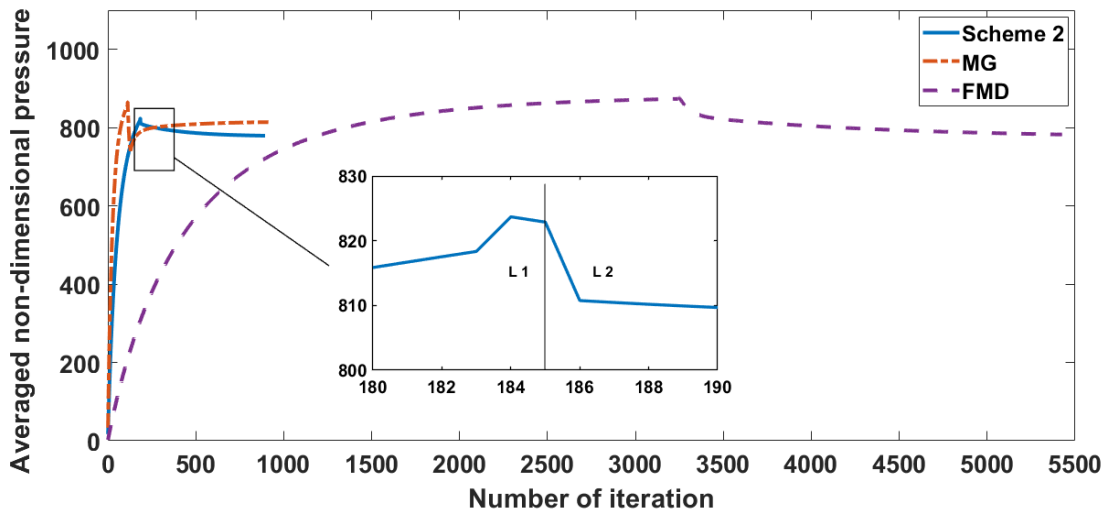


Fig. 4.8 Comparison of Sommerfeld number results of Scheme 2, MG method and FMD method at the dimple aspect ratio of 0.04 and an eccentricity ratio of 0.8

Figure 4.9 depicts the averaged non-dimensional pressure variation against number of iterations till convergence is obtained, for Scheme 2, MG method and FMD method, at the dimple aspect ratio of 0.04 and an eccentricity ratio of 0.8. It is observed that Scheme 2 takes 894 iterations to get the converged results. The number of iterations taken at level 1 and level 3 of Scheme 2 is 185 and 709, respectively. The averaged non-dimensional pressure value obtained at the convergence for Scheme 2 is 779.30.



**Fig. 4.9** Comparison of averaged pressure results of Scheme 2, MG method and FMD method at the dimple aspect ratio of 0.04 and an eccentricity ratio of 0.8

Figure 4.10(a) presents the Sommerfeld number results comparison obtained from Scheme 1 and Scheme 2 of the PMD method, MG method and FMD method for a dimple aspect ratio of 0.08. It shows that the Sommerfeld number results obtained from Scheme 1 and Scheme 2 are very close to each other for the eccentricity ratios up to 0.5, whereas, for the rest of the eccentricity ratios, both the schemes predicted the same results. The Sommerfeld number results obtained from the MG method have a slight difference from that of Scheme 1, Scheme 2 and the FMD method. The results for the Sommerfeld number predicted by the FMD method also have a slight difference from that of Scheme 1 and Scheme 2 of the PMD method at most of the eccentricity ratios. Figures 4.10(b) and 4.10(c) presents the computational performance, in terms of the number of iterations and computing time, of Scheme 1, Scheme 2, MG method and FMD method for a dimple aspect ratio of 0.08. From Fig. 4.10(b), it can be seen that the number of iterations taken by Scheme 1, to predict the converged solution is lesser compared

to Scheme 2 and the MG method. However, it is tremendously lesser compared to the FMD method. The number of iterations reduction percentage for Scheme 1 compared to the MG method and FMD method is 14 and 90, respectively. Figure 4.10(c) depicts that the computational time of Scheme 1 is lesser compared to Scheme 2, moderately lesser compared to the MG method and greatly lesser compared to the FMD method. The computational time reduction percentage for Scheme 1 compared to the MG method and FMD method is 17 and 80, respectively.

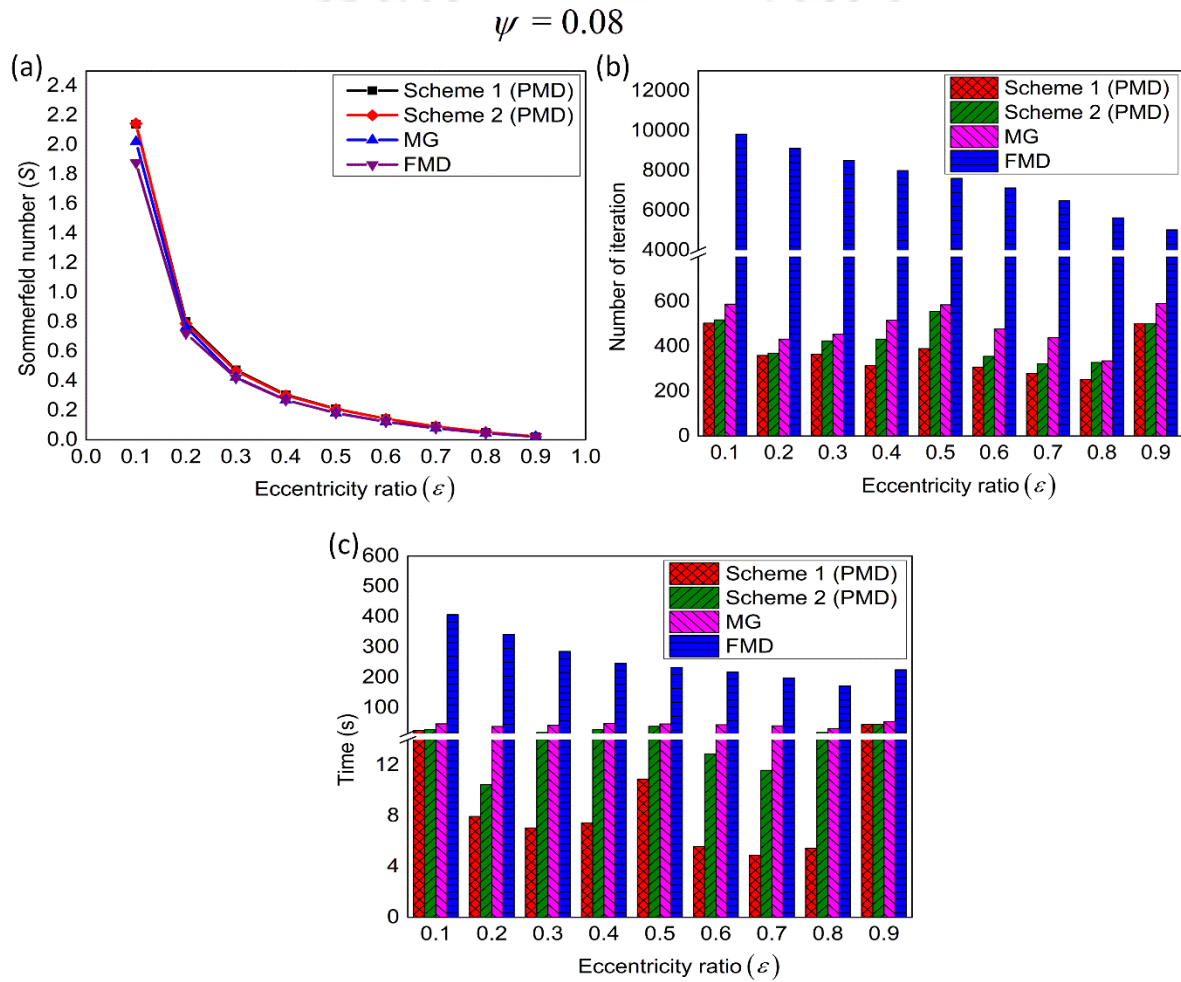


**Fig. 4.10** Computational efficiency comparison for PMD, MG and FMD methods for dimple aspect ratio of 0.08: (a) the Sommerfeld number, (b) the number of iteration, and (c) the time, versus the eccentricity ratio

#### **4.1.4 Influence of non-dimensional clearance**

The non-dimensional clearance ( $\delta$ ) is varied, keeping other parameters constant such as texture portion ( $\alpha$ ) = 1.0, dimple area density ( $S_p$ ) = 0.13, dimple aspect ratio ( $\psi$ ) = 0.06 and non-dimensional length ( $\bar{L}$ ) = 20 to study its effect on the computational efficiencies of PMD, MG and FMD methods for two different cases of 0.03 and 0.06 as shown in Fig. 4.11 and Fig. 4.12, respectively.

From Fig. 4.11(a), it is seen that the Scheme 1 predicted results for Sommerfeld number are very close to that of Scheme 2 and MG method and fairly close to the FMD method results. The results predicted by the MG method are over-estimated to the other methods with slight difference at the lower eccentricity ratios up to 0.5 and negligible difference at the other eccentricity ratios. The computational performance, in terms of the number of iterations and computing time, is presented in Fig. 4.11(b) and Fig. 4.11(c), respectively. It can be seen from figures 4.11(b) and 4.11(c) that the number of iterations and computational time taken by Scheme 1 is lesser compared to Scheme 2, moderately lesser compared to the MG method and greatly lesser compared to the FMD method. The number of iterations taken by Scheme 1 to obtain the converged solution is less than 86% and 19% that of the MG method and FMD method, respectively. Similarly, the computational time taken by Scheme 1 to reach the converged solution is less than 59% for the MG method and 35% for the FMD method.

It is depicted in Fig. 4.12(a) that the Scheme 1 predicted results for Sommerfeld number are very close to that of Scheme 2 for eccentricity ratios from 0.2 to 0.5 and the same as that of Scheme 2 for the rest of the eccentricity ratios. Also, the Sommerfeld number results of Scheme 1 are fairly close to the MG method and FMD method results. Figures 4.12(b) and 4.12(c) depicts the computational performance in terms of the number of iterations and computing time, respectively. From Fig. 4.12(b), it is shown that the number of iterations taken by Scheme 1 is lesser compared to Scheme 2, MG method and tremendously lesser compared to the FMD method. It is seen from Fig. 4.12(c) that the computing time taken by Scheme 1 to reach the converged solution is lesser compared to Scheme 2, moderately lesser compared to the MG method and greatly lesser compared to the FMD method. The number of iterations taken by Scheme 1 is less than 88% and 4% that of the MG and FMD methods, respectively.

Similarly, the computational time taken by Scheme 1 to reach the converged solution is less than 49% of MG method and 5% of FMD method.

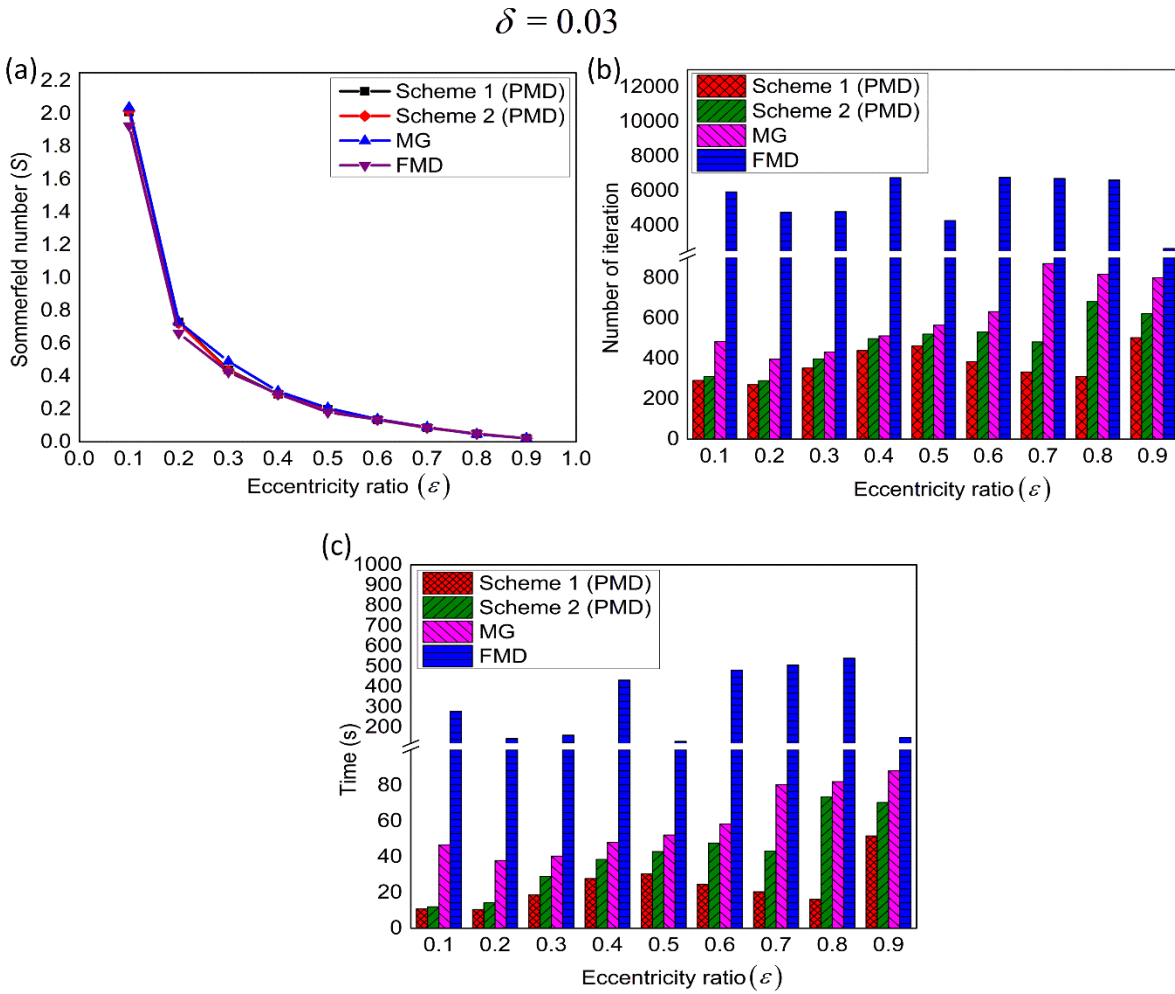


**Fig. 4.11** Computational efficiency comparison for PMD, MG and FMD methods for non-dimensional clearance of 0.03: (a) the Sommerfeld number, (b) the number of iteration, and (c) the time, versus the eccentricity ratio

#### 4.1.5 Influence of non-dimensional length

The effect of non-dimensional length on the computational efficiencies of PMD, MG and FMD methods is studied for two cases of non-dimensional length ( $\bar{L}$ ) of 30 and 50, as presented in Fig. 4.13 and Fig. 4.14, respectively. The other non-dimensional parameters considered constant are texture portion ( $\alpha$ ) = 1.0, dimple aspect ratio ( $\psi$ ) = 0.06, dimple area density ( $S_p$ ) = 0.13, non-dimensional clearance ( $\delta$ ) = 0.05.

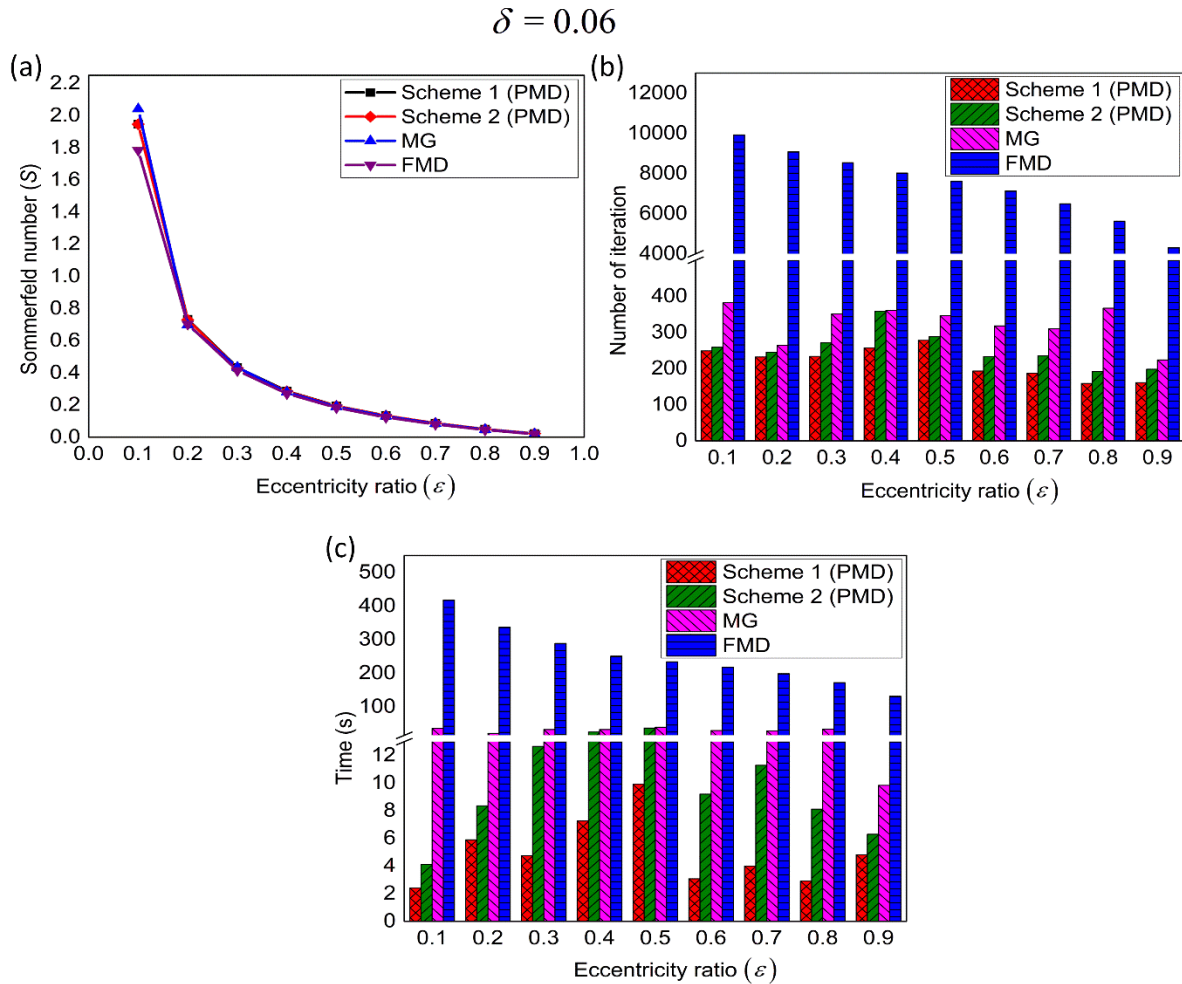


**Fig. 4.12** Computational efficiency comparison for PMD, MG and FMD methods for non-dimensional clearance of 0.06: (a) the Sommerfeld number, (b) the number of iteration, and (c) the time, versus the eccentricity ratio

Figure 4.13(a) shows that the Sommerfeld number results for Scheme 1, Scheme 2, MG method and FMD method are very close at the eccentricity ratios up to 0.5, and at the other eccentricity ratios, the difference is negligible. From Fig. 4.13(b), it is seen that the number of iterations taken by Scheme 1 to reach the converged solution is lesser, moderately lesser and much lesser compared to the Scheme 2, MG method and FMD method, respectively. Similarly, the computational time taken by Scheme 1 is lesser, moderately lesser and much lesser compared to Scheme 2, MG method and FMD method, respectively, as depicted in Fig. 4.13(c). The number of iterations to reach the converged solution for the MG and FMD methods are greater than 1.57 and 22.26 times that of Scheme 1, respectively. The Computing

time to reach the converged solution for the MG and FMD methods is more than 1.62 and 7.08 times that of Scheme 1, respectively.

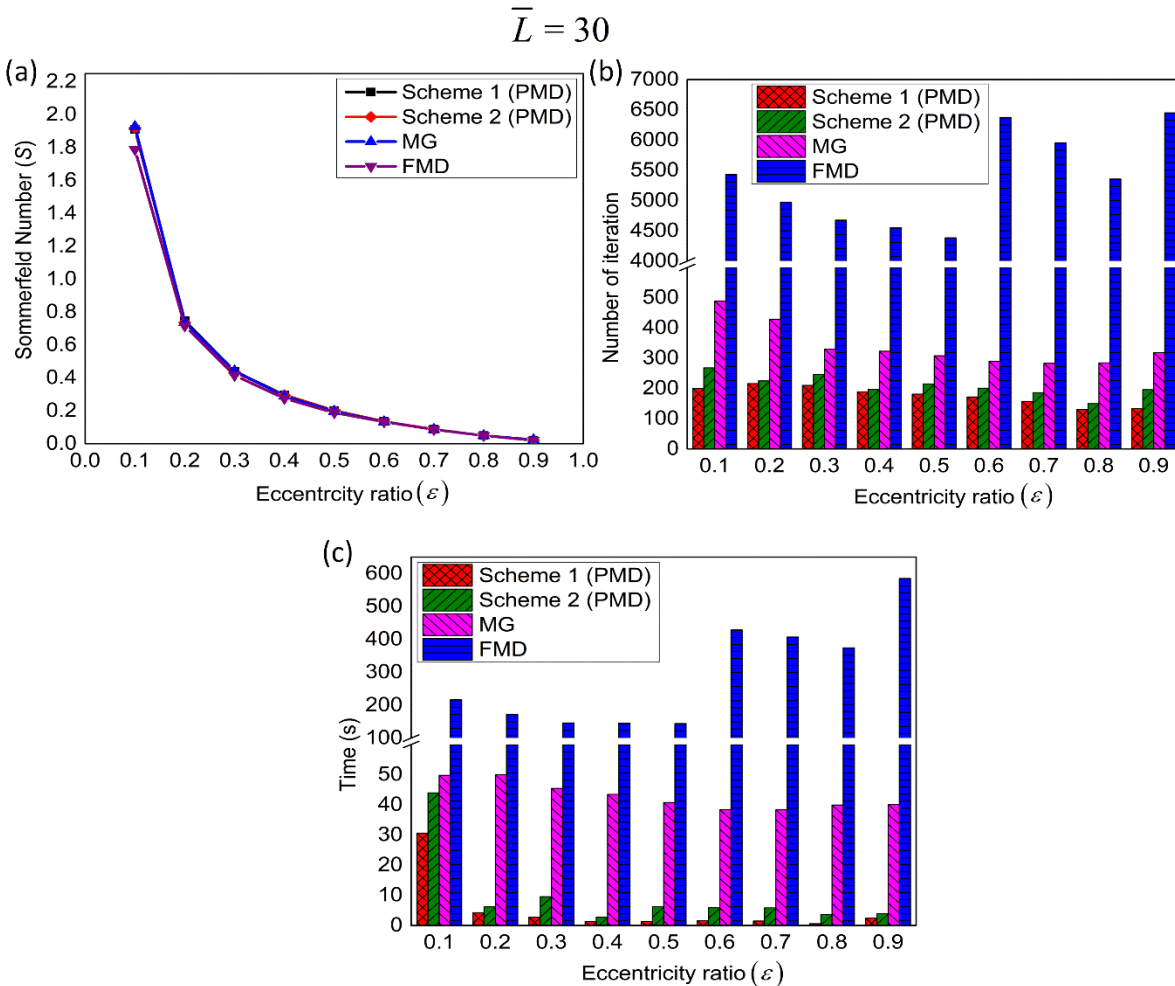


**Fig. 4.13** Computational efficiency comparison for PMD, MG and FMD methods for non-dimensional Length of 30: (a) the Sommerfeld number, (b) the number of iteration, and (c) the time, versus the eccentricity ratio

Figure 4.14(a) presents that the Sommerfeld number results for Scheme 1 have negligible difference from that of Scheme 2 and the MG method at most of the eccentricity ratios. However, the Sommerfeld number results predicted by the FMD method are very close to those predicted by Scheme 2, MG and FMD methods. It is observed from Fig. 4.14(b) that the number of iterations taken by Scheme 1 to attain the converged solution is lesser, moderately lesser and much lesser compared to the Scheme 2, MG method and FMD method, respectively. It is depicted in Fig. 4.14(c) that the computational time taken by Scheme 1 to reach convergence is lesser, moderately lesser and much lesser compared to the Scheme 2, MG

method and FMD method, respectively. The number of iterations to attain the convergence for the MG method and FMD method are more than 1.27 and 14.77 times that of Scheme 1, respectively. The Computing time to attain the convergence for the MG method and FMD method is more than 2.72 and 9.44 times that of Scheme 1, respectively.

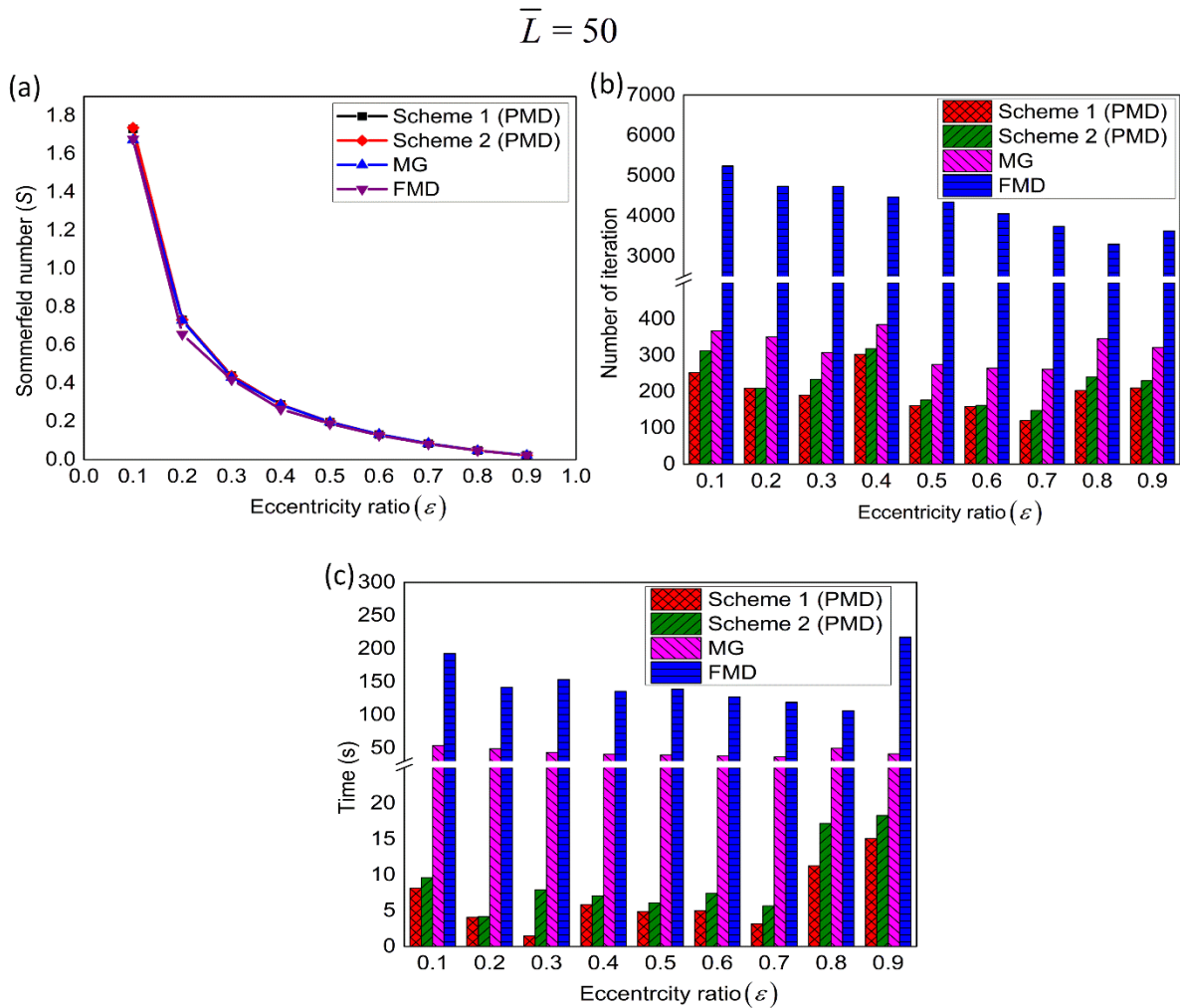


**Fig. 4.14** Computational efficiency comparison for PMD, MG and FMD methods for non-dimensional Length of 50: (a) the Sommerfeld number, (b) the number of iteration, and (c) the time, versus the eccentricity ratio

Scheme 1 is the computationally efficient method compared to Scheme 2, MG and FMD methods in all the above cases of variation of texture parameters. The computational efficiency of Scheme 1 compared to the MG and FMD methods, for all cases of texture parameters variation, is presented in Table 4.2. It is presented as the percentage of number of

iterations and computing time taken by Scheme 1 with respect to that of the MG and FMD methods. On overall, from all the cases of texture parameter variation as shown in Table 4.2, it can be observed that the number of iterations taken by Scheme 1 to obtain the converged solution is less than 88% and 19% that of the MG and FMD methods, respectively. Also, the computing time taken by Scheme 1 is less than 83% and 35% that of the MG and FMD methods, respectively.

**Table 4.2** Percentage of number of iterations and computing time taken by Scheme 1 with respect to the MG and FMD methods

Texture parameters		No. of iterations (%)		Computing time (%)	
		Scheme 1 w.r.to MG	Scheme 1 w.r.to FMD	Scheme 1 w.r.to MG	Scheme 1 w.r.to FMD
$\alpha$	0.4	80.91	7.17	43.25	4.37
	0.8	80.69	5.38	79.74	6.09
$S_p$	0.05	86.60	9.60	53.59	4.88
	0.10	87.77	9.30	41.56	9.02
$\psi$	0.04	87.12	11.25	82.39	22.64
	0.08	85.54	9.94	83.00	19.99
$\delta$	0.03	85.74	18.89	58.69	34.47
	0.06	87.88	3.74	48.98	4.24
$\bar{L}$	30	63.64	4.49	61.48	14.12
	50	78.70	6.77	36.65	10.59

## 4.2 Summary

In this chapter, the comparison of computational efficiencies, in terms of number of iterations and computing time, of PMD, MG and FMD methods has been done by varying texture and bearing parameters, for dimple textured journal bearing of  $L/D = 1$ , such as texture portion, dimple area density, dimple aspect ratio, non-dimension clearance and non-dimensional length. It is observed that the PMD method is the computationally efficient one compared to the MG and FMD methods, irrespective of any texture parameter value considered.

# Chapter 5

## Dimple and protruded textured journal bearing

---

### 5.0 Introduction

The spherical protruded and dimple textured journal bearing's performance characteristics in terms of load carrying capacity, friction variable and flow coefficient are compared with the untextured bearing for different texture configurations such as full textured region, first-half textured region and second-half textured region for  $L/D$  ratio of unity. Here, two different ways of comparison are presented. One comparison is based on eccentricity ratio and the other comparison is based on load. The governing Reynolds equation considering the mass conserving (JFO) boundary conditions is solved using the computationally efficient progressive mesh densification (PMD) method. The theory pertaining to Sec. 2.2 is applicable to this study. The numerical code developed is validated with the experimental results available in the literature.

### 5.1 Comparison of performance characteristics

#### 5.1.1 Comparison of present results for friction coefficient with the experimental results

The friction coefficient results obtained using the PMD method (with three levels) for one sectorial segment (simplified to parallel slider) of textured parallel thrust bearing are compared with the experimental results of Etsion et al. [16] for varying load at a speed of 1500 rpm, as illustrated in Fig. 5.1. The comparison is made for unidirectional texturing ( $L/B = 0.75$ ,  $S_p = 0.6$  and  $\alpha = 0.734$ ) and bidirectional texturing ( $L/B = 0.75$ ,  $S_p = 0.614$  and  $\alpha = 0.633$ ). In Fig. 5.1, it is seen that the theoretical model for unidirectional texturing predicted higher coefficient of friction values for loads under 320 N and lower coefficient of friction values for loads above 300 N compared to experimental results. Similarly, the theoretical model for bidirectional

texturing has predicted higher coefficient of friction values for loads below 250 N and lower values beyond 250 N compared to experimental results. The percentage difference between the theoretical and experimental results of both unidirectional and bidirectional texturing is less than 10%. However, at the load of 160 N, the difference in the theoretical and experimental results of unidirectional texturing is 13%. As the trends of the present results for friction coefficient are similar to that of the experimental results and the present result values for friction coefficient are also fairly close to those of experimental results. Therefore, the codes developed are used for the analysis of textured bearings. The input parameters used for the validation are presented in Table 5.1.

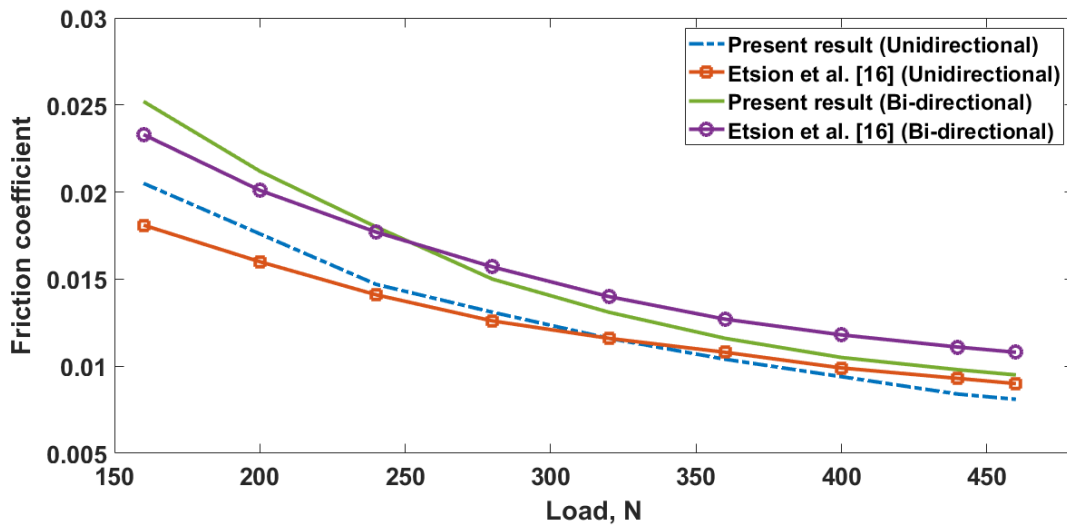


**Fig. 5.1** Validation of the present results with the experimental results of Etsion et al. [16]

As the experimental results for spherical textured journal bearing in the literature are limited and difficult to compare numerically, the experimental results for spherical textured thrust bearing of Etsion et al. [16] are used for validation. After validating the developed code for spherical textured thrust bearing with the experimental results of Etsion et al. [16], it has been modified for the spherical textured journal bearing.

### 5.1.2 Comparison based on eccentricity ratio

The parameters for journal bearing with spherical dimple and protruded texture considered in the present analysis are presented in Table 5.2. The protruded and dimple textured journal bearing performance characteristics such as load carrying capacity, friction variable and flow

coefficient in non-dimensional form are estimated for different non-dimensional texture depth/height (i.e., ratio of texture depth/height to the clearance) with various eccentricity ratios. The eccentricity ratios considered here are 0.2, 0.4, 0.6 and 0.8. The different textured region configurations of full texturing and partial texturing that have been considered in this study are full textured region ( $0^{\circ} - 360^{\circ}$ ), first-half textured region ( $0^{\circ} - 180^{\circ}$ ) and second-half textured region ( $180^{\circ} - 360^{\circ}$ ). The 3-level situation of the PMD method is implemented with mesh sizes for level 1, level 2 and level 3 as 56x18, 112x36 and 224x72, respectively. The ultimate convergence criterion followed is  $10^{-5}$ . The comparison of bearing performance characteristics, in non-dimensional form, for dimple textured and protruded textured bearing with untextured bearing are presented in the following sub-sections. The texture depth in Fig. 5.2 through Fig. 5.10 represents height of the texture for protruded textured bearing and depth of the texture for dimple textured bearing.

**Table 5.1** Parameters used for validation

parameter	Value	Parameter	Value
$L/B$	0.75	Speed	1500 rpm
Slider width $B$	50 mm	Velocity $U$	4.9 m/s
Dimple base radius $r_p$	$30\ \mu\text{m}$	Bulk modulus $\beta$	2.1 GPa
Dimple depth $h_p$	$6.5\ \mu\text{m}$	Cavitation pressure $p_c$	0.9 bar
Viscosity $\eta$	0.001 Pa.s	Ambient pressure $p_a$	1 bar

#### **5.1.2.1 Full textured region configuration ( $0^{\circ} - 360^{\circ}$ )**

In the case of full textured region configuration, two rows of 6 textures in the circumferential direction of journal bearing are considered for spherical dimple and protruded textures. The comparison of bearing performance characteristics for dimple textured and protruded textured bearing with untextured bearing is depicted in Fig. 5.2 through Fig. 5.4.

From Figs. 5.2(a) to 5.2(d), it has been observed that there is an increment in load carrying capacity for protruded textured journal bearing, whereas there is a decrement in load carrying capacity for dimple textured journal bearing with an increment in the texture depth/height value compared to the untextured journal bearing or plain journal bearing. The

maximum percentage increment in the load carrying capacity of protruded textured journal bearing is obtained, at the eccentricity ratio of 0.8 and the texture height of 0.4, as 88.77% compared to dimple textured journal bearing and 75.12% compared to the untextured journal bearing.

**Table 5.2** Parameters for the numerical study of spherical textured journal bearing

Parameter	Value	Parameter	Value
Diameter $D$	62.8 mm	Bulk modulus $\beta$	$1 \times 10^8$ Pa
$L/D$ ratio	1	Cavitation pressure $p_c$	0.9 bar
Clearance $C$	0.055 mm	Ambient pressure $p_a$	1 bar
Viscosity $\eta$	0.0035 Pa. s	Dimple base radius $r_p$	10 mm
Velocity $U$	19.7 m/s	Dimple area density $S_p$	0.3

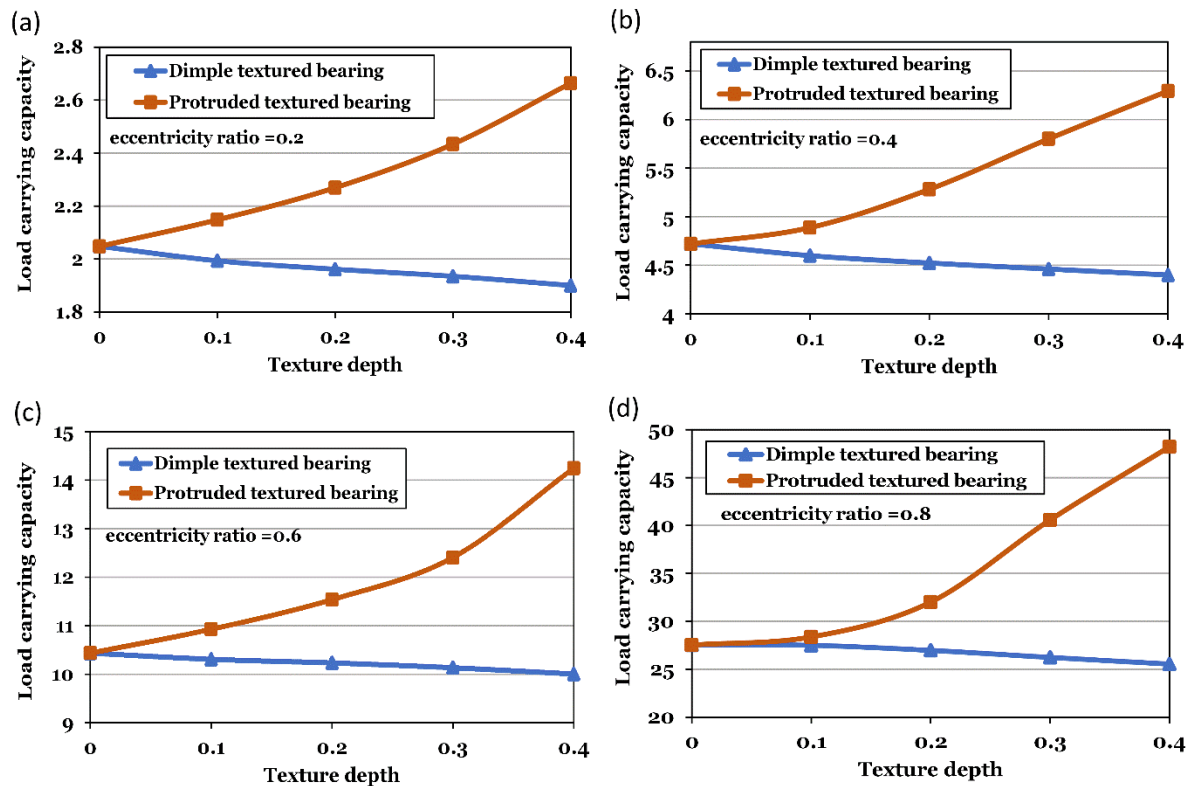


**Fig. 5.2** Comparison of load carrying capacity for journal bearing with dimple and protruded textures with untextured bearing by varying texture depth for full textured region configuration

In Figs. 5.3(a) to 5.3(d), it is shown that there is a decrement in friction variable for protruded textured journal bearing whereas an increment in friction variable for dimple textured journal bearing with an increment in the texture depth/height value when compared to the untextured journal bearing. The maximum percentage decrement in the friction variable of protruded textured journal bearing is obtained, at an eccentricity ratio of 0.8 and the texture height of 0.4, as 45.01% compared to dimple textured journal bearing and 41.33% when compared to the untextured journal bearing.

Therefore, corresponding to load carrying capacity and friction variable, bearing performance characteristics of full textured journal bearing with dimple textures have been negatively affected, whereas performance characteristics of full textured journal bearing with protruded textures have been significantly improved.

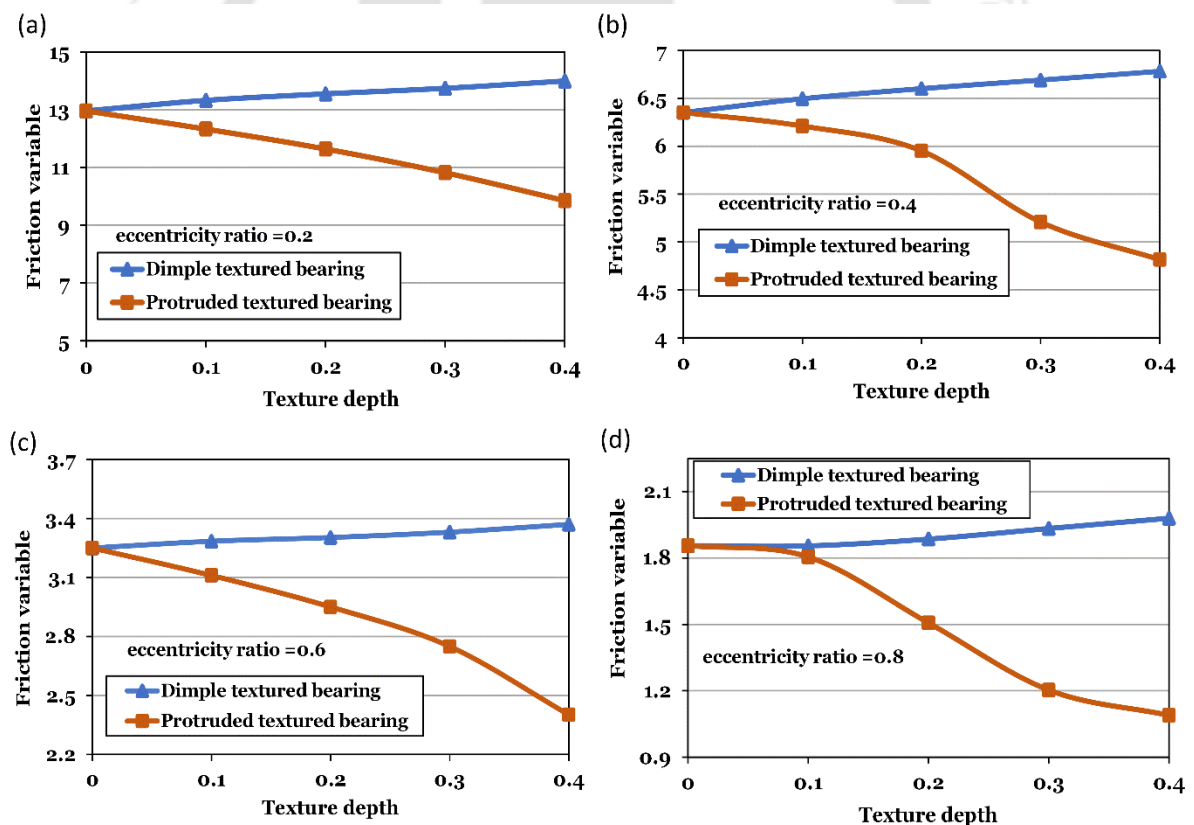


**Fig. 5.3** Comparison of friction variable for journal bearing with dimple and protruded textures with untextured bearing by varying texture depth for full textured region configuration

There is an increment in flow coefficient for dimple textured journal bearing and protruded textured journal bearing with an increment in the texture depth/height value compared to the untextured journal bearing, as shown in Figs. 5.4(a) to 5.4(d). The maximum percentage increment in the flow coefficient of protruded textured journal bearing is obtained, at the eccentricity ratio of 0.6 and the texture height of 0.4, as 4.8% compared to dimple textured journal bearing and 14.07% compared to the untextured journal bearing. Hence, in the case of flow coefficient, bearing performance characteristics of full textured journal bearing with dimple textures and full textured journal bearing with protruded textures have been positively affected.

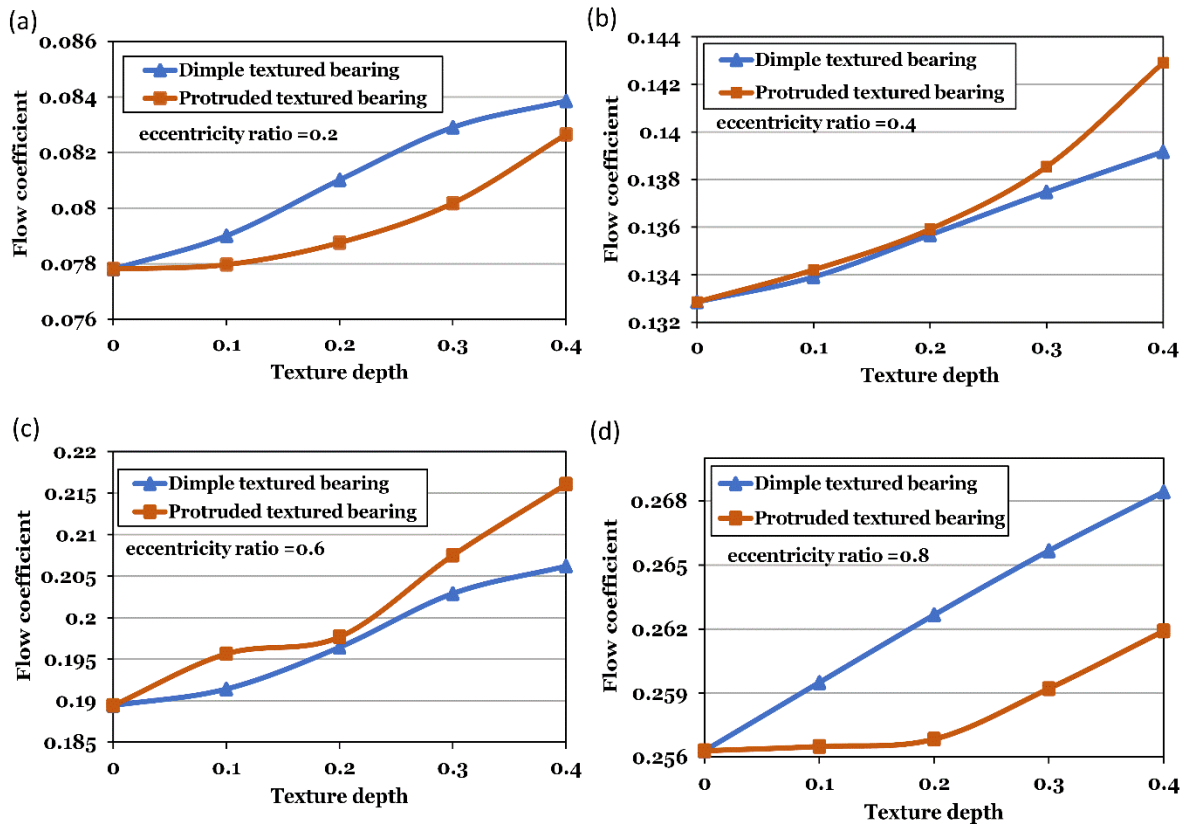


**Fig. 5.4** Comparison of flow coefficient for journal bearing with dimple and protruded textures with untextured bearing by varying texture depth for full textured region configuration

5.1.2.2 First half-textured region configuration (  $0^\circ - 180^\circ$  )

In the analysis of the first half-textured region configuration, two rows of the first three textures in the journal bearing circumferential direction are selected for spherical dimple and protruded textures. The comparison of bearing performance characteristics is shown in Fig. 5.5 through Fig. 5.7.

It has been found in Figs. 5.5(a) to 5.5(d) that the load carrying capacity is increased for protruded textured journal bearing, whereas it is decreased for dimple textured journal bearing with an increment in the texture depth/heights value when compared to untextured journal bearing. The maximum percentage increment in the load carrying capacity of journal bearing with protruded textures is obtained, at the eccentricity ratio of 0.2 and the texture height of 0.4, as 27.11% compared to journal bearing with dimple textures 24.26% compared to the plain journal bearing.

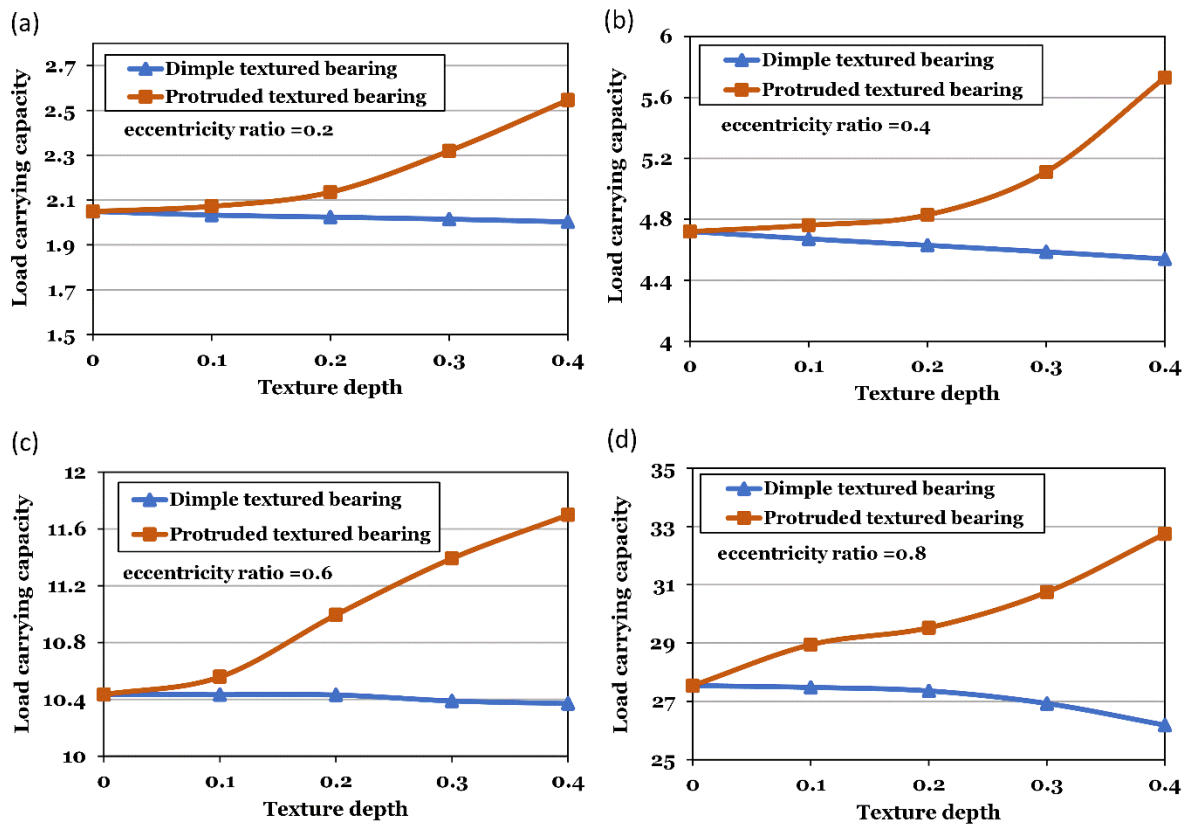
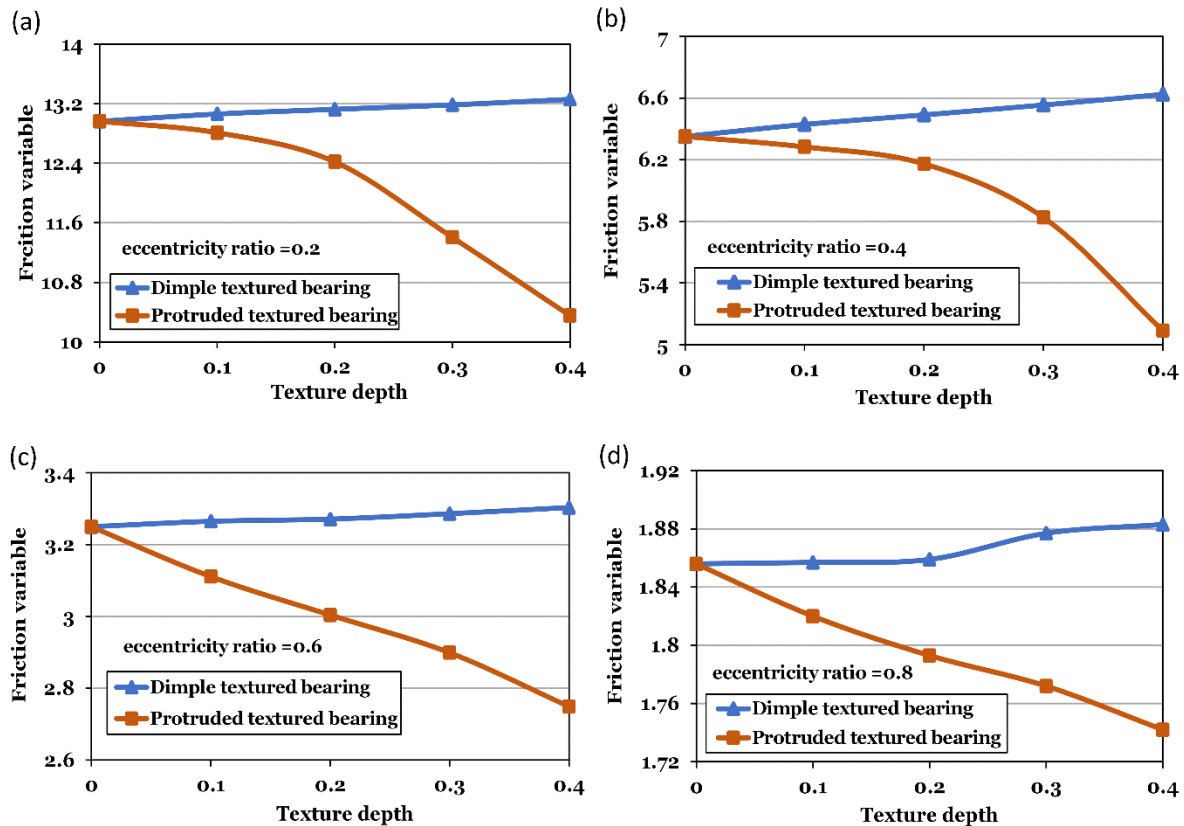


Fig. 5.5 Comparison of load carrying capacity for journal bearing with dimple and protruded textures with untextured bearing by varying texture depth for first-half textured region configuration

From Figs. 5.6(a) to 5.6(d), it has been observed that there is a decrement in friction variable for protruded textured journal bearing, whereas there is an increase in friction variable for dimple textured journal bearing with an increment in the texture depth/heights value when compared to the untextured journal bearing. The maximum percentage decrement in the friction variable of protruded textured journal bearing is obtained, at the eccentricity ratio of 0.4 and the texture height of 0.4, as 23.17% compared to dimple textured journal bearing whereas, it is found as 20.14%, at the eccentricity ratio of 0.2 and the texture height of 0.4, compared to the untextured journal bearing.

Hence, corresponding to load carrying capacity and friction variable, bearing performance characteristics of protruded textured journal bearing textured in the first-half of the circumferential region are positively affected. However, dimple textured journal bearing textured in first-half of the circumferential region gives deterioration in performance.



**Fig. 5.6** Comparison of friction variable for journal bearing with dimple and protruded textures with untextured bearing by varying texture depth for first-half textured region configuration

Figures 5.7(a) to 5.7(d) depict an increment in flow coefficient for dimple textured journal bearing and decrement in flow coefficient for protruded textured journal bearing with an increment in the texture depth/height value when compared to the untextured journal bearing. The maximum percentage increment in the flow coefficient of dimple textured journal bearing is obtained, at the eccentricity ratio of 0.2 and the texture height of 0.4, as 19.44% when compared to protruded textured journal bearing and 10.26% compared to the untextured journal bearing. Therefore, in terms of flow coefficient, bearing performance characteristics of protruded textured journal bearing textured in the first half of the circumferential region have been negatively affected, whereas bearing performance characteristics of dimple textured journal bearing textured in the first half of the circumferential region have been significantly improved.

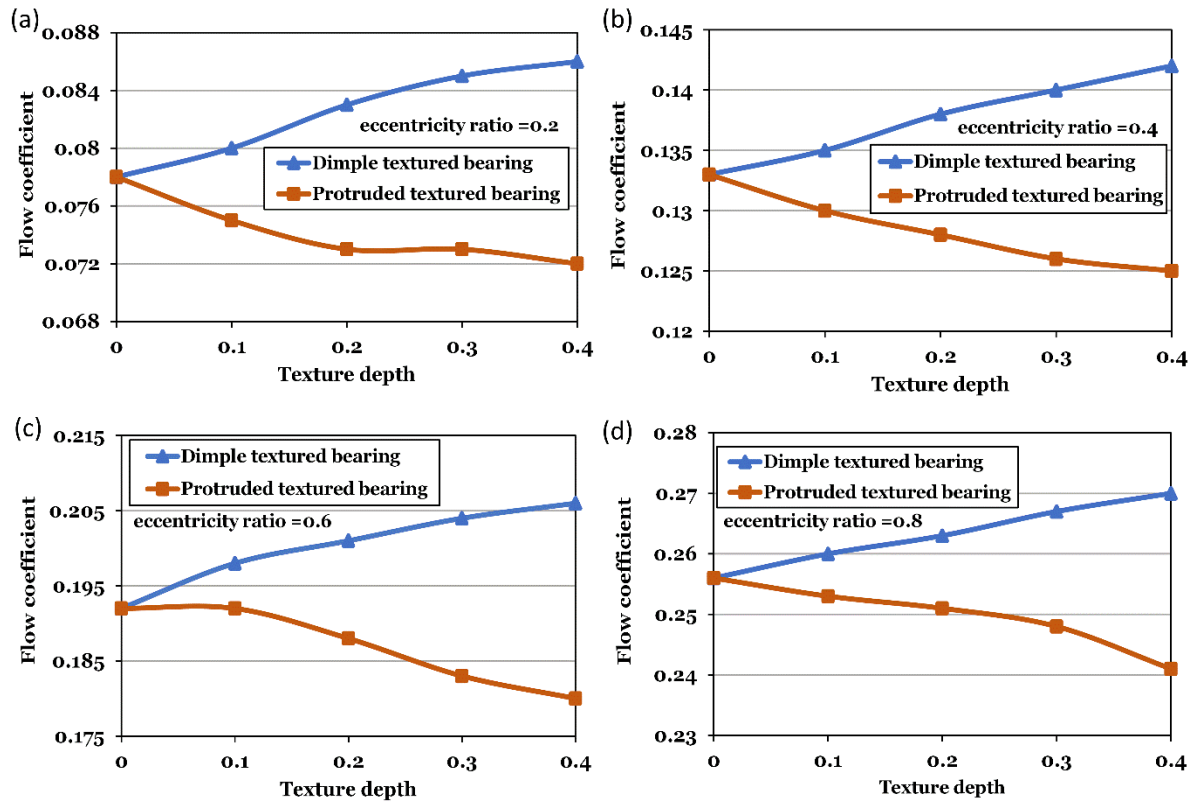


**Fig. 5.7** Comparison of flow coefficient for journal bearing with dimple and protruded textures with untextured bearing by varying texture depth for first-half textured region configuration

### 5.1.2.3 Second half-textured region configuration ( $180^{\circ} - 360^{\circ}$ )

In the present analysis of second half-textured region configuration, two rows of last 3 textures in circumferential direction of journal bearing are selected for spherical dimple and protruded textures. The bearing performance characteristics are depicted in Fig. 5.8 through Fig. 5.10.

From Figs. 5.8(a) to 5.8(d), it has been found that there is an increment in load carrying capacity for protruded textured journal bearing and a decrement in load carrying capacity for dimple textured journal bearing with an increment in the texture depth/heights value as compared to the untextured journal bearing. The maximum percentage increment in load carrying capacity of protruded textured journal bearing is obtained, at the eccentricity ratio of 0.8 and the texture height of 0.4, as 85.88% compared to dimple textured journal bearing and 83.16% compared to untextured journal bearing.

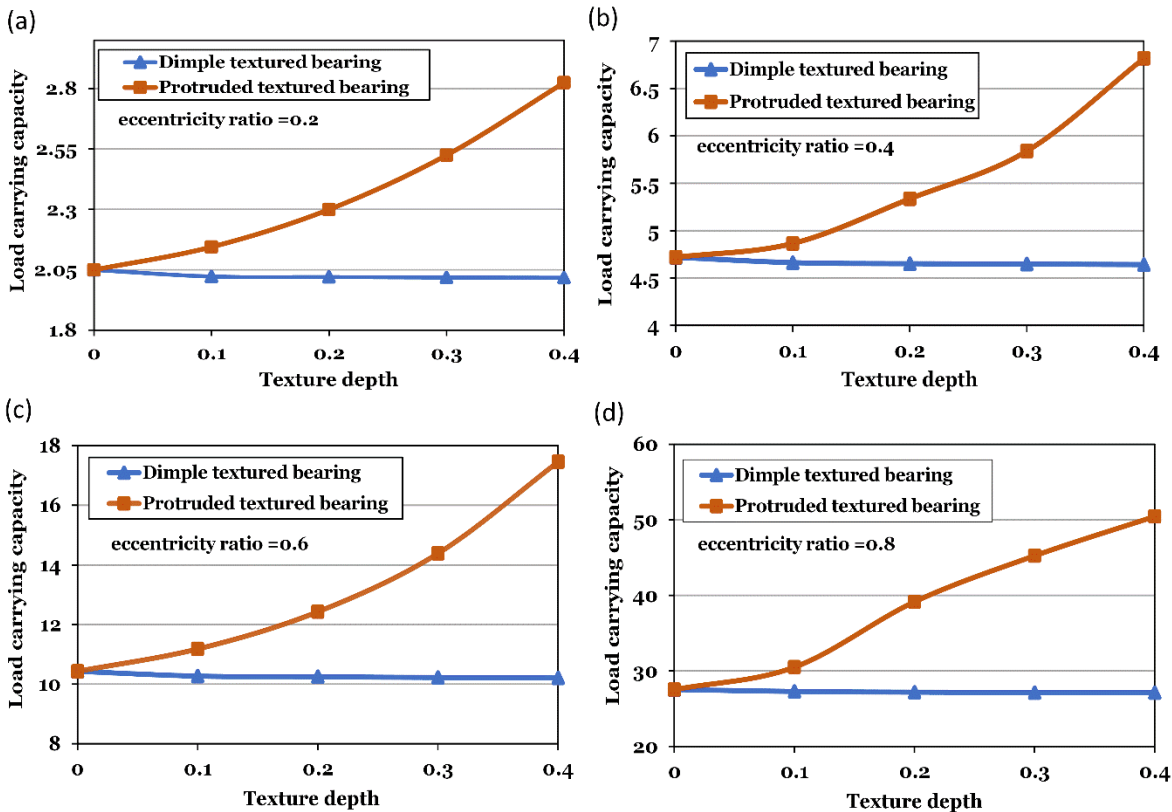


**Fig. 5.8** Comparison of load carrying capacity for journal bearing with dimple and protruded textures with untextured bearing by varying texture depth for second-half textured region configuration

It has been noticed from Figs. 5.9(a) to 5.9(d) that there is a decrease in friction variable for protruded textured journal bearing, whereas there is an increase in friction variable for dimple textured journal bearing with an increment in the texture depth/height value when compared to the untextured journal bearing. The maximum percentage reduction in the friction variable of protruded textured journal bearing is obtained, at the eccentricity ratio of 0.8 and the texture height of 0.4, as 45.22% compared to dimple textured journal bearing whereas, it is found as 44.40%, at the eccentricity ratio of 0.8 and the texture height of 0.4, compared to untextured journal bearing.

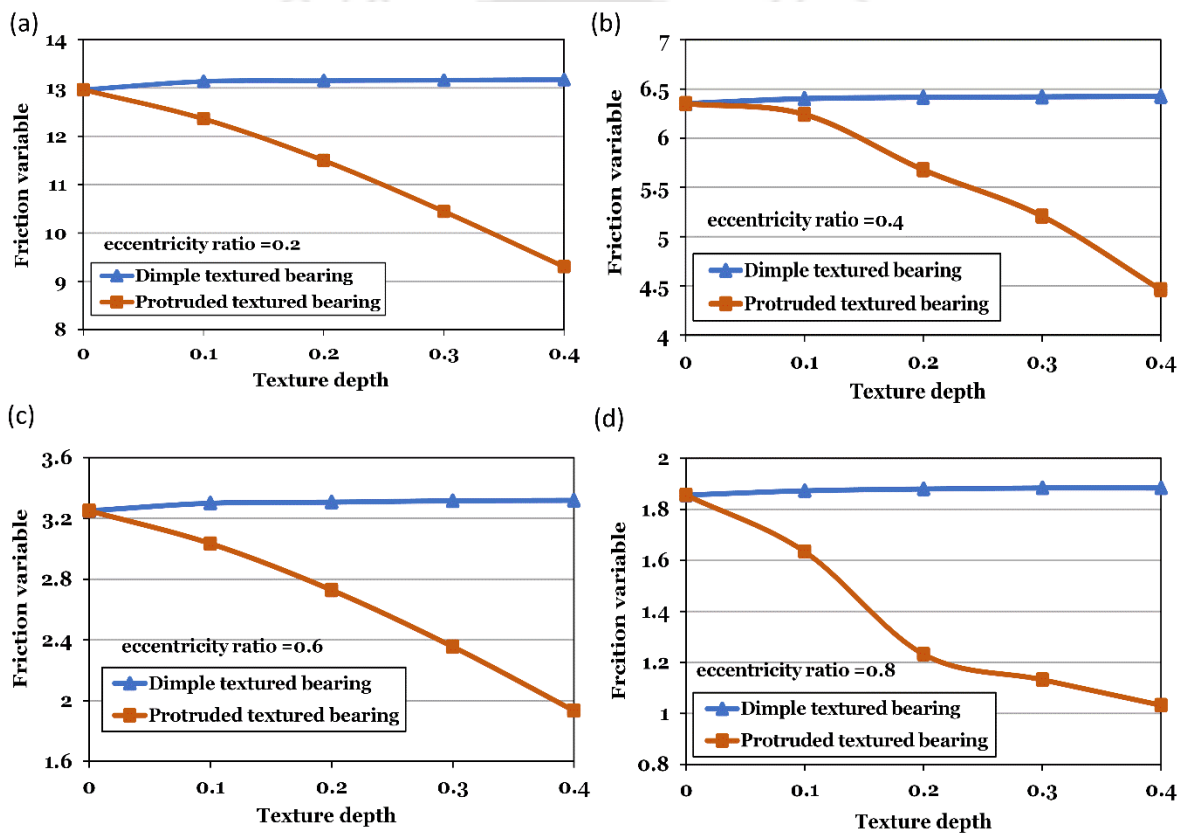


**Fig. 5.9** Comparison of friction variable for journal bearing with dimple and protruded textures with untextured bearing by varying texture depth for second-half textured region configuration

Therefore, in the case of load carrying capacity and friction variable, bearing performance characteristics of protruded textured journal bearing textured in second-half of the circumferential region are significantly improved whereas, bearing performance

characteristics of dimple textured journal bearing textured in second-half of the circumferential region have deteriorated.

It is depicted from Figs. 5.10(a) to 5.10(d) that there is an increment in flow coefficient for protruded textured journal bearing and reduction in flow coefficient for dimple textured journal bearing with an increment in the texture depth/height value when compared to the plain journal bearing. The maximum percentage increment in the flow coefficient of protruded textured journal bearing is noticed, at the eccentricity ratio of 0.2 and the texture height of 0.4, as 25.97% compared to dimple textured journal bearing and 24.36% compared to the plain journal bearing. Therefore, related to flow coefficient, bearing performance characteristics of protruded textured journal bearing textured in the second half of the circumferential region are significantly improved, whereas bearing performance characteristics of dimple textured journal bearing textured in the second half of the circumferential region are adversely affected.

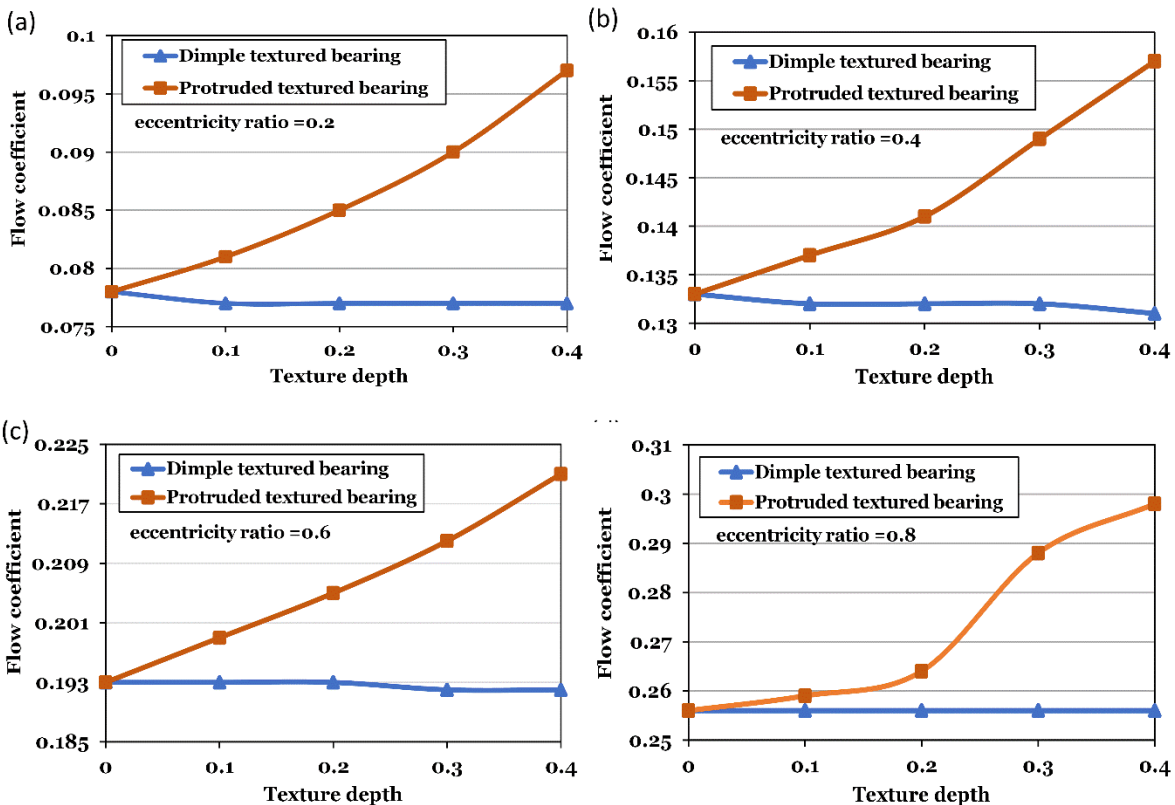


**Fig. 5.10** Comparison of flow coefficient for journal bearing with dimple and protruded textures with untextured bearing by varying texture depth for second-half textured region configuration

#### **5.1.2.4 Calculation of optimum design parameters**

The performance enhancement for journal bearing with spherical dimple and protruded textures corresponding to load carrying capacity and friction variable is obtained by performance enhancement ratio (*PER*) using Eqn. 2.29 for each case of texture depth/height considered in every eccentricity ratio in all texture configurations ( $0^\circ - 360^\circ, 0^\circ - 180^\circ$  and  $180^\circ - 360^\circ$ ) to find the optimum texture depth/height and configuration for which the load carrying capacity is maximum and the friction variable is minimum. From Table 5.3, for full textured region configuration, it can be seen that the maximum *PER* value for protruded textured journal bearing is 2.9849 at the eccentricity ratio value of 0.8 and the texture height of 0.4 and for the dimple textured journal bearing is 0.9989 at the eccentricity ratio of 0.8 and the dimple depth of 0.1. In the case of first-half textured region configuration, the maximum *PER* value for protruded textured journal bearing is 1.5558 at the eccentricity ratio of 0.2 and the texture height of 0.4 and for the dimple textured journal bearing is 0.9972 at the eccentricity ratio of 0.8 and the dimple depth of 0.1 as depicted in Table 5.3. From Table 5.3, for the second-half textured region configuration, it can be seen that the maximum *PER* value for protruded textured journal bearing is 3.2940 at the eccentricity ratio of 0.8 and the texture height of 0.4 and for the dimple textured journal bearing is 0.9816 at the eccentricity ratio of 0.8 and the dimple depth of 0.1. Among all the cases of textured region configurations, the maximum *PER* value is obtained for the protruded textured journal bearing in the second-half textured region configuration at the eccentricity ratio of 0.8 and the texture height of 0.4. The flow coefficient has also been found to be maximum for protruded textured journal bearing in the second-half textured region configuration at the eccentricity ratio of 0.8 and the texture height of 0.4.

In the case of journal bearings, the eccentricity ratio may not be assumed as fixed but must be determined corresponding to an imposed load for comparison of performance characteristics of different textured bearings. It is because the load carrying capacity depends on the geometry of the film gap between the journal and the bearing. Therefore, comparison based on eccentricity ratio gives unrealistic and incorrect results. Similarly, the other performance characteristics, such as friction variable and flow coefficient, may not be compared for a given eccentricity ratio as it results in incorrect comparison. Therefore,

performance characteristics of dimple textured journal bearing, protruded textured journal bearing and untextured journal bearing are compared in a quite realistic and correct way as presented below in comparison based on load.

**Table 5.3** Dimple and protruded textured journal bearing performance enhancement ratios

		Performance enhancement ratio (PER)					
$\varepsilon$	$\Delta h$	Full textured region configuration		First-half textured region configuration		Second-half textured region configuration	
		DTB	PTB	DTB	PTB	DTB	PTB
0.2	0.1	0.9465	1.1023	0.9847	1.0233	0.9739	1.0973
	0.2	0.9159	1.2333	0.9756	1.0877	0.9717	1.2648
	0.3	0.8907	1.4232	0.9668	1.2865	0.9700	1.5285
	0.4	0.8589	1.7107	0.9556	1.5558	0.9688	1.9203
0.4	0.1	0.9526	1.0590	0.9778	1.0196	0.9804	1.0491
	0.2	0.9221	1.1945	0.9598	1.0526	0.9761	1.2648
	0.3	0.8972	1.4995	0.9416	1.1810	0.9745	1.5091
	0.4	0.8730	1.7594	0.9224	1.5153	0.9726	2.0571
0.6	0.1	0.9774	1.0941	0.9952	1.0571	0.9696	1.1482
	0.2	0.9648	1.2181	0.9933	1.1401	0.9656	1.4194
	0.3	0.9479	1.4054	0.9847	1.2240	0.9605	1.9029
	0.4	0.9246	1.8474	0.9779	1.3254	0.9586	2.8119
0.8	0.1	0.9989	1.0600	0.9972	1.0718	0.9816	1.2581
	0.2	0.9639	1.4320	0.9918	1.1098	0.9742	2.1419
	0.3	0.9145	2.2740	0.9669	1.1695	0.9702	2.6935
	0.4	0.8696	2.9849	0.9372	1.2671	0.9707	3.2940

**Notes:** DTB: dimple textured bearing PTB: protruded textured bearing

### 5.1.3 Comparison based on load

In this study, the protruded and dimple textured bearing performance characteristics such as minimum fluid film thickness, maximum pressure, friction variable and flow coefficient in non-dimensional quantities are estimated for different texturing configurations, whereas Tala-Ighil et al. [31] have studied the comparison between the dimple textured bearing and plain

bearing performance characteristics. The three different textured region configurations in the circumferential region of journal bearing that have been considered in this analysis are the same as those considered in Sec. 5.1.2. Also, these textured region configurations are the same as those considered by Tala-Ighil et al. [31] in their numerical analysis. In this comparison, the mesh sizes considered for the 3-level situation of the PMD method, the ultimate convergence criterion and the input parameters considered are also the same as considered in Sec. 5.1.2.

The comparison of bearing operating and performance parameters such as eccentricity ratio ( $\varepsilon$ ), non-dimensional minimum film thickness ( $\bar{h}_{\min}$ ), non-dimensional maximum pressure ( $\bar{P}_{\max}$ ), friction variable ( $f$ ) and non-dimensional flow coefficient ( $\bar{Q}$ ) for the protruded and dimple textured journal bearings with the untextured journal bearing has been made for different steady-state loading conditions. For this, initially, the non-dimensional load carrying capacity ( $\bar{W}$ ) for the untextured or plain journal bearing corresponding to different eccentricity ratios varying from 0.2 to 0.7 in increments of 0.1 has been determined and later exact load carrying capacity (up to 3 decimal places) for protruded and dimple textured bearings has been found, in each case, at their respective eccentricity ratios. Based on this procedure, the bearing performance results obtained for the protruded and dimple textured journal bearing have been compared with the untextured bearing.

#### **5.1.3.1 Full textured region configuration ( $0^\circ - 360^\circ$ )**

For the analysis of fully textured region distribution, two rows of 6 textures in the circumferential direction of journal bearing are considered for spherical dimple and protruded textures. For six different imposed loads ( $\bar{W}$ ), bearing operating and performance parameters of dimple textured bearing and protruded textured bearing have been compared with the plain bearing as presented in Table 5.4. It can be noticed from Table 5.4 that in all cases of different loads ( $\bar{W}$ ), slightly higher eccentricity ratios are predicted for dimple textured bearing when compared to plain bearing, whereas slightly lower eccentricity ratios are predicted for protruded textured bearing. The minimum film thickness ( $\bar{h}_{\min}$ ) calculated in the case of dimple textured bearing is lower when compared to plain bearing and further lesser in the case of protruded textured bearing in all cases of loads. Therefore, there is degradation in dimple textured bearing performance in terms of load carrying capacity compared to the plain bearing,

as reported by Tala-Ighil et al. [31] in their numerical study. However, Tala-Ighil et al. [31] conducted their analysis for only one loading condition. There is much reduction in load carrying capacity compared to the plain bearing in the case of protruded textured bearing. The maximum pressure ( $\bar{P}_{\max}$ ) results estimated in all cases of loads are higher for dimple textured bearing and much higher for protruded textured bearing when compared to the plain bearing. The friction variable ( $f$ ) estimated, in all cases of loads, is higher for dimple textured bearing when compared to plain bearing, same as predicted by Tala-Ighil et al. [31]. However, Tala-Ighil et al. [31] have calculated frictional torque in their study. In all cases of loads, the friction variable ( $f$ ) estimated for the protruded textured bearing is lesser compared to the plain bearing. In all cases of loads, the flow coefficient ( $\bar{Q}$ ) estimated is higher for dimple textured bearing when compared to the plain bearing. For protruded textured bearing, the flow coefficient ( $\bar{Q}$ ) predicted is lesser compared to plain bearing in all cases of loads.

The maximum percentage decrement in minimum film thickness ( $\bar{h}_{\min}$ ) of 12.86% is obtained in protruded textured bearing compared to plain bearing at a load of 16.248. For protruded textured bearing, the eccentricity ratio corresponding to that load is 0.694. The maximum percentage increase in the maximum pressure ( $\bar{P}_{\max}$ ) of 41.83% is obtained for protruded textured bearing compared to plain bearing at a load of 4.966. For protruded textured bearing, the eccentricity ratio corresponding to that load is 0.388. The maximum percentage reduction in friction variable ( $f$ ) of 3.66% has been obtained for protruded textured bearing compared to plain bearing at a load of 2.076. The eccentricity ratio corresponding to that load for protruded textured bearing is 0.18. Also, the maximum percentage increment in flow coefficient ( $\bar{Q}$ ) of 3.32% is found in dimple textured bearing compared to plain bearing at a load of 2.076. The eccentricity ratio corresponding to that load for dimple textured bearing is 0.204.

For a few cases of imposed loads among the above-considered cases, bearing performance characteristics are presented in dimensional values in Table 5.5 for a better understanding of dimple textured journal bearing, protruded textured journal bearing and untextured journal bearing performance practically.

**Table 5.4** Comparison of bearing operating and performance parameters for full textured region configuration

$\bar{W}$	$\varepsilon$			$\bar{h}_{\min}$			$\bar{P}_{\max}$			$f$			$\bar{Q}$		
	PB	DTB	PTB	PB	DTB	PTB	PB	DTB	PTB	PB	DTB	PTB	PB	DTB	PTB
2.076	0.2	0.2040	0.1800	0.8000	0.7960	0.7378	0.3409	0.3504	0.3812	13.708	13.877	13.206	0.0723	0.0747	0.0679
3.348	0.3	0.3060	0.2820	0.7000	0.6940	0.6447	0.9400	0.9704	0.9982	8.033	8.053	7.993	0.1027	0.1054	0.1007
4.966	0.4	0.4060	0.3880	0.6000	0.5940	0.5469	1.4004	1.5489	1.9862	5.712	5.739	5.641	0.1346	0.1375	0.1323
7.160	0.5	0.5050	0.4880	0.5000	0.4950	0.4542	2.1044	2.2648	2.4892	4.269	4.295	4.203	0.1659	0.1689	0.1628
10.524	0.6	0.6045	0.5900	0.4000	0.3975	0.3589	3.2603	3.2948	3.5849	3.230	3.238	3.160	0.1974	0.1999	0.1950
16.248	0.7	0.7025	0.6940	0.3000	0.2995	0.2614	5.5328	5.6482	6.2994	2.412	2.421	2.349	0.2281	0.2308	0.2254

89

**Table 5.5** Comparison of bearing operating and performance parameters for full textured region configuration in dimensional form

$W$ (kN)	$e$ ( $\mu\text{m}$ )			$h_{\min}$ ( $\mu\text{m}$ )			$P_{\max}$ (MPa)			$f$			$Q \times 10^{-6}$ ( $\text{m}^3/\text{s}$ )		
	PB	DTB	PTB	PB	DTB	PTB	PB	DTB	PTB	PB	DTB	PTB	PB	DTB	PTB
2.930	11.0	11.2	9.9	44.000	43.780	40.579	0.2440	0.2508	0.2728	13.708	13.877	13.206	2.4598	2.5414	2.3101
10.105	27.5	27.8	26.8	27.500	27.225	24.981	1.5061	1.6209	1.7815	4.269	4.295	4.203	5.6442	5.7463	5.5388
14.853	33.0	33.2	32.4	22.000	21.863	19.739	2.3334	2.3581	2.5657	3.230	3.238	3.160	6.7159	6.8010	6.6343

**Notes:** PB: Plain bearing DTB: Dimple textured bearing PTB: Protruded textured bearing

### 5.1.3.2 First half-textured region configuration ( $0^\circ - 180^\circ$ )

In the analysis of the first half-textured region configuration, two rows of the first three textures in the journal bearing circumferential direction are selected for spherical dimple and protruded textures. Similarly, as shown in the case of full textured region configuration, in this case also, bearing operating and performance parameters of dimple textured bearing and protruded textured bearing have been compared with the plain bearing for six different cases of imposed load ( $\bar{W}$ ) as shown in Table 5.6. From Table 5.6, it is seen that slightly higher eccentricity ratios are predicted for dimple textured bearing when compared to plain bearing, whereas slightly lower eccentricity ratios are predicted for protruded textured bearing in all cases of different loads ( $\bar{W}$ ). In all cases of loads, the minimum film thickness ( $\bar{h}_{\min}$ ) predicted for dimple textured bearing is lesser when compared to plain bearing and further lesser for protruded textured bearing. Hence, the load carrying capacity of dimple textured journal bearing is lower compared to the plain bearing in the same way as predicted by Tala-Ighil et al. [31]. The protruded textured bearing has a further lower load carrying capacity than the plain bearing. The maximum pressure ( $\bar{P}_{\max}$ ) results calculated in all cases of loads are higher for dimple textured bearing when compared to plain bearing and much higher for protruded textured bearing. In all cases of loads, the friction variable ( $f$ ) calculated is higher for dimple textured bearing when compared to plain bearing, same as reported by Tala-Ighil et al. [31]. The friction variable ( $f$ ) predicted for the protruded textured bearing is lesser compared to plain bearing in all cases of loads. In all cases of loads, the flow coefficient ( $\bar{Q}$ ) calculated is higher for dimple textured bearing when compared to the plain bearing. For protruded textured bearing, the flow coefficient ( $\bar{Q}$ ) calculated is lesser compared to plain bearing in all cases of loads.

The maximum percentage decrement in minimum film thickness ( $\bar{h}_{\min}$ ) of 10.03% is obtained in protruded textured bearing compared to plain bearing at a load of 16.248. The eccentricity ratio corresponding to that load for the protruded textured bearing is 0.685. The maximum percentage increase in the maximum pressure ( $\bar{P}_{\max}$ ) of 41.82% is obtained for protruded textured bearing compared to plain bearing at a load of 4.966. For protruded textured bearing, the eccentricity ratio corresponding to that load is 0.388. The maximum percentage

**Table 5.6** Comparison of bearing operating and performance parameters for first-half textured region configuration

$\bar{W}$	$\varepsilon$			$\bar{h}_{\min}$			$\bar{P}_{\max}$			$f$			$\bar{Q}$		
	PB	DTB	PTB	PB	DTB	PTB	PB	DTB	PTB	PB	DTB	PTB	PB	DTB	PTB
2.076	0.2	0.2020	0.1800	0.8000	0.7980	0.7378	0.3409	3.3468	0.3811	13.708	13.804	13.543	0.0723	0.0728	0.0720
3.348	0.3	0.3005	0.2820	0.7000	0.6995	0.6447	0.9400	0.9486	0.9983	8.033	8.047	7.998	0.1027	0.1030	0.1024
4.966	0.4	0.4050	0.3880	0.6000	0.5950	0.5469	1.4004	1.5204	1.9860	5.712	5.734	5.653	0.1346	0.1349	0.1341
7.160	0.5	0.5040	0.4860	0.5000	0.4960	0.4561	2.1044	2.2604	2.3916	4.269	4.281	4.253	0.1659	0.1662	0.1650
10.524	0.6	0.6040	0.5850	0.4000	0.3960	0.3636	3.2603	3.3102	3.5046	3.230	3.234	3.194	0.1974	0.1979	0.1960
16.248	0.7	0.7010	0.6850	0.3000	0.2990	0.2699	5.5328	5.6513	6.0162	2.412	2.420	2.393	0.2281	0.2286	0.2258

**Notes:** PB: Plain bearing DTB: Dimple textured bearing PTB: Protruded textured bearing

decrement in friction variable ( $f$ ) of 1.2% has been found for protruded textured bearing compared to plain bearing at a load of 2.076. The eccentricity ratio corresponding to that load for protruded textured bearing is 0.18. The maximum percentage increase in flow coefficient ( $\bar{Q}$ ) of 0.69% is found in dimple textured bearing compared to plain bearing at a load of 2.076. The eccentricity ratio corresponding to that load for dimple textured bearing is 0.202.

### 5.1.3.3 Second half-textured region configuration ( $180^\circ - 360^\circ$ )

In the present analysis of the second half-textured region configuration, two rows of 3 textures in the second-half circumferential region of journal bearing are selected for spherical dimple and protruded textures. Table 5.7 presents bearing operating and performance parameters of dimple textured and protruded textured bearing compared with the plain bearing for different imposed loads ( $\bar{W}$ ). From Table 5.7, it is observed that in all cases of different loads ( $\bar{W}$ ), eccentricity ratios predicted for dimple textured bearing are lesser when compared to plain bearing, whereas eccentricity ratios predicted for protruded textured bearing are further lesser. The minimum film thickness ( $\bar{h}_{\min}$ ) determined in the case of dimple textured bearing is higher when compared to plain bearing and lesser in the case of protruded textured bearing in all cases of loads. Therefore, there is performance enhancement in dimple textured bearing in terms of load carrying capacity when compared to the plain bearing, as predicted by Tala-Ighil et al. [31]. In the case of protruded textured bearing, there is a decrement in load carrying capacity compared to the plain bearing. The maximum pressure ( $\bar{P}_{\max}$ ) results found are lesser for dimple textured bearing and much higher for protruded textured bearing, when compared to plain bearing, in all cases of loads. The friction variable ( $f$ ) obtained, in all cases of load carrying capacities, is higher for dimple textured bearing compared to plain bearing, whereas it is lesser for protruded textured bearing. The flow coefficient ( $\bar{Q}$ ) obtained is higher for dimple textured bearing when compared to plain bearing, whereas it is lesser for protruded textured bearing in all cases of loads.

The maximum percentage reduction in minimum film thickness ( $\bar{h}_{\min}$ ) of 8.7% is obtained in protruded textured bearing compared to plain bearing at a load of 2.076. The eccentricity ratio corresponding to that load for the protruded textured bearing is 0.198. The

**Table 5.7** Comparison of bearing operating and performance parameters for second-half textured region configuration

$W$	$\varepsilon$			$\bar{h}_{\min}$			$\bar{P}_{\max}$			$f$			$\bar{Q}$		
	PB	DTB	PTB	PB	DTB	PTB	PB	DTB	PTB	PB	DTB	PTB	PB	DTB	PTB
2.076	0.2	0.1990	0.1980	0.8000	0.8010	0.7304	0.3409	0.3384	0.3984	13.708	13.934	13.128	0.0723	0.0753	0.0664
3.348	0.3	0.2965	0.2960	0.7000	0.7035	0.6446	0.9400	0.9006	0.9998	8.0330	8.054	7.991	0.1027	0.1056	0.0999
4.966	0.4	0.3995	0.3990	0.6000	0.6005	0.5533	1.4004	1.3982	1.9641	5.712	5.794	5.628	0.1346	0.1379	0.1314
7.160	0.5	0.4990	0.4980	0.5000	0.5010	0.4648	2.1044	2.0964	2.3412	4.269	4.299	4.048	0.1659	0.1691	0.1616
10.524	0.6	0.5980	0.5970	0.4000	0.4020	0.3756	3.2603	3.2504	3.3918	3.230	3.260	3.152	0.1974	0.2013	0.1938
16.248	0.7	0.6970	0.6960	0.3000	0.3030	0.2854	5.5328	5.5428	5.8216	2.412	2.501	2.338	0.2281	0.2402	0.2246

**Notes:** PB: Plain bearing DTB: Dimple textured bearing PTB: Protruded textured bearing

maximum percentage increase in the maximum pressure ( $\bar{P}_{\max}$ ) of 40.25% is found in protruded textured bearing compared to plain bearing at a load of 4.966. For protruded textured bearing, the eccentricity ratio corresponding to that load is 0.399. The maximum percentage decrement in friction variable ( $f$ ) of 5.18% has been obtained for protruded textured bearing compared to plain bearing at a load of 7.160. The eccentricity ratio corresponding to that load for the protruded textured bearing is 0.498. Also, the maximum percentage increase in flow coefficient ( $\bar{Q}$ ) of 5.3% is found in dimple textured bearing compared to plain bearing at a load of 16.248. The eccentricity ratio corresponding to that load for dimple textured bearing is 0.697.

#### **5.1.3.4 Percentage change in performance characteristics**

The percentage change in friction variable ( $f$ ) and flow coefficient ( $\bar{Q}$ ) for dimple textured bearing and protruded textured bearing with respect to plain bearing in case of full textured (FT), first-half textured (FHT) and second-half textured (SHT) region configurations are presented in Table 5.8. It can be seen from Table 5.8 that there is a percentage increment in friction variable for dimple textured bearing, in all cases of load, of full textured, first-half textured and second-half textured region configurations with respect to the plain bearing, which is an undesirable result. The poor performance of dimple textured bearing related to friction variable is found in second-half textured region configurations followed by full textured and first-half textured region configurations, respectively. For protruded textured bearing, it can be observed from Table 5.8 that there is a percentage reduction in friction variable of full textured, first-half textured and second-half textured region configurations with respect to plain bearing in all cases of load, which is a desirable outcome. The better performance of protruded textured bearing related to friction variable is found in second-half textured region configuration followed by full textured and first-half textured region configurations, respectively. Table 5.8 depicts a percentage increment in flow coefficient for dimple textured bearing of full textured, first-half textured and second-half textured region configurations with respect to plain bearing in all cases of loads which is a desirable result. The better performance of dimple textured bearing related to flow coefficient is observed in second-half textured region configuration followed by full textured and first-half textured

**Table 5.8** Percentage change in the performance parameters of textured journal bearings

$\bar{W}$	% change in friction variable ( $f$ )						% change in flow coefficient ( $\bar{Q}$ )					
	Dimple textured bearing			Protruded textured bearing			Dimple textured bearing			Protruded textured bearing		
	FT	FHT	SHT	FT	FHT	SHT	FT	FHT	SHT	FT	FHT	SHT
2.076	1.23	0.7	1.65	-3.66	-1.2	-4.23	3.32	0.69	4.15	-6.09	-0.41	-8.16
3.348	0.25	0.17	0.26	-0.5	-0.44	-0.52	2.63	0.29	2.82	-1.95	-0.29	-2.73
4.966	0.47	0.39	1.44	-1.24	-1.03	-1.47	2.15	0.22	2.45	-1.71	-0.37	-2.38
7.160	0.61	0.28	0.7	-1.55	-0.37	-5.18	1.81	0.18	1.93	-1.87	-0.54	-2.59
10.524	0.25	0.12	0.93	-2.17	-1.11	-2.41	1.27	0.25	1.98	-1.22	-0.71	-1.82
16.248	0.37	0.33	3.69	-2.61	-0.79	-3.07	1.18	0.22	5.3	-1.18	-1.01	-1.53

**Notes:** FT: Full textured FHT: First-half textured SHT: Second-half textured

region configurations, respectively. For protruded textured bearing, it can be seen from Table 5.8 that there is a percentage reduction in the flow coefficient of full textured, first-half textured and second-half textured region configurations with respect to plain bearing in all cases of load, which is an undesirable result. The poor performance of protruded textured bearing related to flow coefficient is seen in the second-half textured region configuration followed by full textured and first-half textured region configurations, respectively. From Table 5.8, in all texture region configurations, it can be observed that the maximum percentage reduction in friction variable ( $f$ ) of 5.18% has been obtained for protruded textured bearing at a load of 7.160. For protruded textured bearing, the eccentricity ratio corresponding to that load is 0.18. Further, the maximum percentage increase in flow coefficient ( $\bar{Q}$ ) of 5.3% is obtained in dimple textured bearing at a load of 16.248. For dimple textured bearing, the eccentricity ratio corresponding to that load is 0.697.

#### 5.1.3.5 Pressure and film thickness profiles

The pressure and film thickness profiles of dimple textured bearing, textured in the second-half textured region configuration, for the minimum and maximum loads considered in the analysis are depicted in Fig. 5.11. The pressure and film thickness profiles are presented for dimple textured bearing when textured in the second-half textured region configuration as it has provided the improvement in bearing performance in terms of load carrying capacity (i.e., increase in  $\bar{h}_{\min}$ ) when compared to the plain and protruded textured bearing whereas in other texture configurations there is degradation in the performance of dimple and protruded textured bearings when compared to the plain bearings. Figures 5.11 (a) and 5.11 (b) show that the minimum film thickness and maximum pressure values corresponding to the minimum load of 2.076 are 0.8010 and 0.3402, respectively. Figures 5.11 (c) and 5.11 (d) show that the minimum film thickness and maximum pressure values corresponding to the maximum load of 16.248 are 0.3030 and 5.3962, respectively.

In this numerical analysis, it is found that protruded texture is advantageous compared to dimple texture, when the journal bearing is textured in second half textured region configuration, with respect to friction variable but it is converse with respect to load carrying capacity and flow coefficient. However, in practice, it is difficult to manufacture protruded

textures on the bearing surface compared to the dimple textures. The protruded textures are also susceptible to wear during operation of the bearing whereas, the dimple textures can trap wear debris and can act as small reservoirs during starved lubrication.

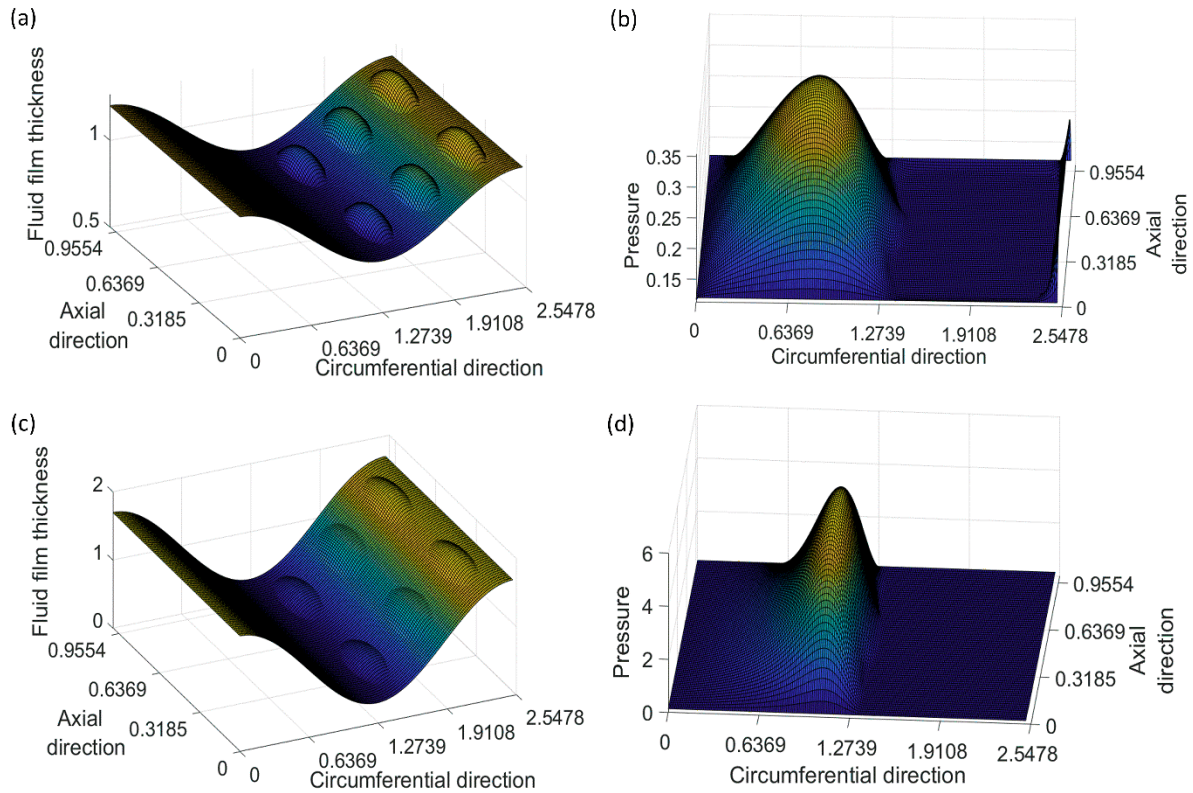


**Fig. 5.11** Film thickness and pressure profiles corresponding to the minimum and maximum loads

## 5.2 Summary

In this study, the performance characteristics of a dimple textured journal bearing and protruded textured journal bearing have been compared to the untextured journal bearing to determine whether the spherical dimples or spherical protuberances on the bearing surface produce better bearing performance in terms of load carrying capacity, friction variable and flow coefficient. The governing Reynolds equation has been solved considering the mass conserving (JFO) boundary conditions using the PMD method, which is computationally efficient and easy to implement compared to the MG method. Two ways of comparison have been presented, one based on eccentricity ratio and the other based on load. From the

comparison based on eccentricity ratio, the optimum texture and bearing operating parameters have been found corresponding to the maximum load carrying capacity, minimum friction variable and maximum flow coefficient. Similarly, from the comparison based on load, the best texture configuration has been determined corresponding to the maximum load carrying capacity, minimum friction variable and maximum flow coefficient. From the comparison based on eccentricity ratio, protruded textured journal bearing, when textured in the second half textured region configuration, gives better performance characteristics than dimple texture journal bearing and untextured journal bearing irrespective of any texture region configuration. However, from the comparison based on load, the dimple textured journal bearing gives better performance, in terms of load carrying capacity and flow coefficient, compared to protruded textured journal bearing and untextured journal bearing irrespective of any texture region configuration when textured in the second half textured region configuration. For friction variable, protruded textured journal bearing gives better performance when textured in the second half textured region configuration. The results predicted from comparison based on load are different than those obtained from comparison based on eccentricity ratio. It is because the effective eccentricity ratio for a given load may be different for dimple textured journal bearing, protruded textured journal bearing and untextured journal bearing. Since load carrying capacity depends on the geometry of the film gap present between journal and bearing, the results obtained from comparison based on load are more realistic than the results obtained from comparison based on eccentricity ratio. Even though many published results are available in which performance characteristics are found based on eccentricity ratio, in fact, for realistic analysis, the performance characteristics are found based on load.

## Concluding remarks

---

### 6.0 Introduction

This thesis deals with the implementation of the progressive mesh densification (PMD) method to textured journal bearing problems and to compare its computational efficiency with the computational efficiencies of multigrid (MG) and Fixed mesh density (FMD) methods for a fixed set of texture parameters and also for varying texture parameters. Further, comparison of performance characteristics of dimple textured and protruded textured journal bearings with untextured journal bearing implementing mass conserving boundary conditions using PMD method. Here, performance characteristics are compared in two different ways. One comparison is based on eccentricity ratio and the other comparison is based on load. As the comparison of performance characteristics based on load is quite realistic and correct than the comparison of performance characteristics based on eccentricity ratio, the inferences and conclusions drawn from the comparison based on load are presented below.

The scope of the present work has been defined based on the literature review presented in Chapter 1. The basic equations, mathematical formulations in theories for textured journal bearing using different boundary conditions and computational methods are presented in Chapter 2. In Chapter 3, the comparison of computational efficiencies of PMD, MG and FMD methods for dimple textured journal bearing problems for a fixed set of textured parameters for different  $L/D$  ratios is presented. A similar study is carried out for varying texture parameters, for the  $L/D$  ratio of unity, in Chapter 4. In Chapter 5, the spherical protruded and dimple textured journal bearings' performance characteristics are compared with the untextured bearing for different texture configurations for the  $L/D$  ratio of unity.

## 6.1 Inferences

The inferences that are drawn from the results presented in this thesis are:

- In the case of the textured journal bearing of  $L/D = 0.2$ , for fixed set of texture parameters, the MG method has better computational efficiency compared to the PMD method and the FMD method.
- In the case of the textured bearing of  $L/D = 1$ , there is above 12% and 94% reduction in the number of iterations to reach the converged solution in Scheme 1 of the PMD method, when there is above 9% and 93% reduction in the number of iterations to reach the converged solution in Scheme 2 of the PMD method, compared to the MG and the FMD methods, respectively for a fixed set of texture parameters.
- In the case of the textured bearing of  $L/D = 2$ , Scheme 1 has a better reduction in the number of iterations than Scheme 2, compared to the MG and the FMD methods, respectively, for a fixed set of texture parameters.
- From all the cases of texture parameter variation considered for the bearing of  $L/D = 1$ , the number of iterations taken by Scheme 1 to obtain the converged solution is less than 0.88 and 0.19 times those of the MG method and FMD method, respectively. Furthermore, the computing speed of Scheme 1 is at least 1.2 and 2.9 compared to the MG and FMD methods, respectively.
- It is also noticed that Scheme 2 of the PMD method is computationally better compared to the MG and FMD methods, irrespective of any texture parameter value considered for bearing of  $L/D = 1$ .
- The maximum reduction in friction variable of 5.18% is found in protruded textured bearing with respect to untextured bearing at an imposed load of 7.160.
- The maximum increase in flow coefficient of 5.3% is found in dimple textured bearing with respect to untextured bearing at an imposed load of 16.248.

## 6.2 Conclusions

The conclusions that are drawn from the results presented in this thesis are:

- The PMD method is the simplest and easiest in implementation compared to the MG method for solving problems pertaining to textured journal bearings.
- The PMD method has better computational efficiency in terms of computational time and the number of iterations compared to MG and FMD methods for bearing of  $L/D = 1$ , irrespective of any texture parameter value considered.
- Scheme 1 of the PMD method is the computationally superior one compared to Scheme 2 of the PMD, MG method and FMD method, irrespective of any texture parameter value considered. However, the '*orf*' values need to be looked into, within Scheme 1, for better accuracy and computational efficiency.
- Implementation of the cavitation algorithm with modified switch function [87] for mass conserving boundary conditions has been difficult for textured journal bearing problems due to convergence issues.
- The dimple textured bearing produces enhancement in load carrying capacity (i.e., increase in  $\bar{h}_{\min}$ ) when the bearing is textured with spherical dimples in the second-half textured region configuration. This is the same as previously concluded by Tala-Ighil et al. [31] in their numerical study. However, Tala-Ighil et al. [31] conducted their study for only one loading condition.
- The protruded textured bearing doesn't improve the load carrying capacity when the bearing is textured with spherical protuberances in the second-half textured region configuration.
- The bearing textured with spherical dimples or spherical protuberances in the full or first-half textured region configuration doesn't improve the load carrying capacity.
- The protruded textured bearing produces the best performance in terms of friction variable when the bearing is textured with spherical protuberances in the second-half textured region configuration in comparison to other texture configurations, whereas

dimple textured bearing produces degradation in performance irrespective of any texture region configuration.

- The dimple textured bearing produces the best performance in terms of flow coefficient when the bearing is textured with spherical dimples in the second-half textured region configuration in comparison to other texture configurations whereas protruded textured bearing produces degradation in performance irrespective of any texture configuration.

The results presented here clearly demonstrate that the PMD method is very efficient for solving Textured journal bearing problems for an  $L/D$  ratio of unity. Therefore, the PMD method is highly recommended for such problems. Within the PMD method, Scheme 1 has better computational performance compared to Scheme 2. Further, it is demonstrated that protruded textured journal bearing gives better performance compared to the dimple textured and untextured journal bearing for friction variable when textured in the second-half textured region whereas dimple textured journal bearing provides better performance compared to the protruded textured and untextured journal bearing for load carrying capacity and flow coefficient when textured in second-half textured region.

### 6.3 Scope for future works

- Analysis on the influence of texture parameters on computational efficiencies of PMD, MG and FMD methods while solving problems pertaining to dimple textured journal bearing for different  $L/D$  ratios.
- Implementation of PMD method to the textured journal bearing problems and to compare its computational efficiency with the computational efficiencies of MG and FMD methods for a fixed set of texture parameters and also for varying texture parameters using mass conserving boundary conditions.
- Numerical investigation of the optimum texture and bearing parameters that provide the best bearing performance characteristics using mass conserving boundary conditions.
- Experimental investigation on the influence of spherical protruded and dimple textures on the journal bearing performance with consideration of wear in protruded textures.

# References

---

- [1] Manser, B., Belaidi, I., Khelladi, S., Chikh, M.A.A., Deligant, M. and Bakir, F., 2020. Computational investigation on the performance of hydrodynamic micro-textured journal bearing lubricated with micropolar fluid using mass-conserving numerical approach. *Proceedings of the Institution of Mechanical Engineers, Part J: Journal of Engineering Tribology*, 234(8), pp.1310-1331.
- [2] Hargreaves, D.J., 1991. Surface waviness effects on the load-carrying capacity of rectangular slider bearings. *Wear*, 145(1), pp.137-151.
- [3] Dobrica, M.B., Fillon, M., Pascovici, M.D. and Cicone, T., 2010. Optimizing surface texture for hydrodynamic lubricated contacts using a mass-conserving numerical approach. *Proceedings of the Institution of Mechanical Engineers, Part J: Journal of Engineering Tribology*, 224(8), pp.737-750.
- [4] Ma, C. and Zhu, H., 2011. An optimum design model for textured surface with elliptical-shape dimples under hydrodynamic lubrication. *Tribology International*, 44(9), pp.987-995.
- [5] Yu, H., Deng, H., Huang, W. and Wang, X., 2011. The effect of dimple shapes on friction of parallel surfaces. *Proceedings of the Institution of Mechanical Engineers, Part J: Journal of Engineering Tribology*, 225(8), pp.693-703.
- [6] Fowell, M.T., Medina, S., Olver, A.V., Spikes, H.A. and Pegg, I.G., 2012. Parametric study of texturing in convergent bearings. *Tribology International*, 52(2012), pp.7-16.
- [7] Ismail, S. and Sarangi, M., 2013, December. Influence of texture orientation on the hydrodynamic lubrication. *In 1st International and 16th national conference on machines and mechanisms IIT Roorkee*, pp.18-20.
- [8] Gherca, A., Fatu, A., Hajjam, M. and Maspeyrot, P., 2013. Influence of surface geometry on the hydrodynamic performances of parallel bearings in transient flow conditions. *Tribology transactions*, 56(6), pp.953-967.

- [9] Malik, S. and Kakoty, S.K., 2014. Analysis of dimple textured parallel and inclined slider bearing. *Proceedings of the Institution of Mechanical Engineers, Part J: Journal of Engineering Tribology*, 228(12), pp.1343-1357.
- [10] Ji, J., Fu, Y. and Bi, Q., 2014. Influence of geometric shapes on the hydrodynamic lubrication of a partially textured slider with micro-grooves. *Journal of Tribology*, 136(4), p.041702.
- [11] Shen, C. and Khonsari, M.M., 2015. Numerical optimization of texture shape for parallel surfaces under unidirectional and bidirectional sliding. *Tribology International*, 82(2015), pp.1-11.
- [12] Singh, D., Singh, N. and Awasthi, R.K., 2018. Effect of surface texture parameters on the performance of finite slider bearing. *Materials Today: Proceedings*, 5(9), pp.19349-19358.
- [13] Han, Y. and Fu, Y., 2018. Investigation of surface texture influence on hydrodynamic performance of parallel slider bearing under transient condition. *Meccanica*, 53(8), pp.2053-2066.
- [14] Fu, H., Ji, J., Fu, Y. and Hua, X., 2018. Influence of donut-shaped bump on the hydrodynamic lubrication of textured parallel sliders. *Journal of Tribology*, 140(4), p.041706.
- [15] Brizmer, V., Kligerman, Y. and Etsion, I., 2003. A laser surface textured parallel thrust bearing. *Tribology transactions*, 46(3), pp.397-403.
- [16] Etsion, I., Halperin, G., Brizmer, V. and Kligerman, Y., 2004. Experimental investigation of laser surface textured parallel thrust bearings. *Tribology Letters*, 17(2), pp.295-300.
- [17] Wang, X., Kato, K., Adachi, K. and Aizawa, K., 2003. Loads carrying capacity map for the surface texture design of SiC thrust bearing sliding in water. *Tribology international*, 36(3), pp.189-197.
- [18] Etsion, I., 2004. Improving tribological performance of mechanical components by laser surface texturing. *Tribology letters*, 17(4), pp.733-737.

- [19] Buscaglia, G.C., Ciuperca, I. and Jai, M., 2005. The effect of periodic textures on the static characteristics of thrust bearings. *Journal of Tribology*, 127(4), pp.899-902.
- [20] Rahmani, R., Shirvani, A. and Shirvani, H., 2007. Optimization of partially textured parallel thrust bearings with square-shaped micro-dimples. *Tribology Transactions*, 50(3), pp.401-406.
- [21] Papadopoulos, C.I., Efstathiou, E.E., Nikolakopoulos, P.G. and Kaiktsis, L., 2011. Geometry optimization of textured three-dimensional micro-thrust bearings. *Journal of Tribology*, 133(3), p.041702.
- [22] Qiu, Y. and Khonsari, M.M., 2009. On the prediction of cavitation in dimples using a mass-conservative algorithm. *Journal of Tribology*, 131(4), p.041702.
- [23] Marian, V.G., Gabriel, D., Knoll, G. and Filippone, S., 2011. Theoretical and experimental analysis of a laser textured thrust bearing. *Tribology letters*, 44(3), pp.335-343.
- [24] Shen, C. and Khonsari, M.M., 2013. Effect of dimple's internal structure on hydrodynamic lubrication. *Tribology Letters*, 52(3), pp.415-430.
- [25] Henry, Y., Bouyer, J. and Fillon, M., 2015. An experimental analysis of the hydrodynamic contribution of textured thrust bearings during steady-state operation: A comparison with the untextured parallel surface configuration. *Proceedings of the Institution of Mechanical Engineers, Part J: Journal of Engineering Tribology*, 229(4), pp.362-375.
- [26] Gherca, A., Fatu, A., Hajjam, M. and Maspeyrot, P., 2016. Influence of surface texturing on the hydrodynamic performance of a thrust bearing operating in steady-state and transient lubrication regime. *Tribology International*, 102(2016), pp.305-318.
- [27] Fu, G. and Untaroiu, A., 2017. An optimum design approach for textured thrust bearing with elliptical-shape dimples using computational fluid dynamics and design of experiments including cavitation. *Journal of Engineering for Gas Turbines and Power*, 139(9), p.092502.
- [28] Panigrahi, D.K. and Sarangi, M., 2020. Tribological performance of positive deterministic textured surfaces in parallel sliding lubricated contacts: effect of texture size and height.

*Proceedings of the Institution of Mechanical Engineers, Part J: Journal of Engineering Tribology*, 234(12), pp.1908-1925.

[29] Zhirong, T., Xiangkai, M., Yi, M. and Xudong, P., 2021. Shape optimization of hydrodynamic textured surfaces for enhancing load-carrying capacity based on level set method. *Tribology International*, 162(2021), p.107136.

[30] Sinanoğlu, C., Nair, F. and Karamış, M.B., 2005. Effects of shaft surface texture on journal bearing pressure distribution. *Journal of materials processing technology*, 168(2), pp.344-353.

[31] Tala-Ighil, N., Maspeyrot, P., Fillon, M. and Bounif, A., 2007. Effects of surface texture on journal-bearing characteristics under steady-state operating conditions. *Proceedings of the Institution of Mechanical Engineers, Part J: Journal of Engineering Tribology*, 221(6), pp.623-633.

[32] Ausas, R., Ragot, P., Leiva, J., Jai, M., Bayada, G. and Buscaglia, G.C., 2007. The impact of the cavitation model in the analysis of microtextured lubricated journal bearings. *Journal of Tribology*, 129(4), pp.865-875.

[33] Lu, X. and Khonsari, M.M., 2007. An experimental investigation of dimple effect on the stribeck curve of journal bearings. *Tribology letters*, 27(2), pp.169-176.

[34] Tala-Ighil, N., Maspeyrot, P., Fillon, M. and Bounif, A., 2007. Hydrodynamic effects of texture geometries on journal bearing surfaces. In *10th International Conference on Tribology ROTRIB'07, Bucharest, Romania from 8 to 10 November 2007*.

[35] Cupillard, S., Glavatskih, S. and Cervantes, M.J., 2008. Computational fluid dynamics analysis of a journal bearing with surface texturing. *Proceedings of the Institution of Mechanical Engineers, Part J: Journal of Engineering Tribology*, 222(2), pp.97-107.

[36] Tala-Ighil, N., Fillon, M. and Maspeyrot, P., 2011. Effect of textured area on the performances of a hydrodynamic journal bearing. *Tribology international*, 44(3), pp.211-219.

- [37] Kango, S., Singh, D. and Sharma, R.K., 2012. Numerical investigation on the influence of surface texture on the performance of hydrodynamic journal bearing. *Meccanica*, 47(2), pp.469-482.
- [38] Brizmer, V. and Kligerman, Y., 2012. A laser surface textured journal bearing. *Journal of Tribology*, 134(3), p.031702.
- [39] Rao, T.V.V.L.N., Rani, A.M.A., Nagarajan, T. and Hashim, F.M., 2012. Analysis of slider and journal bearing using partially textured slip surface. *Tribology International*, 56(2012), pp.121-128.
- [40] Li, J. and Wang, X., 2013. Numerical simulation of the influence of the bulges around laser surface textures on the tribological performance. *Tribology Transactions*, 56(6), pp.1011-1018.
- [41] Gupta, K.K., Kumar, R., Kumar, H. and Sharma, M., 2013. Study on effect of surface texture on the performance of hydrodynamic journal bearing. *International Journal of Engineering and Advanced Technology*, 3(1), pp.49-54.
- [42] Kango, S., Sharma, R.K. and Pandey, R.K., 2014. Comparative analysis of textured and grooved hydrodynamic journal bearing. *Proceedings of the Institution of Mechanical Engineers, Part J: Journal of Engineering Tribology*, 228(1), pp.82-95.
- [43] Lu, Y., Liu, Y., Wang, J. and Liu, H., 2014. Experimental investigation into friction performance of dimples journal bearing with phyllotactic pattern. *Tribology letters*, 55(2), pp.271-278.
- [44] Ganji, T.S. and Kakoty, S.K., 2014. Analysis on micro elliptical textured journal bearing. *International Journal of Current Engineering and Technology*, 2(2), pp.648-650.
- [45] Tala-Ighil, N. and Fillon, M., 2015. Surface texturing effect comparative analysis in the hydrodynamic journal bearings. *Mechanics & Industry*, 16(3), p.302.
- [46] Zhang, H., Dong, G., Hua, M., Guo, F. and Chin, K.S., 2015. Parametric design of surface textures on journal bearing. *Industrial lubrication and Tribology*. 67(4), pp.359-369.

- [47] Meng, F.M., Zhang, L., Liu, Y. and Li, T.T., 2015. Effect of compound dimple on tribological performances of journal bearing. *Tribology International*, 91, pp.99-110.
- [48] Liang, X., Liu, Z., Wang, H., Zhou, X. and Zhou, X., 2016. Hydrodynamic lubrication of partial textured sliding journal bearing based on three-dimensional CFD. *Industrial Lubrication and Tribology*. 68(1), pp.106-115.
- [49] Dadouche, A. and Conlon, M.J., 2016. Operational performance of textured journal bearings lubricated with a contaminated fluid. *Tribology International*, 93(2016), pp.377-389.
- [50] Khatri, C.B. and Sharma, S.C., 2016. Influence of textured surface on the performance of non-recessed hybrid journal bearing operating with non-Newtonian lubricant. *Tribology International*, 95(2016), pp.221-235.
- [51] Sharma, N., Kango, S., Tayal, A., Sharma, R.K. and Sunil, 2016. Investigations on the influence of surface texturing on a couple stress fluid-based journal bearing by using JFO boundary conditions. *Tribology Transactions*, 59(3), pp.579-584.
- [52] Yamada, H., Taura, H. and Kaneko, S., 2017. Static characteristics of journal bearings with square dimples. *Journal of Tribology*, 139(5), p.051703.
- [53] Shinde, A.B. and Pawar, P.M., 2017. Multi-objective optimization of surface textured journal bearing by Taguchi based Grey relational analysis. *Tribology International*, 114(2017), pp.349-357.
- [54] Guo, B., 2017. Optimal surface texture design of journal bearing with axial grooves. *International Journal of Heat and Technology*, 35(2), pp.267-272.
- [55] Usman, A. and Park, C.W., 2018. Numerical optimization of surface texture for improved tribological performance of journal bearing at varying operating conditions. *Industrial Lubrication and Tribology*. 70(9), pp.1608-1618.
- [56] Shinde, A., Pawar, P., Shaikh, P., Wangikar, S., Salunkhe, S. and Dhamgaye, V., 2018. Experimental and numerical analysis of conical shape hydrodynamic journal bearing with partial texturing. *Procedia Manufacturing*, 20(2018), pp.300-310.

- [57] Mao, Y., Jianxi, Y., Wenjing, X. and Yonggang, L., 2019. Study on the influence of round pits arrangement patterns on tribological properties of journal bearings. *Industrial Lubrication and Tribology*, 71(7), pp.931-941.
- [58] Sharma, S., Jamwal, G. and Awasthi, R.K., 2019. Enhancement of steady state performance of hydrodynamic journal bearing using chevron-shaped surface texture. *Proceedings of the Institution of Mechanical Engineers, Part J: Journal of Engineering Tribology*, 233(12), pp.1833-1843.
- [59] Galda, L., Sep, J., Olszewski, A. and Zochowski, T., 2019. Experimental investigation into surface texture effect on journal bearings performance. *Tribology International*, 136(2019), pp.372-384.
- [60] Korenaga, A., Mano, H., Omura, A., Ohana, T., Aso, S., Sadakata, K., Tanabe, S., Akiyama, Y. and Habuki, F., 2020. Friction reduction of oil-impregnated sintered bearings by surface texturing. *Journal of Tribology*, 142(9), p.091801.
- [61] Singh, N. and Awasthi, R.K., 2020. Influence of dimple location and depth on the performance characteristics of the hydrodynamic journal bearing system. *Proceedings of the Institution of Mechanical Engineers, Part J: Journal of Engineering Tribology*, 234(9), pp.1500-1513.
- [62] Manser, B., Belaidi, I., Hamrani, A., Khelladi, S. and Bakir, F., 2020. Texture shape effects on hydrodynamic journal bearing performances using mass-conserving numerical approach. *Tribology-Materials, Surfaces & Interfaces*, 14(1), pp.33-50.
- [63] Singh, N. and Awasthi, R.K., 2021. Influence of texture geometries on the performance parameters of hydrodynamic journal bearing. *Proceedings of the Institution of Mechanical Engineers, Part J: Journal of Engineering Tribology*, 235(10), pp.2056-2072.
- [64] Awasthi, R.K. and Maan, J.S., 2021. Influence of surface texture on the performance of hydrodynamic journal bearing operating under turbulent regime. *Tribology Online*, 16(2), pp.99-112.

- [65] Filgueira Filho, I.C.M., Bottene, A.C., Silva, E.J. and Nicoletti, R., 2021. Static behavior of plain journal bearings with textured journal-experimental analysis. *Tribology International*, 159(2021), p.106970.
- [66] Zhu, D., 2007. On some aspects of numerical solutions of thin-film and mixed elastohydrodynamic lubrication. *Proceedings of the Institution of Mechanical Engineers, Part J: Journal of Engineering Tribology*, 221(5), pp.561-579.
- [67] Pu, W., Wang, J. and Zhu, D., 2016. Progressive mesh densification method for numerical solution of mixed elastohydrodynamic lubrication. *Journal of Tribology*, 138(2), p.021502.
- [68] Kumar, R., Azam, M.S., Ghosh, S.K. and Khan, H., 2019. Thermo-elastohydrodynamic lubrication simulation of the Rayleigh step bearing using the progressive mesh densification method. *Simulation*, 95(5), pp.395-410.
- [69] Kumar, R., Azam, M.S. and Ghosh, S.K., 2019. Influence of stochastic roughness on performance of a Rayleigh step bearing operating under Thermo-elastohydrodynamic lubrication considering shear flow factor. *Tribology International*, 134, pp.264-280.
- [70] Kumar, R., Azam, M.S., Ghosh, S.K. and Khan, H., 2017. Effect of surface roughness and deformation on Rayleigh step bearing under thin film lubrication. *Industrial Lubrication and Tribology*, 69(6), pp.1016-1032.
- [71] Kumar, R., Azam, M.S., Ghosh, S.K. and Khan, H., 2019. Performance evaluation of rough thrust pad bearing under thermo-elastohydrodynamic lubrication using an improved iterative method. *Mechanics & Industry*, 20(1), p.110.
- [72] Kumar, R. and Azam, M.S., 2021. Effect of directionally oriented random roughness on performance of a Rayleigh step bearing operating under Mixed-Elastohydrodynamic Lubrication. *Tribology International*, 153(2021), p.106572.
- [73] Quiñonez, A.F. and Morales-Espejel, G.E., 2016. Surface roughness effects in hydrodynamic bearings. *Tribology International*, 98(2016), pp.212-219.

- [74] Awati, V.B. and Kengangutti, A., 2019. Surface roughness effect on thermohydrodynamic analysis of journal bearings lubricated with couple stress fluids. *Nonlinear Engineering*, 8(1), pp.397-406.
- [75] Wang, J., Qu, S. and Yang, P., 2001. Simplified multigrid technique for the numerical solution to the steady-state and transient EHL line contacts and the arbitrary entrainment EHL point contacts. *Tribology International*, 34(3), pp.191-202.
- [76] Venner, C.H., ten Napel, W.T. and Bosma, R., 1990. Advanced multilevel solution of the EHL line contact problem. *Journal of Tribology*, 112(3), pp.426-431.
- [77] Su, B., Huang, L., Huang, W. and Wang, X., 2017. The load carrying capacity of textured sliding bearings with elastic deformation. *Tribology International*, 109(2017), pp.86-96.
- [78] Liu, S., Qiu, L. and Chen, X., 2021. In-Depth Exploration of the Multigrid Method to Simulate Elastohydrodynamic Line Lubrications With Smooth, Wavy, and Rough Surfaces. *Journal of Tribology*, 143(12), p.121602.
- [79] Liu, S., Qiu, L., Wang, Z. and Chen, X., 2021. Influences of Iteration Details on Flow Continuities of Numerical Solutions to Isothermal Elastohydrodynamic Lubrication With Micro-Cavitations. *Journal of Tribology*, 143(10), p.101601.
- [80] Chang, L., Conry, T.F. and Cusano, C., 1989. An efficient, robust, multi-level computational algorithm for elastohydrodynamic lubrication. *Journal of Tribology*, 111(2), pp.193-199.
- [81] Venner, C.H. and Lubrecht, A.A., 2000. Multigrid techniques: a fast and efficient method for the numerical simulation of elastohydrodynamically lubricated point contact problems. *Proceedings of the Institution of Mechanical Engineers, Part J: Journal of Engineering Tribology*, 214(1), pp.43-62.
- [82] Noutary, M.P., Venner, C.H. and Lubrecht, A.A., 2012. Grid generation in hydrodynamic and elastohydrodynamic lubrication using algebraic multigrid method. *Proceedings of the Institution of Mechanical Engineers, Part J: Journal of Engineering Tribology*, 226(5), pp.343-349.

- [83] Awati, V.B., Kengangutti, A. and Kumar, M., 2016. Multigrid method for the solution of combined effect of viscosity variation and surface roughness on the squeeze film lubrication of journal bearings. *Journal of Mechanical Engineering*, 46(1), pp.1-8.
- [84] Liu, F., Li, Z., Yang, C., Wu, H., Yin, H. and Jiang, S., 2021. Hydrodynamic Lubrication of Partially Textured Gas Parallel Slider Bearings with Orientation Ellipse Dimples. *Mathematical Problems in Engineering*, 2021, p.4441892.
- [85] Reichelt, M., Windisch, M., Offner, G. and Santner, S., 2021. A Multigrid Method for Elasto-hydrodynamic Contact Simulations of Radial Slider Bearings. *Electronic Transactions on Numerical Analysis*, 54, pp.355-369.
- [86] Elrod, H.G., 1981. A cavitation algorithm. *Journal of Lubrication Technology*, 103(3), pp.350-354.
- [87] Fesanghary, M. and Khonsari, M.M., 2011. A modification of the switch function in the Elrod cavitation algorithm. *Journal of Tribology*, 133(2), p.024501.

# List of publications

---

## International journals

- [1] Syed, N.R. and Kakoty, S.K., 2022. Computational efficiency improvement of dimple textured hydrodynamic journal bearing using progressive mesh densification method. Transactions of the ASME: Journal of Tribology, 144(3). DOI: <https://doi.org/10.1115/1.4051039>
- [2] Syed, N.R. and Kakoty, S.K., 2022. Influence of spherical protruded and dimple texture on the journal bearing performance: A comparative theoretical analysis implementing JFO boundary conditions. Industrial Lubrication and Tribology, 74(7), pp.788-795. DOI: <https://doi.org/10.1108/ILT-04-2022-0115>
- [3] Syed, N. R., and Kakoty, S. K., A comparative study on computational efficiencies of PMD, MG and FMD methods while solving problems pertaining to dimple textured journal bearing. Journal of The Institution of Engineers (India): Series C (under review)

## International conferences

- [1] Syed, N.R. and Kakoty, S.K., 2021, December. Influence of Texture Portion and Dimple Area Density on the Tribological Characteristics of Dimple Textured Hydrodynamic Journal Bearing. In Gas Turbine India Conference (Vol. 85536, p. V001T06A001). American Society of Mechanical Engineers. DOI: <https://doi.org/10.1115/GTINDIA2021-75989>
- [2] Syed, N.R. and Kakoty, S.K., 2022, June. Analysis of the effect of spherical texture on the performance characteristics of journal bearing using JFO boundary conditions. International Conference on Recent Advances in Metallurgy and Mechanical Engineering, Arya College of Engineering, Jaipur. 17th June to 18th June, 2022, Paper ID-5869.

# Curriculum vitae

---

Born and brought up in Kadapa, a town in Andhra Pradesh, Mr. Syed Nayab Rasool is the eldest of two children of Mr. Syed Rahamathulla and Mrs. Syed Rahamathun. After schooling in Kadapa, he graduated in Mechanical Engineering from Kandula Sreenivasa Reddy Memorial College of Engineering (then affiliated with Sri Venkateswara University), Kadapa, in 2013. He took his Master of Technology degree in Machine Design from the Indian Institute of Technology Guwahati. He worked for more than a year in Tata Advanced Systems Limited, Hyderabad, as an Executive in Tooling Department. Later, he joined the Department of Mechanical Engineering of the Indian Institute of Technology Guwahati as a Research Scholar in 2017 and worked under the supervision of Prof. Sashindra Kr. Kakoty. His research interests are hydrodynamic lubrication, textured journal bearing, surface texturing and tribology.

